

**AUSTENITE DECOMPOSITION DURING HOT STRIP ROLLING OF
MICROALLOYED LOW CARBON STEEL**

by

Wing Shan Tam

B.Sc., University of Alberta, 2018

A THESIS SUBMITTED IN PARTIAL FULFILLMENT OF
THE REQUIREMENTS FOR THE DEGREE OF

MASTER OF APPLIED SCIENCE

in

THE FACULTY OF GRADUATE AND POSTDOCTORAL STUDIES
(MATERIALS ENGINEERING)

THE UNIVERSITY OF BRITISH COLUMBIA
(Vancouver)

December 2021

© Wing Shan Tam, 2021

The following individuals certify that they have read, and recommend to the Faculty of Graduate and Postdoctoral Studies for acceptance, a thesis entitled:

Austenite decomposition during hot strip rolling of microalloyed low carbon steel

submitted by Wing Shan Tam in partial fulfillment of the requirements for

the degree of Master of Applied Science

In Materials Engineering

Examining Committee:

Prof. Matthias Militzer, Materials Engineering, UBC

Supervisor

Prof. Chad W. Sinclair, Materials Engineering, UBC

Supervisory Committee Member

Prof. Rizhi Wang, Materials Engineering, UBC

Supervisory Committee Member

Abstract

Hot strip rolling is one of the most critical steel manufacturing processes, and hot rolled products are utilized in a wide range of industrial sectors such as construction, automotive, and pipelines. In the final stage of hot rolling, the steels are cooled by water on the runout table; during cooling, the austenite decomposition takes place that determines the final microstructure and thus the final properties of the hot rolled products. To achieve the desired hot band microstructures and required mechanical properties during hot strip rolling, precise control of the cooling path through the runout table is critical. In this study, the austenite decomposition kinetics during continuous cooling of two microalloyed low-carbon steels have been investigated.

Austenite grain growth, deformation and austenite decomposition tests were performed using a Gleeble 3500 thermomechanical simulator. The influence of processing parameters including austenite grain size ($10\mu\text{m}$ to $60\mu\text{m}$), cooling rate (3°C/s to 100°C/s), and retained strain (0.2, 0.4) on transformation kinetics and the transformation products under no-recrystallized rolling conditions were examined. With contact dilation measurements on a series of continuous cooling tests, transformation temperature was found to increase with decreasing prior austenite grain size, slower cooling rates and higher retained strain. Microstructure characterization was carried out using optical microscopy and EBSD. At higher transformation temperatures, ferrite-pearlite microstructures were observed. As transformation temperatures decrease, refinement of ferrite grains was seen. For sufficiently low transformation temperatures, bainitic structures were obtained. Hardness measurements obtained showed an inverse relationship with transformation temperature. A microstructure model describing these metallurgical phenomena considering the effect of prior austenite grain size, cooling rate and

retained strain has been proposed that is applicable to industrially relevant runout table cooling strategies.

Lay Summary

With continuous global economic growth, it is foreseen that the demand for steel will increase further. Improved steel processing strategies have to be developed to meet societal demands. Hot strip mills are one of the most cost-effective solutions in producing flat rolled steels with applications seen across different sectors such as automotive, energy and construction. One of the final steps in hot strip mills is water cooling on the runout table where phase transformation takes place. The micro-scale features of the transformation products determine the properties. Therefore, precise design of the cooling path is essential to ensure the quality of the steel products. In this study, the impact of various processing parameters on the austenite decomposition kinetics in two low-carbon steels were investigated. A phase transformation model has also been developed that is applicable to industrial runout table cooling conditions.

Preface

All experimental designs, sample preparations, heat treatments, *in-situ* observations, data processing, experimental analysis and modelling work in this thesis were performed by the author in the laboratories at UBC. Test samples used were fabricated by the machine shop in the Department of Materials Engineering. Analysis of laser ultrasonics results and dilatometry measurements were done using the CTOME program suite developed by Dr. Thomas Garcin. My supervisor, Professor Matthias Militzer was involved and provided continuous guidance throughout all stages of this investigation.

Table of Contents

Abstract.....	iii
Lay Summary	v
Preface.....	vi
Table of Contents	vii
List of Tables	x
List of Figures.....	xi
List of Symbols	xv
List of Abbreviations	xviii
Acknowledgements	xx
Dedication	xxi
Chapter 1: Introduction	1
Chapter 2: Literature review.....	4
2.1 Chemistry and alloying elements of line pipe steels.....	4
2.2 Continuous cooling transformation products of austenite	6
2.2.1 Austenite decomposition to ferrite.....	6
2.2.2 Austenite decomposition to polygonal ferrite/pearlite.....	7
2.2.3 Austenite decomposition to irregular ferrite	8
2.2.4 Austenite decomposition to bainite.....	9
2.2.5 Austenite decomposition to martensite.....	15
2.3 Factors influencing austenite decomposition behavior.....	17
2.3.1 Cooling rate.....	17
2.3.2 Prior austenite grain size.....	19

2.3.3	Retained strain	20
2.4	Microstructure modelling.....	24
2.4.1	Semi-empirical model.....	24
2.4.2	Diffusion controlled model	26
2.4.3	Interface controlled model	27
2.4.4	Mixed-mode model.....	28
2.4.5	JMAK model.....	29
2.4.6	Mesoscale model.....	34
Chapter 3:	Scope and objectives.....	36
Chapter 4:	Materials and experimental methodology.....	37
4.1	Introduction.....	37
4.2	Materials	37
4.3	Austenite grain size measurement	38
4.4	Continuous cooling transformation test.....	40
4.5	Austenite double hit test.....	44
4.6	Deformation transformation test.....	49
4.7	Microstructure characterization	51
4.7.1	Sample preparation for metallography.....	51
4.7.2	Optical microscope imaging	52
4.7.3	Microstructure characterization using electron backscatter diffraction.....	53
4.7.4	Austenite grain size validation.....	54
4.8	Hardness measurement	54
4.9	Phenomenological modelling approach.....	55

Chapter 5: Results and discussions	56
5.1 Introduction.....	56
5.2 Initial grain size conditions.....	56
5.3 Double hit test.....	59
5.4 Test variability	62
5.4.1 Continuous cooling transformation test.....	62
5.4.2 Deformation transformation test	63
5.4.3 Effect of sample geometries.....	64
5.5 Austenite decomposition.....	65
5.5.1 Role of cooling rate and initial austenite grain size.....	65
5.5.2 Role of retained strain.....	68
5.5.3 Optical microstructure characterization.....	70
5.5.4 EBSD	75
5.5.5 Hardness.....	78
5.6 Modelling.....	81
5.6.1 Overview.....	81
5.6.2 Ferrite start model	82
5.6.3 Growth kinetics.....	85
Chapter 6: Conclusions and future work	89
6.1 Conclusions and summary	89
6.2 Future work.....	91
Bibliography	93

List of Tables

Table 2.1 24 KS variants grouped into four CP groups along with their misorientation values [56]. Reprinted with permission from Elsevier.....	13
Table 2.2 Bain correspondence for KS variant group.....	13
Table 2.3 Ideal values of the JMAK exponent n	30
Table 4.4 Chemical composition (in wt. %) and Ae ₃ temperature of the investigated steels	38
Table 4.5 Detailed second pass holding conditions for CCT tests	42
Table 5.6 Details of holding conditions to obtained selected austenite grain sizes.....	59
Table 5.7 Deformation temperature for each testing condition	61
Table 5.8 Summary of repeatability among 5 CCT (tubular) tests.....	63
Table 5.9 Summary of repeatability among 5 deformation transformation tests	64
Table 5.10 Ferrite fraction quantification	74
Table 5.11 EQAD measurements of ferrite at selected conditions	75
Table 5.12 Summary of misorientation analysis.....	77
Table 5.13 Summary of parameters used in the ferrite start model	83
Table 5.14 Summary of JMAK fit parameters.....	86

List of Figures

Figure 1.1 Schematic diagram of a hot strip rolling mill [10]	3
Figure 2.1 Schematic of a) irregular ferrite, b) upper bainite and c) lower bainite [54].....	12
Figure 2.2 Three types of pairing observed in Takayama et al.'s [56] study 1) bainite formed at 853K b) bainite formed at 723K c) lath martensite in one prior austenite grain. Reprinted with permission from Elsevier.	14
Figure 2.3 Example of Reichert's [54] EBSD map of a) upper bainite formed from PAGS 42 μ m cooled at 10°C/s 93ppm Nb in solution and b) lower bainite formed from PAGS 42 μ m cooled at 50°C/s, 204ppm Nb in solution.....	15
Figure 2.4 CCT diagram for X80 steel with PAGS of 26 μ m (IR: irregular ferrite, UP: upper bainite and LB: lower bainite) [54].....	18
Figure 2.5 Effect of deformation on austenite grain geometry with a reduction of p [79].....	21
Figure 2.6 The grain boundary surface area ratio with respect to rolling reduction and strain [79]	22
Figure 2.7 Transformation start model by Militzer et al. [70] on a Nb steel as a function of cooling rate and grain size with the effect of retained strain. Reprinted with permission from Springer Nature.....	25
Figure 2.8 Kamat et al.'s [87] work with comparison between experimental data and model (spherical and planar) on 0.11 wt. % C (1010) steel. Reprinted with permission from Springer Nature.....	27
Figure 2.9 Comparison of a) ferrite, b) pearlite fraction between modelled data and experimental data for work by Azghandi et al. [97] in vanadium microalloyed steel. Reprinted with permission from Elsevier.....	32

Figure 2.10 Comparison of experimental and modelled phase transformation results at different cooling rate on 0.45 wt. % C-0.49 wt. %Mn steel [104]. Reprinted with permission from Elsevier.	34
Figure 4.1 Microstructures of the as-received steels (a) 04C07Nb and (b) 2C04Nb obtained using optical microscope	38
Figure 4.2 Sample Geometry used for austenite grain size measurement (dimension in mm), with a thickness of 3mm	39
Figure 4.3 Schematic of thermal cycle used in austenite grain growth tests	40
Figure 4.4 Tubular sample geometry for continuous cooling transformation tests (dimension in mm): (a) front view, (b) side view, (c) isometric view	40
Figure 4.5 Schematic plot of thermal path for continuous cooling tests	41
Figure 4.6 Gleeble set up for continuous cooling transformation tests.	42
Figure 4.7 Sample lever rule calculation of a continuous cooling transformation test: (a) dilation curve, (b) fraction transformed	44
Figure 4.8 Sample geometry used for double hit tests.....	45
Figure 4.9 Setup within the Gleeble chamber for austenite double hit tests.....	45
Figure 4.10 Schematic of thermal cycle used in austenite double hit test	46
Figure 4.11 Schematic figure of the determination of the yield stress	48
Figure 4.12 Example of a stress-strain curve obtained during a double hit test along with the mentioned variables	48
Figure 4.13 Solid cylindrical sample geometry for deformation transformation tests (dimension in mm).....	49

Figure 4.14 Two types of holders used in deformation transformation tests (left: hollow, right: solid)	50
Figure 4.15 Setup within the Gleeble chamber for deformation transformation tests.....	50
Figure 4.16 Schematic of thermal cycle used in deformation transformation tests.....	51
Figure 5.1 Laser ultrasonic measurement of grain growth at different holding temperatures for a) 04C07Nb steel and b) 2C04Nb steel.....	58
Figure 5.2 Prior austenite reconstruction map from EBSD for the 04C07Nb steel held 8 minutes at 1200°C	58
Figure 5.3 Abnormal grain growth in 04C07Nb steel at 1100°C, results from (a) LUMet and (b) EBSD	59
Figure 5.4 Softening behavior at (a) various PAGS and (b) deformation temperature (PAGS: 10µm) on 2C04Nb steel with 5s interpass time	61
Figure 5.5 Variability of repeated continuous cooling tests at 30°C/s with PAGs of 40µm for 2C04Nb	62
Figure 5.6 Variability of repeated deformation transformation measurements at cooling rate of 30°C/s with PAGS of 10µm and retained strain of 0.2	64
Figure 5.7 Overview of test repeatability between different sample geometries	65
Figure 5.8 Effect of cooling rate on austenite decomposition kinetics in 04C07Nb	66
Figure 5.9 Effect of grain size on austenite decomposition kinetics in 2C04Nb.....	67
Figure 5.10 Effect of grain size and cooling rate on 50% transformation temperature for both steels (error bar calculation included in Section 5.4.1).....	68
Figure 5.11 Effect of retained strain on austenite decomposition kinetics in 2C04Nb	69

Figure 5.12 Effect of retained strain on 50% transformation temperature for both steels (error bar calculation included in Section 5.4.2).....	70
Figure 5.13 Summary of optical micrographs showing effect of grain size and cooling rate	72
Figure 5.14 Summary of optical micrographs showing effect of retained strain.....	73
Figure 5.15 Summary of IPF mapping for 2C04Nb at cooling rate of 80°C/s.....	77
Figure 5.16 Summary of misorientation maps for 2C04Nb at cooling rate of 80°C/s	77
Figure 5.17 Hardness measurement on 2C04Nb with grain size of 10µm at various strain.....	78
Figure 5.18 Relationship between hardness and HAGB density.....	80
Figure 5.19 Relationship between hardness and transformation start temperature in all tested conditions.....	81
Figure 5.20 Summary of the resulting ferrite start modelled data with corresponding experimental data for 04C07Nb.....	84
Figure 5.21 Summary of the resulting ferrite start modelled data with corresponding experimental data for 2C04Nb.....	84
Figure 5.22 Comparison between JMAK modelled data and experimentally measured transformation kinetics for cases with PAGS of 20µm in 2C04Nb with 0.2 retained strain.....	87
Figure 5.23 Comparison of T_{50} obtained from the JMAK modelling approach with the measurement results (offset calculation included in Section 5.4.2).....	88

List of Symbols

α_λ	Growth coefficient dependent on the equilibrium carbon concentrations
β	JMAK fitting parameter
ε	Strain
φ	Cooling rate
σ_{max}	Maximum stress in the first hit
σ_{y1}	Yield stress of the first hit
σ_{y2}	Yield stress of the second hit
b	JMAK rate parameter
B	Alloy-dependent coefficient
B_s	Bainitic start temperature
c_α	Equilibrium carbon concentration in ferrite
c_γ	Equilibrium carbon concentration in austenite
c^*	Fitted parameter representing critical carbon concentration
c^0	Average carbon bulk concentration
C_{Nb}	Concentration of niobium in solution
d_a	Dilation measurement from austenite region
d_b	Dilation measurement from product region
d_{dia}	Diagonal length of the indentation in hardness measurement
d_γ	Austenite grain size
D_c	Carbon diffusivity in austenite
D_0^C	Pre-exponential diffusivity term of carbon

D	Cube edge length
F	Load
ΔG	Driving pressure
G	Growth rate
H	HAGB density
k_1	Constant for nucleation and growth model
k_2	Constant for site saturation model
I	Nucleation rate
l	Characteristic length scale
$L_{initial}$	Initial diameter
L_{after}	Diameter after compression
M_0	Pre-exponential factor of interface mobility
M_{int}	Interface mobility
M_s	Martensite start temperature
n	JMAK exponent
N_{LR}	Intercept number of grain boundaries along rolling direction
N_{LZ}	Intercept number of grain boundaries along thickness direction
N_{LT}	Intercept number of grain boundaries along transverse direction
q	Grain boundary surface area ratio between pre-rolling and post-rolling
Q	Activation energy
Q_D^c	Activation energy of carbon diffusion in austenite
R	Gas constant

R_{red}	Ratio of rolling reduction
R_f	Radius of the growing ferrite grain
s	Ferrite plate thickness
S_{gb}^0	Surface area of austenite prior to rolling
S_{gb}	Surface area of austenite grain
S_v	Total effective interfacial surface area per unit volume
t	Time
T	Temperature
T_{nr}	Recrystallization stop temperature
T_N	Nucleation temperature
T_5	Transformation start temperature, 5% transformed
T_{50}	50% transformed temperature
T_{95}	Transformation finish temperature, 95% transformed
v	Interface velocity
x	Distance between interphase and austenite
X	Fraction transformed

List of Abbreviations

API	American Petroleum Institute
ASTM	American Society for Testing and Materials
BCC	Body centered cubic
BCT	Body centered tetragonal
CA	Cellular Automata
CCT	Continuous cooling transformation
CI	Confidence index
CP	Closed-pack
CTE	Coefficient of thermal expansion
EBSD	Electron back-scattered diffraction
EQAD	Equivalent area diameter
FCC	Face centered cubic
HAGB	High angle grain boundary
HAZ	Heat affected zone
IF1	Interstitial-free
IPD	Intergranular planar defect
IPF	Inverse pole figure
IQ	Image quality
JMAK	John-Mehl-Avrami-Kolmogorov
KS	Kurdjumov-Sachs
LAGB	Low angle grain boundary
LUMet	Laser ultrasonics for metallurgy

M/A	Martensite-Austenite
MC	Monte Carlo
MCL	Markov Cluster Algorithm
NW	Nishiyama-Wassermann
OIM	Orientation imaging microscopy
OR	Orientation relationship
PAGB	Prior austenite grain boundary
PAGS	Prior austenite grain size
PFM	Phase field model
RA	Retained austenite
SEM	Scanning electron microscope
TEM	Transmission electron microscopy
TMCP	Thermomechanical controlled processing
ULC	Ultra-low carbon
VH	Vickers hardness

Acknowledgements

I would like to express my sincere gratitude to my academic supervisor, Professor Matthias Militzer for his continuous support and guidance throughout. Thanks are extended to Professor Warren Poole for his valuable inputs during our bi-weekly meetings. I am grateful to ArcelorMittal Dofasco and the Natural Sciences and Engineering Research Council of Canada (NSERC) for the funding of this project.

I gratefully acknowledge the assistance from the staff members in the Department of Materials Engineering, especially Michelle Tierney and Rebecca Abbott for their help with administrative matters; Ross McLeod, Carl Ng and David Torok for their help with sample fabrication; and Heli Eunike for her support with EBSD.

During my time here, I had the opportunity to work with a group of devoted individuals. To my colleagues in the microstructure group: Minghui Lin, Madhumanti Mandal, Mariana Mendes, Sudipta Patra, Nicolas Romualdi, Sabyasachi Roy, Brian Tran, Kaiya Yamada, Tianbi Zhang, thank you so much for all the help and insightful advice during this journey. I appreciate the fun and positive work environment that you all have fostered.

Special thanks to my friends and my church group, who were always so supportive: in particular, Angel, Calvin, Emily, Hylann, Michelle and Savina.

Last but definitely not least, to my parents and my little sister, Kelly, who always believed in me, thank you so much for the continuous support, encouragements and understanding since the beginning.

Dedicated to my parents

Chapter 1: Introduction

Hot rolling is one of the most important industrial steel manufacturing process, where steels are processed plastically at very high temperatures. Approximately 1.8 billion tonnes of crude steel were produced in 2018 worldwide, with around 800 million tonnes of hot rolled flat steel products [1]. It was foreseen that the demand for steel in 2021 will increase 3.8% compared to 2020 [2]. The application of hot rolled steels is well established in the automotive and construction industry. The production of line pipe steels with thickness below 15mm through hot strip mills has also seen growing interest due to its high productivity. With strong global economic growth, global energy demand rose by 2.1% in 2017 and is projected to increase by 25% in 2040 according to the International Energy Agency [3]. With pipelines being one of the most efficient and cost-effective means to transport energy products, the demand for line pipe steels is also expected to grow. Such demand places hot strip producers to be in a competitive position of this lucrative line pipe steel market, as they are able to manufacture advanced line pipe steel coils with reduced alloying concepts through accelerated cooling.

A typical hot strip mill consists of reheat furnaces, roughing mill, finishing mill, runout table and coilers (Figure 1.1). During the first step of the process, steel slabs are reheated from room temperature to approximately 1200°C – 1250°C in reheat furnaces. This is to solutionize microalloying elements, homogenize chemical segregation and allow for easy deformation in further steps; the material undergoes full austenization at this stage. The slabs are then passed through the roughing mill, where the rotating rolls reduce the thickness of the steel slabs; during this process, high temperature deformation occurs and the material undergoes recovery, complete recrystallization, and grain growth between successive passes. As the slabs travel into the finishing mill, further thickness reduction occurs at relatively lower temperatures compared to

the previous steps (i.e. 850°C – 1100°C). At this instance, recrystallization may be increasingly incomplete and continuous work hardening may be observed due to lower temperatures and shorter processing times. Particularly, in Nb-microalloyed steels, pancaked austenite grains are produced during this stage of hot deformation and they provide further potential nucleation sites for ferrite grains [4]. Once rolling in the finishing mill is completed, the hot band undergoes quenching on the runout table where high pressure water jets can be used for accelerated cooling. During this step, the material undergoes austenite decomposition, and this step is critical in determining the final mechanical properties. Increasing the cooling rate lowers the transformation temperatures which promotes ferrite grain refinement as well as the formation of bainitic transformation products, both of which result in increased strength of the steel [5]. After the cooling step, the strips enter a coiler where they get coiled for shipment. The coiling temperature is another critical processing parameter as it controls precipitation of nanosized carbonitrides to provide precipitation strength in microalloyed steels. The final microstructures can be affected by factors such as cooling paths, austenite grain size, retained strain and chemical composition of the steel [6]–[9]. In order to produce the desired microstructures with enhanced mechanical properties that satisfy the requirements of the product, the metallurgical processing cooling paths need to be precisely designed. As a result, significant efforts have been made to predict the microstructure evolution during runout table operation.

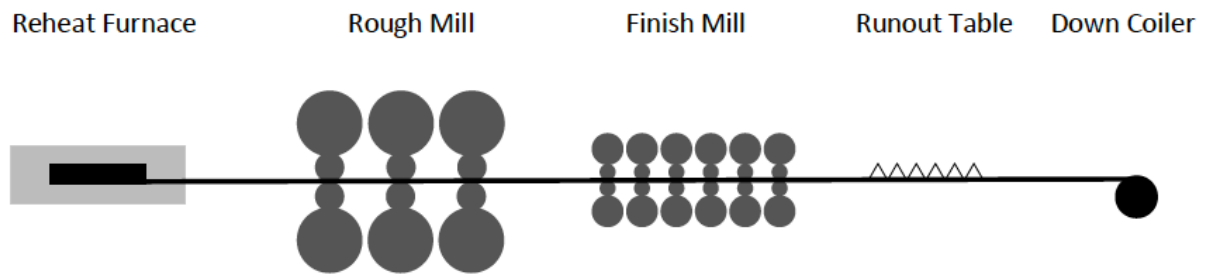


Figure 1.1 Schematic diagram of a hot strip rolling mill [10]

The current study investigates and quantifies austenite decomposition during continuous cooling in two microalloyed low carbon steels. This study is part of a wider and long-standing collaboration between the University of British Columbia (UBC) and ArcelorMittal Dofasco (AMD) with an overall goal to combine phase transformation models with heat transfer models to develop a new mechanistic runout table cooling model that is applicable for industrial use and adjustable to relevant runout table configurations. The general outcome of the overall project is to advance knowledge on accelerated runout table cooling for the production of high performance hot rolled steel strip.

Chapter 2: Literature review

2.1 Chemistry and alloying elements of line pipe steels

The manufacturing standards for fabricating seamless and welded steel pipes for conveying natural gas and petroleum are specified by API 5L in the United States and CSA Z245.1 in Canada [11], [12]. According to the API 5L standard [12], the number next to “X” in X-grade steels indicates the minimum yield strength in thousands of pound per square inch or ksi (e.g. X80 steel has a minimum yield strength of 80 ksi). Line pipe steels have low carbon content (< 0.20 wt. % C for X-grade steels) to improve weldability, with other alloying elements (mostly < 0.10 wt. %) such as Si, Nb and Ti to improve impact toughness and strength. The role of Nb is critical for thermomechanical controlled processing (TMCP) whereas Ti additions are aimed at austenite grain size control through TiN, particularly relevant for the heat affected zone (HAZ) in welds. Their mechanical properties can be further improved through microstructural controlling techniques, such as TMCP. TMCP is employed to transform steel slabs into plates or coils from which pipes are formed by combining both controlled rolling and cooling to achieve grain refinement hence the desired increase in strength.

Austenite decomposition products depend heavily on the alloying elements in steel and the thermal path that it undergoes. In this study, high performance microalloyed low-carbon steels are investigated, where Nb, Mo and Ti are of significance. The addition of alloying elements such as Nb and Mo can retard decomposition kinetics and reduce the austenite – ferrite transformation rate as they segregate to austenite grain boundaries and delay the formation of new phases.

Microalloyed Nb impedes recrystallization and grain growth during hot rolling, in the temperature range of 950°C – 1300°C. A typical range of Nb addition is within 0.03 wt. % and

0.09 wt. % for line pipe steels. Nb in solution leads to solute drag and precipitated Nb leads to particle pinning [13]. The addition of Nb promotes the production of niobium carbide and carbonitride precipitates which contribute to strength via precipitation strengthening [14], [15]. Further, Nb in solution encourages the formation of lower temperature transformation products such as finer ferrite and bainite as well as martensite. The microalloying of Nb also has a profound effect on increasing the recrystallization stop temperature, T_{nr} (i.e. in a non-recrystallization regime) [16]. Fossaert et al. [17] examined the effect of Nb precipitation on austenite transformation kinetics for low-carbon steel. It was found that a slight addition of Nb can retard both ferrite and bainite transformation considerably. The required critical cooling rate for acquiring microstructures with > 95% martensitic fraction has also been determined via dilatometric measurements, where it was learnt that by adding Nb, the required cooling rate significantly drops.

One of the well-known empirical formula to estimate T_{nr} is the Boratto equation [18], developed through multi-pass torsion as a function of chemical composition

$$T_{nr} = 464C - (644\sqrt{Nb} - 6445Nb) - (230\sqrt{V} - 732) + 363Al \quad (2.1)$$

$$+ 890Ti - 357Si + 887$$

where C, Nb, V, Al, Ti, Si are the microalloying content in wt. % in steel.

To incorporate the effect of retained strain, Bai et al. [19] developed a strain-based model as follows

$$T_{nr} = Be^{-0.36\varepsilon} \quad (2.2)$$

where B is an alloy-dependent coefficient and ε is the strain per pass. It is evident that the amount of strain can have a significant effect on T_{nr} .

Microalloying of Ti is also commonly seen for line pipe steels. Ti has strong affinity to form TiN precipitates, a stable compound that usually remains undissolved even at high temperatures. TiN precipitates play an important role in limiting austenite grain size through Zener pinning during reheating due to its stability at high temperatures [20]. While each alloying element bring its own influence, it is important to consider and understand the interaction between different alloying elements. For example, the solubility temperature of Nb rises from 1170°C in a Nb steel to 1250°C in a Nb-Ti steel [21].

2.2 Continuous cooling transformation products of austenite

2.2.1 Austenite decomposition to ferrite

Upon slow cooling to below A_{e3} , austenite begins to decompose slowly to ferrite. It is important to note that not all austenite is necessarily transformed; the remaining austenite is termed retained austenite. In a fully austenitic structure, ferrite forms primarily through nucleation at austenite grain boundaries. When small amounts of new phases are first nucleated and separated by interfaces, these new interfaces eventually advance and results in ferrite growth. Adachi et al. [22], [23] found that ferrite nuclei and austenite grains hold either a Kurdjumov-Sachs (KS) or a Nishiyama-Wassermann (NW) orientation relationship (OR) with their adjacent austenite grains. The KS and NW are two classic ORs that were discovered through X-rays diffraction in the 1930s through measurements on 1.4% carbon steel and Fe-30%Ni alloy respectively. KS OR proposes $\{111\}_\gamma/\!(011)_\alpha'$; $\langle\bar{1}01\rangle_\gamma/\!\langle\bar{1}\bar{1}1\rangle_\alpha'$, and the NW OR proposes $\{111\}_\gamma/\!(011)_\alpha'$; $\langle\bar{1}\bar{1}2\rangle_\gamma/\!\langle0\bar{1}1\rangle_\alpha'$, [24]–[26]. Homogenous nucleation is generally not favored for ferrite nucleation due to its higher energy barrier. According to Enomoto et al.'s [27] study, where a comparison of the nucleation kinetics at grain edges and grain faces in Fe-C and

Fe-C-X alloys were made assuming a spherical cap shaped nuclei, the location of nucleation was also found to be temperature sensitive. It was observed that nucleation was more likely to occur at grain corners, subsequently at grain edges, and ultimately at grain faces with increasing undercooling [23], [27]. Huang and Hillert's study [28] further confirmed that first sight of nucleation occurred at grain corners, which was followed by occurrence at grain edges and ultimately on grain faces. The growth of ferrite follows a diffusional transformation mechanism where continuous rejection of carbon from newly formed ferrite into parent austenite occurs due to the much lower solubility of carbon in ferrite than that in austenite. Long range diffusion of carbon atoms in austenite is therefore considered as the rate controlling step of such transformation [29]–[31]. It is worth noting that the growth rate can be significantly lowered by the partitioning of substitutional alloying elements across the ferrite-austenite interface [32]. Austenite decomposition products can range from polygonal ferrite with pearlite at slower cooling rates to bainitic ferrite and martensite at faster cooling rates; however, the definition of a “fast” or a “slow” cooling rate depends on the alloying content [33].

2.2.2 Austenite decomposition to polygonal ferrite/pearlite

Given an adequately slow cooling rate, the formation of polygonal ferrite is favored and accompanied by pearlite as the carbon concentration of remaining austenite increases and approaches the eutectoid composition during the formation of ferrite. Polygonal ferrite (also known as equiaxed ferrite) is characterized by smooth grain boundaries with roughly equiaxed grains which possesses a low dislocation density with no substructure. Pearlite is characterized by a lamellar or sheet arrangement of cementite and ferrite [5].

As carbon atoms continue to get rejected from daughter ferrite grains into parent austenite grains, carbon concentration increases, eventually reaching the eutectoid composition, and pearlite is formed. Pearlite nucleates initially along ferrite-austenite boundaries, and such nucleation is followed by growth of pearlite colonies into austenite [34]. The growth of pearlite is therefore controlled by carbon diffusion, growing at a relatively constant radial velocity and the lamellar structure of pearlite depends on the extent of the undercooling. As cooling continues, the driving force for austenite decomposition increases; however, at the same time carbon diffusivity decreases at lower temperature, which results in finer inter-lamellar spacing in pearlite [29].

A number of studies have reported that with an increasing volume fraction of polygonal ferrite, the yield strength of the steel is lower [35]–[37]. In a study by Wang et al. [35], the microstructure, mechanical properties and strain-hardening behavior of V-N microalloyed low-carbon pipeline steels with different TMCP parameters were studied. One of the findings was that with increasing volume fraction of polygonal ferrite, the yield strength, tensile strength and low temperature toughness decreased, and elongation increased.

2.2.3 Austenite decomposition to irregular ferrite

Another type of ferrite that can be produced from austenite decomposition, when the cooling rate is faster and transformation temperature is lower, is irregular ferrite. Irregular ferrite is characterized by its irregular and considerably finer shape that can crossover prior austenite grain boundaries. It consists of intergranular substructures and occasionally contains martensite-austenite islands (M/A) [33], [38]–[40]. These microstructures result in a combination of properties that are particularly attractive for the pipeline industry: Enhanced tensile strength,

excellent corrosion resistance, improved toughness, and superior weldability. These properties are specifically meaningful for the construction of large oil and gas pipelines used in severe environments [38], [41]–[43]. Higher hardness values were obtained for microstructures dominated by irregular ferrite when compared to polygonal ferrite, due to the higher dislocation density found among irregular ferrite [33]. Partitioning of substitutional or interstitial alloy elements may occur at the migrating interfaces which contributes to the growth of jagged boundaries [32], [40].

2.2.4 Austenite decomposition to bainite

Bainite was termed in honor of Edgar C. Bain after his discovery of the formation of a unique ferrite and carbide mixture structure at intermediate temperature (between austenite pearlite transformation and martensite formation temperature) through light microscopy [44]. Bainite was found to be a major contributor to hardness as it is the second hardest microstructure (after lath martensite) in low-carbon steel [45], [46].

The transformation start temperature of bainite is sensitive to cooling rate; however, the effect is not as significant as in ferrite formation [6]. The transformation temperature is also known to be dependent on steel chemistry. Lee developed an empirical formula (Equation (2.3)) to calculate the bainitic transformation temperature as a function of steel chemistry (in wt. %) [47] after studying previously developed empirical expressions by Steven and Haynes [24], Kunitake and Okada [48] and Kirkaldy and Venugopalan [49]. Equation (2.3) shows that increasing carbon content also reduces the bainitic transformation temperature.

$$B_s (\text{°C}) = 745 - 110C - 59Mn - 39Ni - 68Cr - 106Mo + 17MnNi \quad (2.3)$$

$$+ 6Cr^2 + 29Mo^2$$

In Lawrynowicz et al.'s [50] work, the transition temperature from upper to lower bainite was determined by dilatometry in conjunction with transmission electron microscopy (TEM) observations. It was found that the transition temperature is within a small range of 350°C to 410°C for Fe-0.38C-0.39Cr (wt. %) steel, where some influencing factors to the temperature include the thickness of bainitic ferrite lath and volume fraction of precipitated cementite [50]. Low-carbon steels consisting of Mo and Mn that have undergone continuous cooling often display microstructures composed of coarse plates with an almost granular aspect, along with tiny islands of retained austenite and martensite [46]. As early as 1967, Habarken and Economopolus [51] termed these microstructures as granular bainite and made successful detailed observations through TEM. Through their observations, it was found that these granular-like structures are in fact sheaves of bainitic ferrite with very thin regions of austenite between subunits. It was also noted that granular bainites contains minimal level of carbides. Once carbon is partitioned from the bainitic structure, it quickly distributes to stabilize neighboring retained austenite, resulting in a final structure composing of high carbon martensite and retained austenite.

For the past 80 years, the exact mechanism of bainite growth has been under debate. The two most widely proposed hypotheses are the diffusion/reconstructive driven non-cooperative growth mechanism or the shear/displacive mechanism. The diffusion controlled growth mechanism is known to describe a diffusion random walk type atom movement while the shear mechanism is defined as a glide type movement travelling across parent grain boundaries coordinately with the atoms on the other side [52].

Supporters of the diffusional model believe that bainite growth occurs through ledge-wise movement/propagation of growing interfaces along with simultaneous carbide precipitation. The process is initiated by ferrite nucleation, which is controlled by carbon diffusion through austenite. As ferrite grows, excess carbon gets rejected which results in carbide precipitation. The different growth rates of carbide and ferrite give rise to the characteristic non-lamellar structure of bainite. Supporters of the displacive model believe in a diffusionless growth process that consists of rapid autocatalytic nucleation with carbon partitioning followed by displacive growth of successive sub-units until plastic deformation is experienced in the adjoining austenites. New sub-units nucleate and grow at the tip of previously formed laths, with subsequent carbide precipitation into austenite, forming upper bainites, or into sub-units forming lower bainites with excess carbon diffused/rejected from supersaturated ferrite. With the continuous debates on austenite decomposition mechanism to bainite, the exact details remain unclear, and no single theory can fully describe the process.

Despite the controversy regarding bainite formation by steel metallurgists, it has generally been acknowledged that in low-carbon steel, bainite can be classified into two sub-categories: upper bainite and lower bainite, according to its carbide distribution depending on the fluctuation of temperature and the chemical composition of alloy [53].

Figure 2.1 a, b and c show schematics of the morphology of irregular ferrite, upper bainite and lower bainite respectively [54]. Upper bainites are obtained at relatively higher transformation temperatures where carbide precipitates reside parallel to ferritic laths. Lower bainites are created at lower transformation temperatures with carbide particles locating within sub-units of lower bainite, mostly 60-70° to longitudinal direction of ferrite plates [55].

According to Long et al.'s study [55], upper bainite shows a greater number of boundaries with lower angle misorientation, while lower bainite shows more of high angle misorientation.

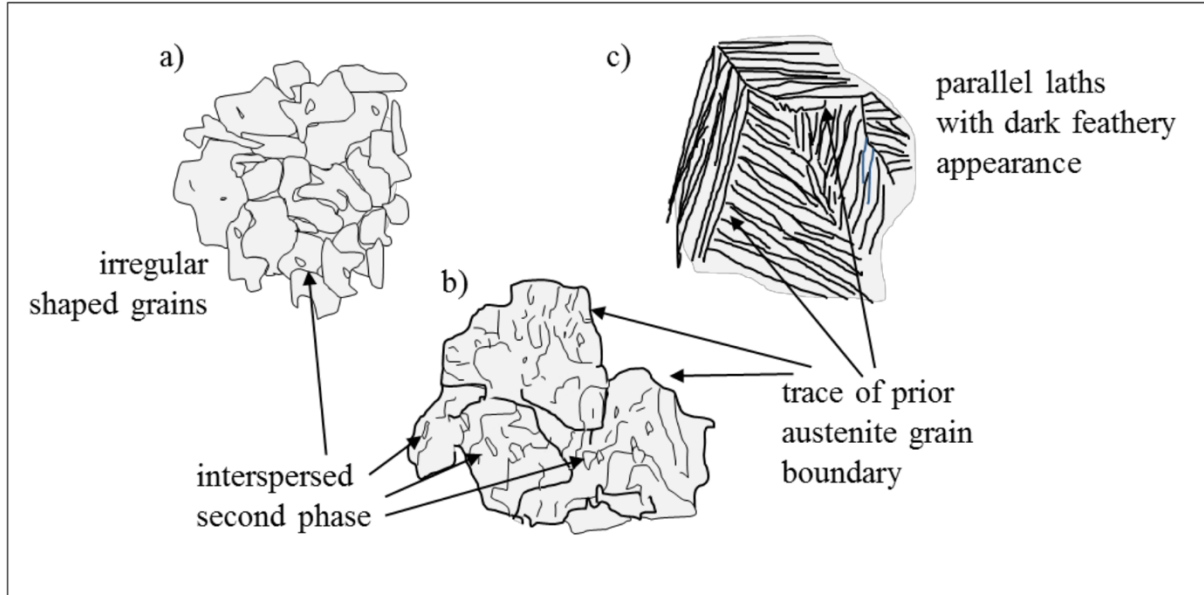


Figure 2.1 Schematic of a) irregular ferrite, b) upper bainite and c) lower bainite [54]

It can be challenging to distinguish between upper and lower bainite under an optical microscope. With the availability and help of electron back-scattered diffraction (EBSD), Bain group analysis can be conducted to discriminate between the two. Bainite was observed to nucleate with a specific orientation, near KS OR with parent austenite grains [46]. Table 2.1 details the 24 KS OR variants grouped into four closed-packed plane (CP) group based on parallel planes and three Bain groups based on parallel direction, along with their misorientation values from V1 [56].

Table 2.1 24 KS variants grouped into four CP groups along with their misorientation values [56]. Reprinted with permission from Elsevier.

Variant no.	Plane parallel	Direction parallel	CP group	Bain group	Misorientation from V1 (°)
V1	(111) _γ //(011) _α	[101] _γ //[111] _α	CP1	B1	—
V2		[101] _γ //[111] _α		B2	60.0
V3		[011] _γ //[111] _α		B3	60.0
V4		[011] _γ //[111] _α		B1	10.5
V5		[110] _γ //[111] _α		B2	60.0
V6		[110] _γ //[111] _α		B3	49.5
V7	(111) _γ //(011) _α	[101] _γ //[111] _α	CP2	B2	49.5
V8		[101] _γ //[111] _α		B1	10.5
V9		[110] _γ //[111] _α		B3	50.5
V10		[110] _γ //[111] _α		B2	50.5
V11		[011] _γ //[111] _α		B1	14.9
V12		[011] _γ //[111] _α		B3	57.2
V13	(111) _γ //(011) _α	[011] _γ //[111] _α	CP3	B1	14.9
V14		[011] _γ //[111] _α		B3	50.5
V15		[101] _γ //[111] _α		B2	57.2
V16		[101] _γ //[111] _α		B1	20.6
V17		[110] _γ //[111] _α		B3	51.7
V18		[110] _γ //[111] _α		B2	47.1
V19	(111) _γ //(011) _α	[110] _γ //[111] _α	CP4	B3	50.5
V20		[110] _γ //[111] _α		B2	57.2
V21		[011] _γ //[111] _α		B1	20.6
V22		[110] _γ //[111] _α		B3	47.1
V23		[101] _γ //[111] _α		B2	57.2
V24		[101] _γ //[111] _α		B1	21.1

Table 2.2 Bain correspondence for KS variant group

Group	Parallel Directions
B1	[001] _γ //[001] _α , [100] _γ //[110] _α , [011] _γ //[110] _α
B2	[100] _γ //[001] _α , [010] _γ //[110] _α , [001] _γ //[110] _α
B3	[010] _γ //[001] _α , [001] _γ //[110] _α , [100] _γ //[110] _α

Table 2.2 shows the three variants of Bain correspondence that were used to group KS variants into Bain groups. Takayama et al. [56] investigated quantitatively the effect of temperature on the OR between bainitic ferrite and austenite and the variant pairing in bainite and martensite in low-carbon low alloy steel with the use of EBSD. A schematic representation of the three main types (Type I, II and III) of pairing within a prior austenite grain is shown in

Figure 2.2. In the figure, the white line indicates low angle grain boundaries (LAGB) with misorientation angle less than 15° and the black line corresponds to high angle grain boundaries (HAGB) with misorientation angle more than 15° . The red, blue and yellow region each represent one Bain group. Type I was obtained where bainite was formed at a higher temperature, 853K. The same Bain group was observed in each packet, with LAGB within each packet (CP group) and HAGB between packets. This indicates that variants with LAGB tend to form adjacently. Type II was obtained when bainite was formed at a lower temperature of 723K. It was observed that variants that are in different Bain group, but same CP groups have a tendency to form adjacently. The HAGB density is also increased in Type II. Type III shows lath martensite and is a mix of both type I and II. It is similar to type II where variants of different bainite form adjacently; however, in this case, variants with lower misorientation are preferred. The HAGB density is lower than Type II but higher than Type I.

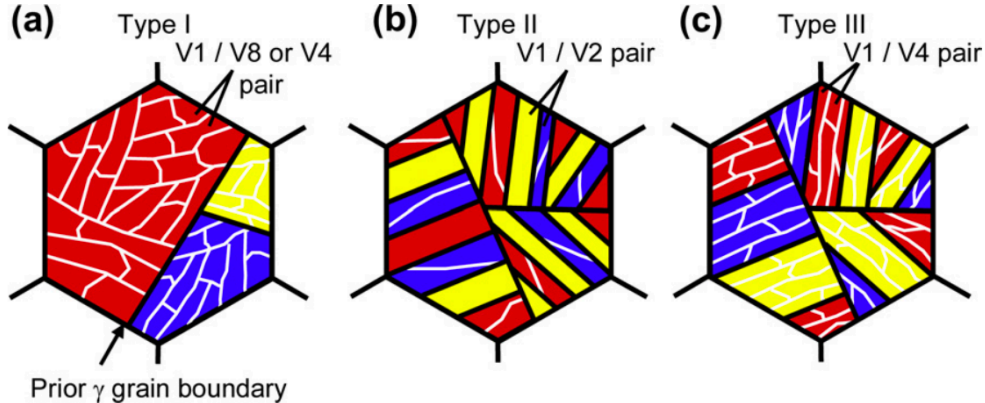


Figure 2.2 Three types of pairing observed in Takayama et al.'s [56] study 1) bainite formed at 853K b) bainite formed at 723K c) lath martensite in one prior austenite grain. Reprinted with permission from Elsevier.

Reichert et al. [54] characterized and distinguished complex transformation products: irregular ferrite, lower bainite, upper bainite, and M/A of X80 line pipe steel. Through EBSD analysis, the distinction between upper and lower bainite was made based on their crystallographic orientation. The arrangement of bainite packets is dependent on temperature; leading to higher HAGB density in lower bainite as variants of different Bain groups are arranged adjacently within one PAG. In summary, it was found that in upper bainite, only one dominant Bain group is present while in lower bainite, three Bain groups are present, separated by HAGB. Figure 2.3 a and b show an example of Reichert's [54] work of EBSD map of upper bainite and lower bainite of one prior austenite grain respectively for low-carbon steel.

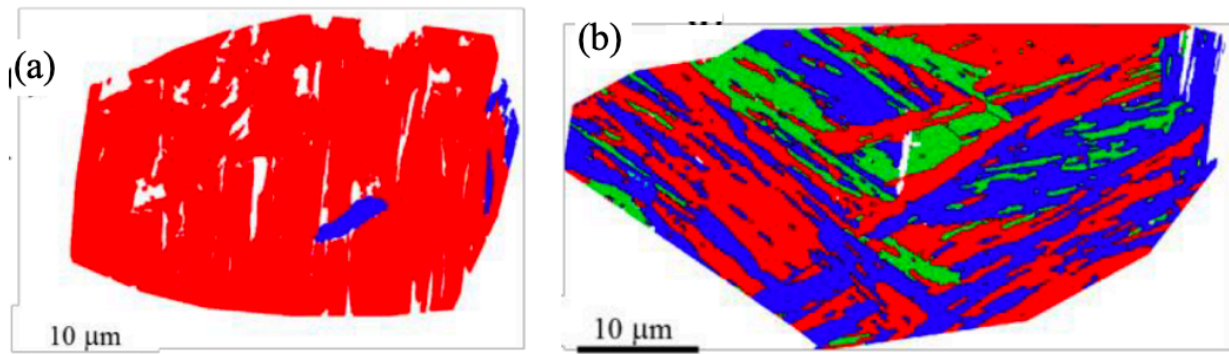


Figure 2.3 Example of Reichert's [54] EBSD map of a) upper bainite formed from PAGS 42 μm cooled at 10°C/s, 93ppm Nb in solution and b) lower bainite formed from PAGS 42 μm cooled at 50°C/s, 204ppm Nb in solution

2.2.5 Austenite decomposition to martensite

Martensite, named after the German metallurgist Adolf Martens, is a unique metastable body-centered tetragonal (BCT) structure that exists when carbon diffusion is suppressed. In Fe-C alloys and steel, martensite is formed upon high undercooling with fast cooling rate, through nucleation and growth by a displacive or military mechanism, with cooperative short range atom

movements of less than one atomic spacing [57]. For steel with low carbon content, < 0.2 wt. % , lath martensite is more commonly formed. Once the carbon content increases to > 0.2 wt. %, plate martensite becomes the more common structure. The exact detailed kinetics of martensite growth are however challenging to investigate as such transformation happens at almost the speed of sound [58]. The mismatch between BCT and cubic lattices generates elastic strain energy, which results in high kinetic barrier for martensite transformation. As a result, martensite transformation requires high driving pressure (undercooling) while continuous and rapid cooling is required to extend the transformation [59]. The temperature at which martensite transformation begins is known as the martensite start temperature, M_s , and can be described by multiple empirical formulations. Trzaska [60] has developed an empirical formula as shown in Equation (2.4) to describe the relationship between the steel chemical composition (in wt. %) and the transformation temperature.

$$M_s(\text{°C}) = 541 - 401C - 36Mn - 10.55Si - 14Cr - 18Ni - 17Mo \quad (2.4)$$

Once M_s is reached upon cooling, the amount of martensite formed depends solely on the degree of undercooling and is independent of the transformation time [44]. Due to the accumulation of carbon rejected by prior bainite and ferrite formation, austenite becomes enriched in carbon. The enrichment leads to stabilization of austenite which decreases the martensite transformation temperature. As a result, the austenite-to-martensite transformation becomes incomplete, developing final products named martensite-austenite island constituents (M/A). According to Li and Baker's study, four types of M/A particles were identified through the scanning electron microscope (SEM) including a) blocky-like or island M/A particles, b) elongated stringer particles along bainitic ferrite laths, c) connected or nearly connected M/A

particles and d) MA C structure which includes an M/A constituent with an additional phase (carbide and ferrite) [61].

It is known that the presence of M/A island reduces toughness [62] due to the brittleness of martensite [61], [63]–[67]. In Kim et al.’s [68] study, it was experimentally confirmed through Charpy tests that the amount of M/A islands is the major contributing microstructure in controlling the toughness in HAZ region; the M/A islands contribute to local embrittlement and lead to crack initiation.

2.3 Factors influencing austenite decomposition behavior

2.3.1 Cooling rate

Cooling rate plays a significant role on the kinetics of austenite decomposition, the final microstructure as well as the resulting mechanical properties. It is of significance especially for the runout table in a hot strip mill, as it is one of the most important adjustable processing parameters. With higher cooling rate, the steel undergoes a steeper temperature change in a shorter amount of time period which reduces the amount of time available for nucleation and growth of new product phase. As a result, higher cooling rate leads to lower transformation start temperature [54], [69]–[71]. For example, in Tafteh’s [6] study, it was found that with an initial austenite grain size of 80 μm and Nb precipitated, the transformation start temperature is lowered by 60°C as the cooling rate increases from 3°C/s to 100°C/s.

It is worth mentioning that as undercooling increases, the driving force increases. However, since diffusivity is temperature dependent, diffusion rate decreases as temperature decreases. In other words, the rate limiting step would initially be the driving force, followed by diffusion as temperature decreases.

With sufficiently low cooling rates, transformation takes place at the equilibrium temperature as determined by thermodynamic equilibrium. However, it is noted that the formation of polygonal or equiaxed ferrite grains is also possible with slightly faster cooling where equilibrium is not maintained at every temperature [44].

A higher cooling rate causes temperature to decrease rapidly, lowering the transformation start temperature and increases the free energy difference between austenite and forming ferrite. This leads to the activation of additional nucleation sites which produces and promotes fine ferrite structures with an associated strengthening of the final product according to the Hall-Petch relationship [5], [71]–[73]. Finer bainite ferrite structures were also observed as cooling rate increased from 3°C/s to 100°C/s in Roy's [71] study. Similar finding was also observed in Reichert's study as shown in Figure 2.4. The CCT diagram for X80 steel (0.06C-0.034Nb-0.24Mo-0.012Ti-0.0005N) shows that as cooling rate increases, transformation start temperature is lowered and transformation products go from irregular ferrite to bainite [54].

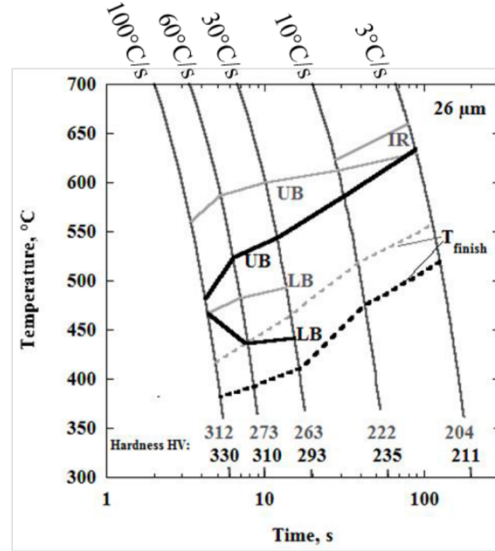


Figure 2.4 CCT diagram for X80 steel with PAGS of 26µm (IR: irregular ferrite, UP: upper bainite and LB: lower bainite) [54]

With further increase of cooling rate, the transformation start temperature continues to lower. Carbon-enriched austenite grains are stabilized until lower temperatures, which favors the formation of bainite and martensite. It is possible that remaining austenite structures are found at room temperature, and these are M/A constituents.

Given the significant role that cooling rate has on its final microstructure, precise runout table cooling path design can essentially provide an accurate control of the final mechanical properties of the steel.

2.3.2 Prior austenite grain size

The microstructures of the material prior to entering the runout table play a critical role in its subsequent transformation kinetics, hence a sound understanding of such effect will allow for better control of the final product properties. The relationship between austenite grain size and grain boundary area per unit volume is inversely proportional; this indicates that with a larger austenite grain size, the available surface area that can serve as potential nucleation sites decreases. As mentioned above, the preferred ferrite nucleation sites are grain boundary corners, edges, and faces; and it was found that the relationship between the austenite diameter, d_γ and the density of ferrite nuclei is proportional to d_γ^{-3} , d_γ^{-2} and d_γ^{-1} for nucleation at corners, edges and faces respectively [4]. The increase of nucleation site density accelerates the rate of nucleation which causes impingement of growing ferrite to happen sooner, resulting in finer ferrite grains. It also increases the ratio of nucleation rate to growth rate hence boosting the transformation rate [74]. With more nucleation sites, transformation tends to shift to higher temperature as the undercooling required is reduced, resulting in higher temperature transformation products such as polygonal ferrite. Likewise, larger prior austenite grain size

would lead to a decrease of potential nucleation sites, suppressing the formation of polygonal ferrite, which instead favors the formation of lower transformation products. These microstructures include irregular and bainitic ferrite when cooled at a lower cooling rate, and martensite or bainite if cooled at a higher cooling rate [75], [76].

2.3.3 Retained strain

In a hot strip mill, materials undergo substantial deformation during rough rolling and finish rolling. When deformation occurs below T_{nr} , the deformed austenite grains are elongated in the rolling direction and become pancaked austenites. Such pancaking along with grain refinement due to recrystallization provides a strong effect on subsequent austenite decomposition. As mentioned above, the addition of Nb increases T_{nr} due to solute dragging and Zener pinning, helping with the accumulation of strain between passes. Pancaked austenite grains are characterized by having irregular grain boundaries and deformation bands within the grain interior or localized regions with high dislocation density [4]. During deformation, smooth austenite grain boundaries become rough and irregular through a non-uniform slip mechanism within grain interior; this results in areas with high grain boundary energy, which later on become favored nucleation regions [4].

It was observed by Kazimierz and Lis [77] that when austenite grains are deformed, dislocation density increases and provides further potential nucleation sites. This allows for accelerated nucleation of bainite laths in the range of fast cooling rate. Comparing to undeformed austenite where nucleation predominately takes place along external grain boundaries, these deformed pancaked austenite grains have significantly more nucleation sites, due to the increased surface area per unit volume from the elongated grains and boundary irregularities as well as the

additional intragranular crystalline defects (i.e. annealing twin boundaries, sub-grains and deformation bands) [78]. The role of deformation and grain elongation on grain boundary surface area per unit volume was studied quantitatively by Umemoto et al. [79]. For ease of calculation, the initial austenite grain was assumed to be a sphere with a unit radius of 1 as indicated in Figure 2.5 and the grain surface without any deformation can be described as

$$S_{gb}^0 = 4\pi(r)^2 = 4\pi(1)^2 = 4\pi \quad (2.5)$$

where S_{gb}^0 is the surface area of austenite grain prior to rolling.

Once the austenite grain experiences deformation by a reduction of p , Equation (2.5) transforms into:

$$S_{gb}(p) = \int_{-1/(1-p)}^{1/(1-p)} \left[\left\{ 4x \int_0^{\pi/2} \sqrt{1 - (2p - p^2) \sin^2 \theta} d\theta \right\} \times \sqrt{\frac{x^2(1-p)^6}{1-x^2(1-p)^2} + 1} \right] dx \quad (2.6)$$

where $S_{gb}(p)$ is the surface area of austenite grain with rolling reduction of p .

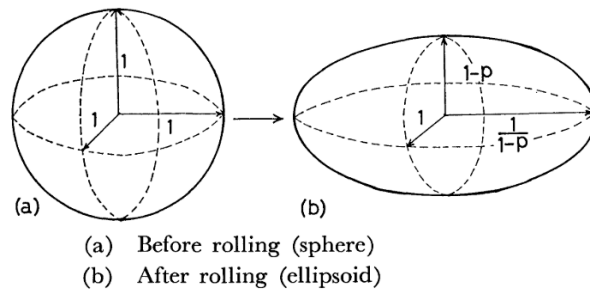


Figure 2.5 Effect of deformation on austenite grain geometry with a reduction of p [79]

The grain boundary surface area ratio between pre-rolling and post-rolling, $q = \frac{S_{gb}^0(p)}{S_{gb}^0}$

was also examined and can be described by Figure 2.6. Since volume is conserved during

deformation, the ratio of surface area, q , can be understood as the change in boundary area per unit volume. According to Figure 2.6, it is evident that when the rolling reduction is relatively low at 30% reduction (i.e. $p = 0.3$), the ratio change is also minimal ($q = 1.04$). However, following the curve, when reduction is increased to 70% (i.e. $p = 0.7$), the ratio change is noticeably significant as it is almost doubled ($q = 1.9$).

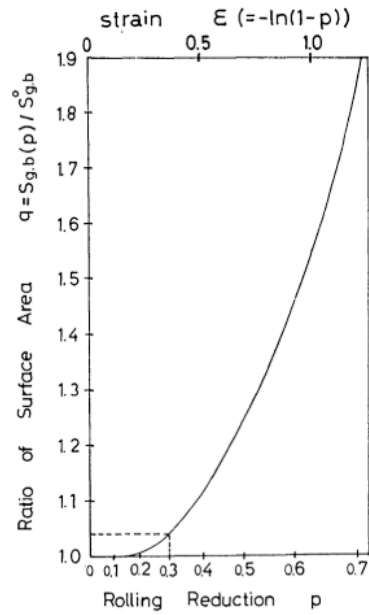


Figure 2.6 The grain boundary surface area ratio with respect to rolling reduction and strain [79]

The contributing factors to the total effective interfacial surface area per unit volume (mm^{-1}) were studied by DeArdo et al. [16] who expressed it as

$$S_v = S_v(GB) + S_v(IPD) \quad (2.7)$$

where S_v is the total effective interfacial surface area per unit volume and the determining elements include $S_v(GB)$ associated with grain boundary and $S_v(IPD)$ associated with intergranular planar defect (IPD). S_v is dependent on the pre-rolling prior austenite grain size as well as the reduction extent. An empirical relationship was made in the same study and Equation (2.7) can be represented as:

$$S_v = 0.429N_{LR} + 2.571N_{LZ} - N_{LT} + \frac{N_{DB}}{\sin(\theta)} \quad (2.8)$$

where N_{LR} , N_{LZ} and N_{LT} are the intercept number of grain boundaries per unit length along the rolling, thickness, and transverse directions respectively. N_{DB} is the length of IPD per unit area and θ refers to the angle between the plate thickness direction and the IPD.

The effect of rolling reduction on the effective surface area was further examined by Speich et al. [80] assuming cube grains with plane strain deformation

$$S_V(GB) = \frac{1}{D} \left(1 + \frac{1}{R_{red}} + R_{red} \right) \quad (2.9)$$

where $S_V(GB)$ is the effective grain boundary surface area, D is the cube edge length and R_{red} is the ratio of rolling reduction.

The effect of hot rolling condition of steels on IPD was further investigated by Ouchi et al. [81]. It was stated that $S_v(IPD)$, effective surface area from IPD depends on the rolling reduction and can be represented as follows:

$$S_V(IPD) = 63(\varepsilon - 0.3) \quad (2.10)$$

where ε is the applied deformation strain under no-recrystallization conditions.

As shown in Equation (2.10), the density of deformation bands increases linearly with associated applied deformation strain, and that the increase only takes place when the rolling reduction is greater than 30%, below T_{nr} .

Given the additional extragranular and intragranular potential nucleation sites, transformation will therefore occur at higher temperature along with increased nucleation rate and grain refinement when there is retained strain [82], [83].

2.4 Microstructure modelling

2.4.1 Semi-empirical model

Previous work has been done to describe experimental observations on austenite decomposition through different models. In 1987, Suehiro et al. [84] developed a mathematical model to examine microstructural evolution of hot strips for low carbon steels which helped to predict strength. The ferrite transformation start temperature was taken when temperature drops below T_{Ae3} which was calculated using thermodynamic parameters. The subsequent transformation was assumed to follow the “nucleation and growth” model or the “site saturation” model. In Suehiro et al.’s [84] work, the first part of the austenite ferrite transformation follows nucleation and growth and the later part follows site saturation. Following the nucleation and growth mechanism, the transformation progress can be described as

$$\frac{dX}{dt} = \frac{k_1}{d_\gamma} (IG^3)^{\frac{1}{4}} \left(\ln \frac{1}{1-X} \right)^{\frac{3}{4}} (1-X) \quad (2.11)$$

And for saturation sites, it can be described as

$$\frac{dX}{dt} = \frac{k_2}{d_\gamma} G (1-X) \quad (2.12)$$

where k_1 and k_2 are constants, d_γ is the austenite grain size before transformation, I is the nucleation rate, G is the growth rate and X is the fraction transformed.

A physical based ferrite start model developed by Militzer et al. [69] for plain carbon steels assumes carbon diffusion controlled early growth of corner nucleated ferrite. Ferrite nucleates at a particular temperature, T_N , which is independent of cooling rate. Transformation start temperature is defined as when a measurable fraction of ferrite is reached (i.e. 5% transformation).

Figure 2.7 shows an example of the modelling work of Militzer et al. [70] on a Nb steel, where the curves represent the transformation start model and the markers represent the experimental data with the effect of retained strain at $\varepsilon = 0$ and $\varepsilon = 0.5$, as a function of cooling rate, φ and PAGS, d_γ . A critical carbon enrichment value, c^* , was used in this model, above which ferrite nucleation at PAGBs is inhibited. For the Nb steel, $c^* = 1.3c^0$ was used, where c^0 is the average carbon bulk concentration. It was observed that the effect of retained strain on the transformation start temperature for this specific steel grade (Nb steel) is negligible. However, the effect of retain strain cannot be neglected for the Nb/Ti 80 steel. As retained strain increased from 0 to 0.6, c^* decreased from $2.2 c^0$ to $2.0 c^0$, which translates into an approximately 20°C increase in transformation start temperature.

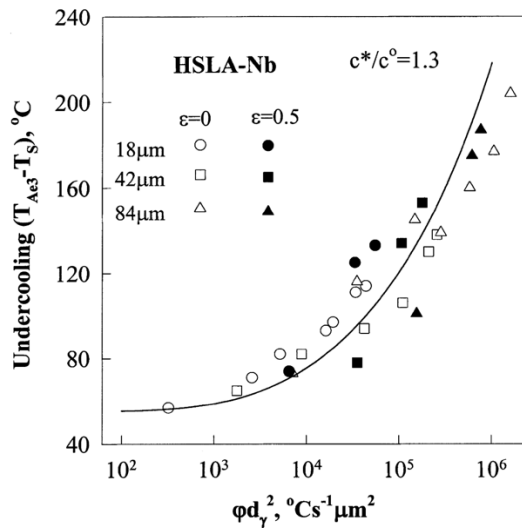


Figure 2.7 Transformation start model by Militzer et al. [70] on a Nb steel as a function of cooling rate and grain size with the effect of retained strain. Reprinted with permission from Springer Nature.

Further work was done in 2011 by Fazeli and Militzer [85] and Militzer et al. [86] where solute drag effect of Nb on the moving austenite-ferrite interface, which slows down the growth rate of ferrite particles, was considered. In this model, additional parameters were added to

consider the solute drag effect: C_{Nb} , the concentration of Nb in solution and α , an adjustable parameter that is associated to the intensity of the solute-interface interaction.

2.4.2 Diffusion controlled model

A carbon diffusion controlled model is an austenite/ferrite transformation model which assumes that the lattice transformation from face-centred cubic (FCC) to body-centred cubic (BCC) during austenite decomposition is rapid, thus the transformation rate is governed by carbon diffusion in austenite ferrite transformations. Ferrite is assumed to be supersaturated with carbon leading to an accumulation of carbon at the austenite-ferrite interface, where local equilibrium is satisfied.

Early work by Zener has used the Fick's equation to describe transformation, with the assumption that the moving interface is at all times establishing local equilibrium. Based on a linearized carbon gradient in austenite, indicating parabolic growth rate

$$s = \alpha_\lambda (D_c t)^{0.5} \quad (2.13)$$

where s is the ferrite plate thickness, D_c is the carbon diffusivity in austenite, t is time and α_λ is the growth coefficient dependent on the equilibrium carbon concentrations.

In 1992, Kamat et al. [87] developed a model describing ferrite growth process for Fe-C alloys under isothermal and stepped-isothermal conditions based on carbon diffusion and local equilibrium at austenite ferrite interface. The model assumes two simple shape approximation: planar and spherical austenite grain geometry with diameter same as initial austenite grain sizes, with no carbon flux at the centre of the austenite grain. Figure 2.8 shows a comparison of Kamat et al.'s modelling work with experimental data of isothermal transformation at 800°C on 0.11wt.% C (1010) steel. While neither of the cases exhibited complete agreement with experiment, the

spherical case displayed better prediction of ferrite growth kinetics throughout the transformation among the two, and the planar case displayed well prediction only during early stage of the transformation.

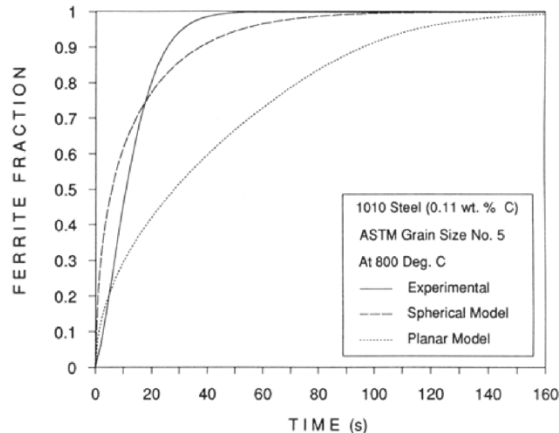


Figure 2.8 Kamat et al.'s [87] work with comparison between experimental data and model (spherical and planar) on 0.11 wt. % C (1010) steel. Reprinted with permission from Springer Nature.

Vandermeer [88] further modelled austenite decomposition in Fe-C alloys, considering a log-normal distribution of spherical austenite grains, capturing effect of temperature, carbon content, austenite grain size, and carbon buildup in the centers of parent austenite grains. It was determined that a pure carbon diffusion controlled model can only provide accurate descriptions for steel with carbon content > 0.2 wt. %. As ferrite transformation in low carbon steels depends on both long range carbon diffusion and interface migration reaction, it is important to consider for the interface reaction [89], [90].

2.4.3 Interface controlled model

For an interface controlled model, it is assumed that carbon diffusion in austenite happens infinitely fast with no carbon gradient within austenite, thus the transformation rate is governed

by interface velocity, which is determined by driving pressure and interface mobility. The interface velocity, v depends on local driving pressure for transformation, ΔG [91], [92]

$$v = M_{int} \left(1 - e^{\frac{\Delta G}{RT}} \right) \quad (2.14)$$

where ΔG is the local driving pressure and is directly related to the carbon concentration difference between interface and at equilibrium, C_{int}^γ and C_{eq}^γ respectively, R is the gas constant, T is the temperature and M_{int} is the interface mobility. M_{int} follows an Arrhenius relationship with temperature

$$M_{int} = M_0 e^{-\frac{Q}{RT}} \quad (2.15)$$

where M_0 is a pre-exponential factor that describes the interface mobility and Q is the activation energy (likely to be close to the activation energy for grain boundary diffusion, the energy barrier for atoms to enter the boundary).

When driving pressure is small, i.e. $\Delta G \ll RT$, Equation (2.14) can be re-written as

$$v = M_{int} \frac{\Delta G}{RT} \quad (2.16)$$

2.4.4 Mixed-mode model

The use of a mixed-mode model was proposed which provides a balance between carbon diffusion kinetics and lattice transformation kinetics. The mixed-mode interface migration model accounts for the intrinsic interface mobility and the carbon diffusion within austenite grains. Kop et al. [89] developed a model that considers austenite grain size, ferrite nuclei density, composition and the austenite/ferrite interface mobility to describe the phase transformation of three lean carbon-manganese steel grades (0.05 wt. % C – 0.10 wt. % C) with cooling rates

between 0.05°C/s and 60°C/s. It was shown that with decreasing cooling rate and low initial carbon level, the transformation is interface controlled; vice versa, with increasing cooling rate and high initial carbon level, transformation becomes diffusion controlled.

Krielaart et al. [90] developed a numerical method in modelling the austenite decomposition and ferrite growth in binary Fe-C alloys. Interface velocity was assumed to be proportional to local driving force which is the difference of chemical potential between the austenitic and ferritic lattice.

2.4.5 JMAK model

The Johnson-Mehl-Avrami-Kolmogorov (JMAK) Model [17] is a classical approach to describe isothermal phase transformations as well as recrystallization. It was developed separately by Johnson and Mehl and Avrami and Kolmogorov in 1937-1939 to illustrate the isothermal phase transformation mechanisms consisting of nucleation and growth. In recent years, Hillert, a Swedish metallurgist has commented to include another M into the model name "JMAK" to appreciate the efforts given by Mirkin, a Russian metallurgist who introduced the metallurgical problem in modelling isothermal formation of pearlite to the famous mathematician, Kolmogorov [93]. Equation (2.17) displays the simple expression of the JMAK formula relating fraction transformed with transformation time, where X is the fraction transformed, b is temperature dependent rate parameter, t is reaction time and the exponent n is an empirical parameter [94].

$$X = 1 - e^{-bt^n} \quad (2.17)$$

Manipulating Equation (2.17) to obtain the double logarithm form such that:

$$\ln(-\ln(1-X)) = \ln(b) + n\ln(t) \quad (2.18)$$

This suggests that a linear fit of $\ln(-\ln(1-x))$ versus $\ln(t)$ allows the determination of b and n . Some assumptions were made when deriving the JMAK model, which may not be fulfilled in practice, including random distribution of nucleation sites, constant nucleation rate or nucleation site saturation and constant linear growth rate. The value of the JMAK exponent n depends on the dimensionality and regime of the transformation. Two transformation regimes are considered: site saturation (i.e. all nuclei are present at the beginning of the transformation) and constant nucleation rate. The ideal values of n can be rigorously deducted and are shown in Table 2.3 below.

Table 2.3 Ideal values of the JMAK exponent n

Dimension	Site Saturation	Constant nucleation rate
3D	3	4
2D	2	3
1D	1	2

These values are rarely observed in experiments. It was found that discrepancy from the assumptions of the JMAK model, for example, clustering or non-random distribution of nuclei, or non-linear growth rate will cause deviations of experimentally obtained n from the ideal values [95], [96]. In practice, these two parameters, n and b , are empirically determined; b can be a function of cooling rate, PAGS, chemical composition and temperature. The JMAK model can be readily applied to non-isothermal transformations such as continuous cooling using the additivity principle, which treats a non-isothermal temperature path as many individual isothermal steps. The additivity principle is valid when the transformation reaction is isokinetic

(i.e. transformation is either nucleation- or growth-controlled, or they have the same temperature dependence). The empirical exponent n must remain constant and the transformation rate $\frac{dX}{dt}$ must be a separate function of fraction transformed $F(X)$ and temperature $G(T)$ such that

$$\frac{dX}{dt} = F(X)G(T) \quad (2.19)$$

Adapting the principle of additivity and taking a derivative of Equation (2.17) with respect of time, it becomes,

$$\frac{dX}{dt} = \frac{n(-b)^{\frac{1}{n}}}{\left(\frac{1}{1-x}\right)\left(\frac{1}{\ln(1-x)}\right)^{\frac{n-1}{n}}} \quad (2.20)$$

therefore, a non-isothermal transformation can be modelled using experimentally obtained n and b .

Application of the JMAK model on austenite decomposition is commonly seen in describing subsequent growth kinetics. Azghandi et al. [97] developed a semi-empirical model describing austenite decomposition during continuous cooling for vanadium microalloyed steel considering the effect of cooling rate and austenite grain size. 8 sub-models were included in this model, consisting of ferrite transformation start temperature, ferrite growth, pearlite start temperature, pearlite growth, bainite start temperature, bainite growth, martensite start temperature and hardness. Out of which, fractions of ferrite and pearlite were described using JMAK with Scheil's equation of additivity. $n = 1$ was used for austenite to ferrite evolution referencing to Liu et.al [98]; $n = 1.5$ was used for austenite to pearlite evolution which was determined empirically. Figure 2.9 shows the modelling results and comparison with experimental data obtained for phase fraction of ferrite and pearlite, respectively. The results

showed satisfactory agreement with experimental data in terms of phase volume fraction, with a 18%, 13% and 7% error, respectively, for pearlite, ferrite and bainite.

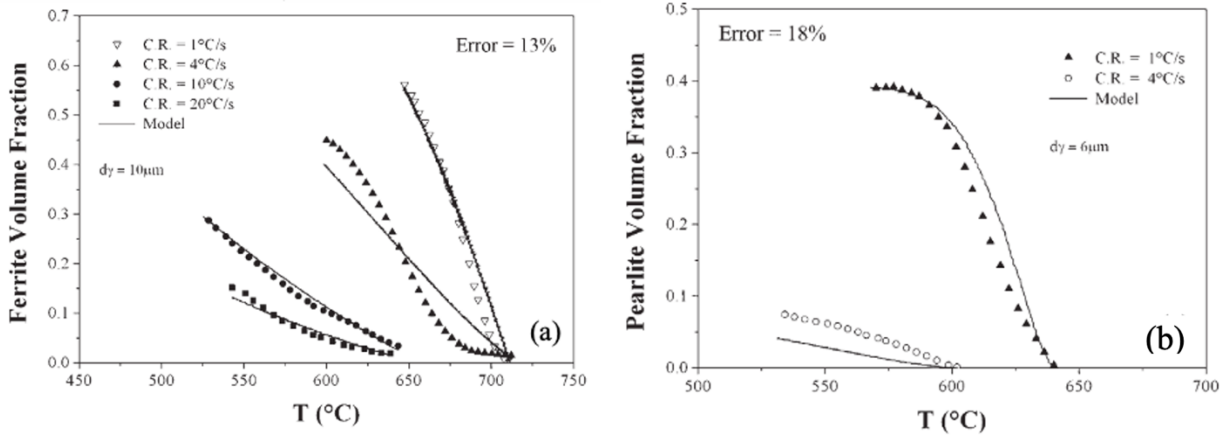


Figure 2.9 Comparison of a) ferrite, b) pearlite fraction between modelled data and experimental data for work by Azghandi et al. [97] in vanadium microalloyed steel. Reprinted with permission from Elsevier.

In 2016, Garcin et al. [99] have developed a microstructure evolution model that extends the JMAK analysis to ferrite and bainite formation on the HAZ of an X80 line pipe steel under several welding scenarios, incorporating the effect of Nb solute drag on the austenite-ferrite interface migration. The model incorporates various important microstructure phenomena such as Nb(CN) precipitates dissolution, austenite grain growth and the austenite decomposition, displaying transformation products fraction as a function of time and position (distance from fusion line) within the HAZ.

Since austenite decomposition is complicated and can yield multiple products, sub-models or extensions to JMAK have been developed assuming simultaneous [100] or sequential [101] formation of different structures to more closely simulate the phase transformation.

While the JMAK approach is commonly used for ferrite formation, it is less seen for bainite formation during continuous cooling as it does not follow in general the requirement of constant n for additivity rule to apply. Manning and Lorig [102] have examined that bainite modelling becomes more complex in most plain carbon and low alloy steels, due to the lack of consensus of the bainite transformation mechanism (i.e. displacive or diffusional) [102]. Implementation of a JMAK model and additivity principle to bainitic transformation is more challenging if assuming the transformation is controlled by diffusion. The opposing theory of displacive transformation suggests that bainite nucleates on the tips of old subunits and grows in displacive nature, hence the additivity principles can be more easily applied. In 2009, Sarkar and Militzer [103] have developed a microstructure model targeted for a Nb-Mo microalloyed steel describing both ferrite and bainite reactions with the use of a JMAK approach and the additivity principle during runout table cooling, with $n = 1.1$ for ferrite growth and $n = 0.85$ for bainite growth. The model was validated against experimental observations with corresponding hot strip rolling condition and runout table cooling strategies.

In 2016, Han et al. [104] developed a numerical model to describe the deformation, temperature, and phase transformation behavior of a Fe-C-Mn system on a run-out table in the hot strip mill. It consists of a thermodynamic model, a phase transformation model, a thermal model and a stress model. Within the phase transformation model, the JMAK approach with additivity principle was used to describe austenite decomposition into ferrite, pearlite and bainite. In this particular case, n was found to be additive, where $n = 0.8674 + 1.7506[\% C_\gamma] + 0.0583[\% Mn]$, $n = 1.5$ and $n = 1.5$ for ferrite, pearlite and bainite transformation, respectively. Figure 2.10 shows a summary of the modelled results along with experimental measurements during continuous cooling of 0.45 wt. % C-0.49 wt. % Mn steel [104].

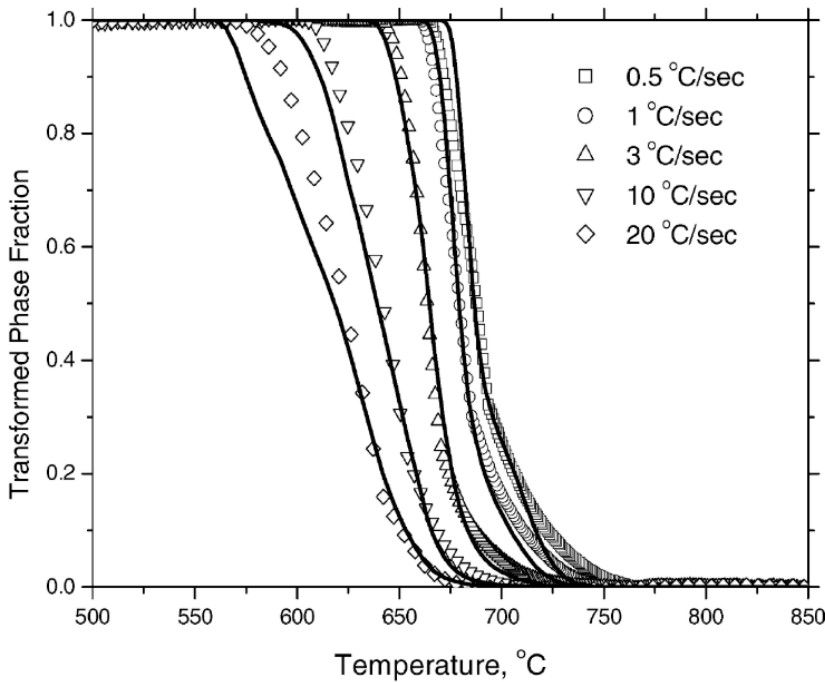


Figure 2.10 Comparison of experimental and modelled phase transformation results at different cooling rate on 0.45 wt. % C-0.49 wt. %Mn steel [104]. Reprinted with permission from Elsevier.

2.4.6 Mesoscale model

On top of the mentioned modelling approach, mean field simulations are also popular for describing microstructure evolution as they describe both microstructures and kinetics. Mesoscale models are models that describe transformation mechanisms and resulting grain structures on the length scale of microstructure. Common types of models include: phase field model (PFM), Monte Carlo (MC) Method and Cellular Automata (CA).

PFM has drawn increasing interest recently due to its ability to simulate complex microstructure features while allowing for easy incorporation of anisotropy and complex interfacial evolution [105], [106]. About two decades ago, Yeon et al. [107] first simulated austenite-ferrite transformation kinetics with 1D PFM, with a local equilibrium condition for a

substitutional Fe-Cr-Ni alloy system and a para-equilibrium for an interstitial Fe-Mn-C system. 2D PFM simulation was later developed by Pariser et al. [108] for both ultra-low carbon (ULC) and interstitial-free (IF) steel (microalloyed with small amounts of Nb and Ti), examining austenite ferrite transformation during cooling with slow cooling rates. Takahama and Sietsma [109] conducted both 2D and 3D PFMs on austenite-ferrite transformation (cooling from different austenitization temperatures between 900°C and 1200°C at 0.3°C/s), which looked into the mobility of austenite ferrite boundaries in Nb microalloyed steel with solute drag and pinning pressure terms due to NbC. It was found that the solute drag strength is highest with intermediate austenitization temperature and intermediate velocity of austenite ferrite boundary.

Chapter 3: Scope and objectives

To achieve the desired hot band microstructures and required mechanical properties during hot strip rolling, precise control of the cooling path through the runout table is critical. In this study, the austenite decomposition kinetics during continuous cooling of two microalloyed low-carbon steels with chemistries that are relevant for TMCP processing have been investigated.

The overall objective of this work is to advance knowledge on accelerated cooling for producing hot-rolled high performance steels. This overall goal can be divided into sub-objectives as follows:

1. Quantify continuous cooling phase transformation kinetics.
2. Determine the influence of processing parameters on transformation kinetics and products under no-recrystallized rolling conditions:
 - a. Prior austenite grain size
 - b. Cooling rate
 - c. Retained strain
3. Develop an austenite decomposition model that is applicable to industrially relevant runout table cooling strategies.

Chapter 4: Materials and experimental methodology

4.1 Introduction

This chapter provides the overall details of the experimental methodologies adapted in this study, which involved four major tasks: i) austenite grain size measurements, ii) continuous cooling transformation tests, iii) double hit tests and iv) deformation transformation tests. All of the mentioned tests were conducted on a GleebleTM 3500 thermomechanical simulator (Dynamic System Inc. Poestenkill, NY), with low-force jaws for thermal treatments to minimize load on the sample and high-force jaws for thermo-mechanical treatments. High vacuum was kept at $\sim 1.3 \times 10^{-5}$ Pa during the tests until helium quench started, if used; and temperature was controlled and measured using type K thermocouples with an accuracy of $\pm 1^\circ\text{C}$ spot welded mid-length. Data acquisition was done via the computer interface software QuikSim.

4.2 Materials

The investigated steels are microalloyed low-carbon steels including a laboratory steel from CanmetMATERIALS and an industrial steel provided by ArcelorMittal Dofasco (AMD). The chemical composition and Ae_3 temperatures calculated using Thermo-Calc with the TCFE7 database of both of the steels are listed in Table 4.4. The initial microstructures for both as-received steels are shown in Figure 4.1. The as-received 04C07Nb steel consists mostly of irregular ferrite with some bainite and martensite-austenite constituents (M/A) while the 2C04Nb steel consists primarily of bainite, surrounded by ferrite at prior austenite grain boundaries.

Table 4.4 Chemical composition (in wt. %) and A_{e3} temperature of the investigated steels

Label	C	Mn	Nb	Mo	Cr	Ti	N	Si	Al	A_{e3}
04C07Nb	0.039	1.67	0.070	0.11	0.031	0.014	0.0054	0.26	0.018	850°C
2C04Nb	0.19	0.95	0.040			0.020		0.25		824°C

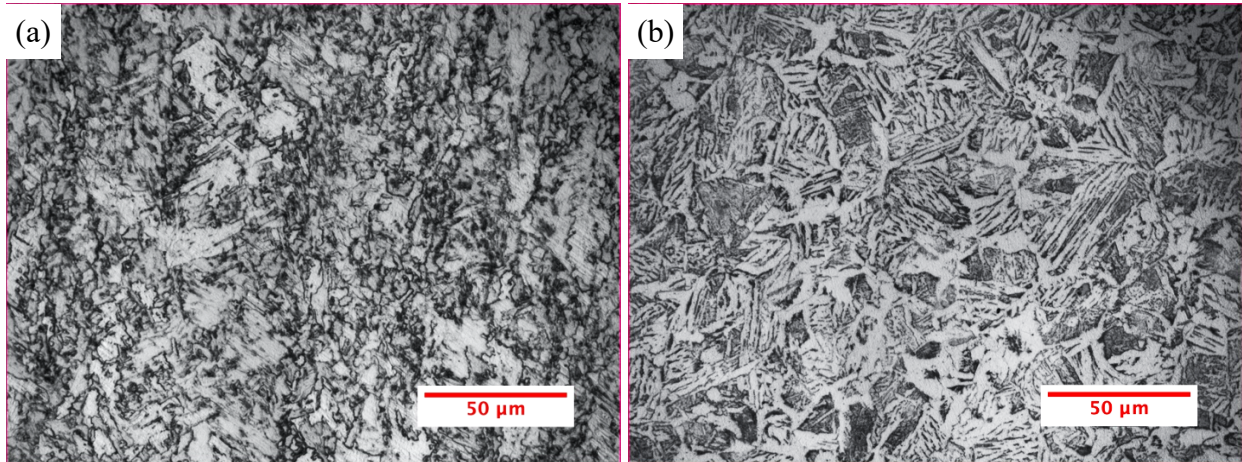


Figure 4.1 Microstructures of the as-received steels (a) 04C07Nb and (b) 2C04Nb obtained using optical microscope

4.3 Austenite grain size measurement

In order to select the appropriate reheating conditions for obtaining a representative austenite grain size ($10 - 60\mu\text{m}$) in subsequent continuous cooling tests, it is important to quantify the austenite grain size evolution for both steels.

The Laser Ultrasonics for Metallurgy system (LUMet) attached to the back of the Gleeble thermomechanical simulator conducts *in-situ* grain size measurements during heat treatments [110] [111] [112]. It consists of two lasers with a typical spot diameter of 2mm: i) a generation laser pulse that creates a pressure wave travelling across the material through ablating a thin

layer of the specimen surface and ii) a detection laser which illuminates the same part of the material and detects the subsequent echoes scattered due to discontinuities such as grain boundaries, dislocations and porosities with an interferometer. The measurement of grain size was made possible through its correlation with the attenuation between subsequent echoes of the ultrasonic waves [111]. Correlations used to obtain grain size are well established with studies on similar steels over the years [8], [113], [114]. Rectangular strip samples with the dimension of $60 \times 10 \times 3$ mm were used for this set of tests (Figure 4.2).

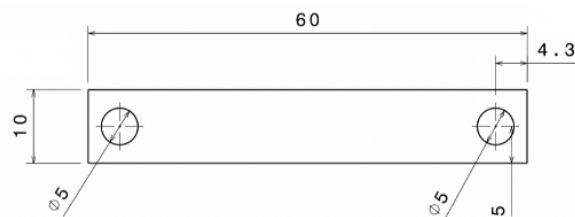


Figure 4.2 Sample Geometry used for austenite grain size measurement (dimension in mm), with a thickness of 3mm

These tests were done in two passes: in the first pass, the sample was heated up at a heating rate of $50^{\circ}\text{C}/\text{s}$ to 1300°C with a 10s holding time to solutionize all precipitates except for TiN, followed by a rapid helium quench. The cooling was fast enough to avoid any re-precipitation, cooling from 1300°C to 700°C in 3.5s. In the second pass, the sample was reheated at $50^{\circ}\text{C}/\text{s}$ to $1000^{\circ}\text{C} - 1200^{\circ}\text{C}$, and was held for 10 minutes to record the austenite grain size evolution. Figure 4.3 shows a schematic of the thermal cycle used for quantifying austenite grain growth. The LUMet austenite grain size measurements were validated *ex-situ* by EBSD PAG reconstruction in selected cases, where the detailed methodology will be described in section 4.7.3.

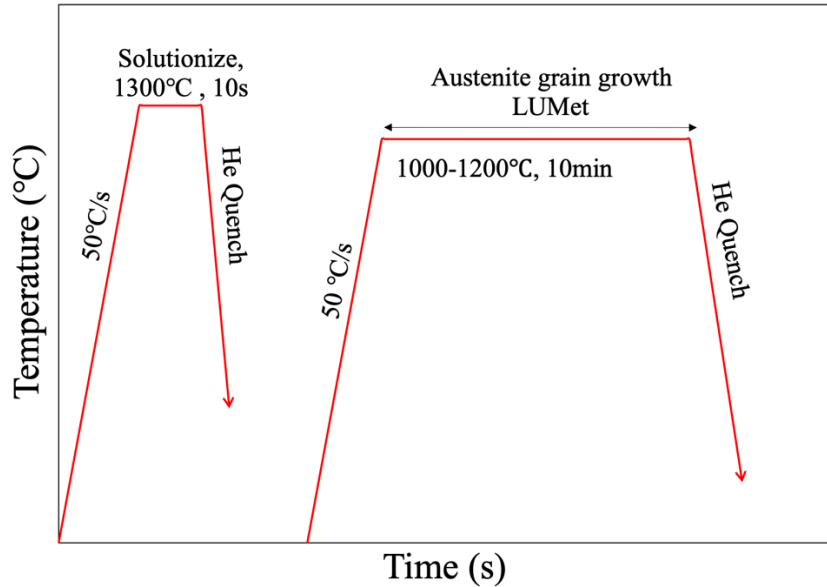


Figure 4.3 Schematic of thermal cycle used in austenite grain growth tests

4.4 Continuous cooling transformation test

Continuous cooling transformation (CCT) tests were conducted to study the influence of processing parameters including austenite grain size and cooling rate on austenite decomposition behavior. Tubular samples with 8mm outer diameter, 1mm wall thickness and 20mm length were used in the study, where sample hollowness allowed for helium gas to flow through to execute rapid axisymmetric cooling. Figure 4.4 shows the design of the specimen.

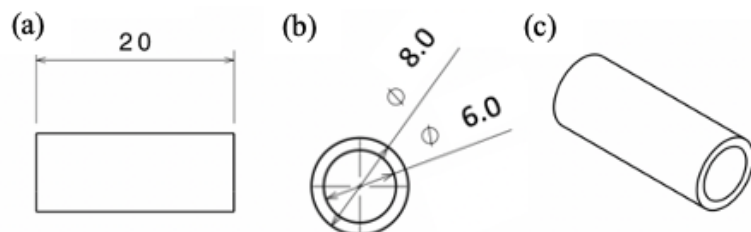


Figure 4.4 Tubular sample geometry for continuous cooling transformation tests (dimension in mm): (a) front view, (b) side view, (c) isometric view

Figure 4.5 shows the thermal path executed in the CCT tests referencing to the previously determined reheating scenarios. The samples were heated following the same first pass from the previous section, then the sample again was heated to austenization temperatures as selected previously to obtain specific austenite grain sizes followed by controlled cooling at cooling rates of 3°C/s, 10°C/s, 30°C/s and 100°C/s. Constant cooling of 3°C/s under vacuum was controlled through resistance heating, for faster cooling rates (i.e. 10°C/s, 30°C/s and 100°C/s.), helium gas was introduced to achieve the cooling rates. The details of the second pass holding conditions are shown in Table 4.5.

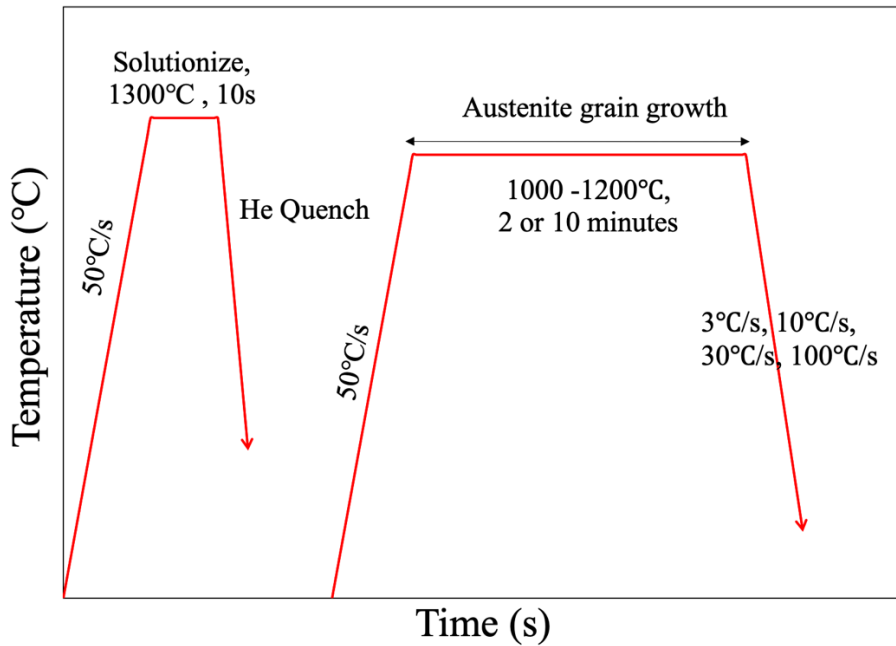


Figure 4.5 Schematic plot of thermal path for continuous cooling tests

Table 4.5 Detailed second pass holding conditions for CCT tests

Steel	Second pass holding condition
04C07Nb	1000°C, 2 min
	1200°C, 2 min
2C04Nb	1000°C, 2 min
	1050°C, 10 min
	1200°C, 2 min

During the tests, diameter change associated with austenite decomposition and thermal expansion was measured using a mechanical contact dilatometer carefully attached to the sample at the temperature measurement cross section plane. Figure 4.6 shows the setup within the Gleeble chamber for CCT tests.

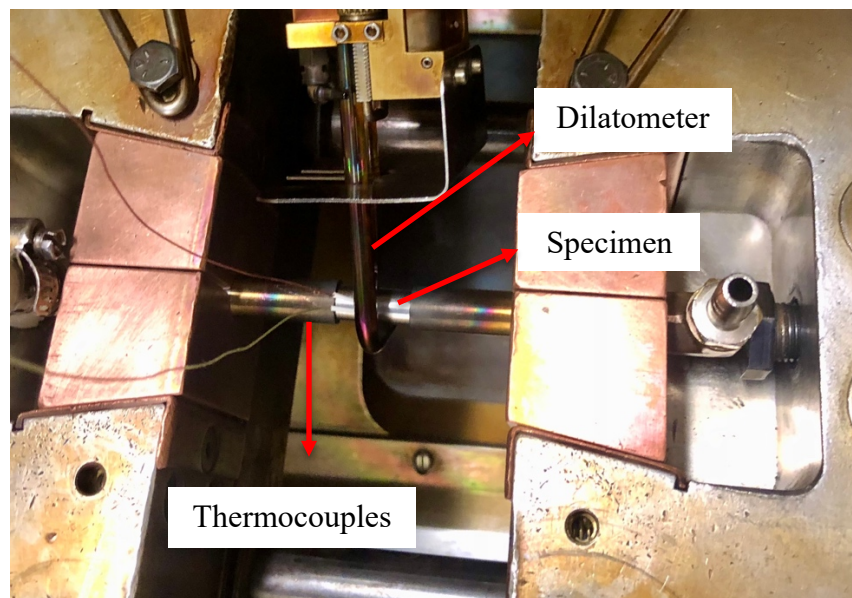


Figure 4.6 Gleeble set up for continuous cooling transformation tests.

To quantify the phase transformation, the dilation profile as a function of temperature was recorded. The system takes advantage of the specific volume difference between the different parent and resulting crystal structures of BCC and FCC, i.e. as austenite (closed-packed) decomposes into ferrite (higher density). Thus, fraction transformed during continuous cooling can be quantified through the lever rule (ASTM A1033):

$$X(T) = \frac{d(T) - d_a(T)}{d_b(T) - d_a(T)} \quad (4.1)$$

where $X(T)$ is the fraction transformed as a function of temperature, T , $d(T)$ is the measured dilation as a function of temperature, $d_a(T)$ is the extrapolated dilation from the austenite region, $d_b(T)$ is the extrapolated dilation from the product region and such extrapolation slopes are associated to their thermal expansion coefficients (CTE). An example dilation curve and the corresponding transformation curve calculation is included in Figure 4.7. Transformation start and finish temperatures are taken at 5% and 95% transformed, respectively. To ensure the reliability of the tests, experimental CTEs were compared against reported literature CTE values, i.e. $22.5 \times 10^{-6} \text{ }^{\circ}\text{C}^{-1}$ and $14.8 \times 10^{-6} \text{ }^{\circ}\text{C}^{-1}$ for austenite and ferrite, respectively [115]. Tests with CTE values within a $\pm 10\%$ margin were deemed valid.

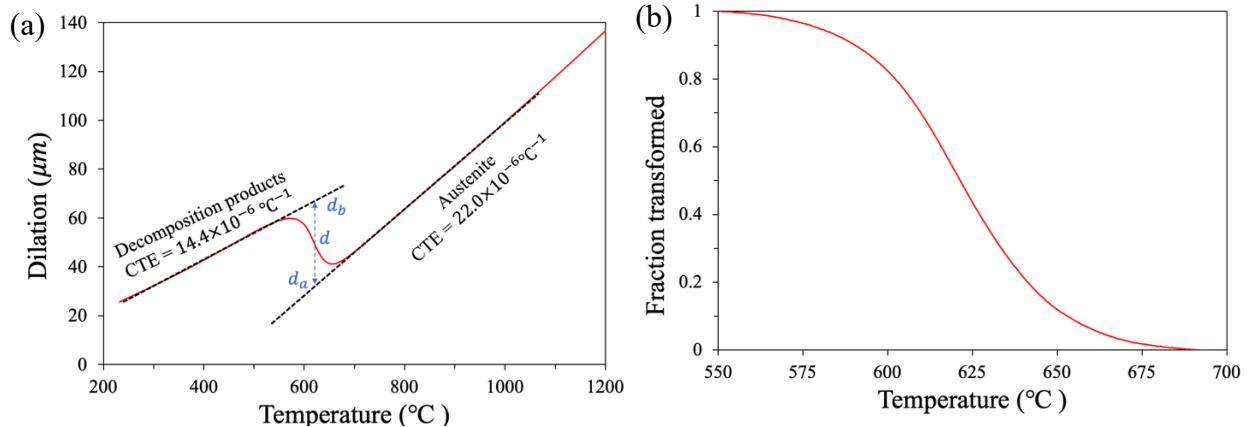


Figure 4.7 Sample lever rule calculation of a continuous cooling transformation test: (a) dilation curve, (b) fraction transformed

4.5 Austenite double hit test

To ensure the essential TMCP practice of no-recrystallization rolling and that the applied strains can be retained, double hit axisymmetric compression tests were carried out to verify that no recrystallization has taken place during the laboratory replication. Solid cylinder specimens measuring 10mm in diameter and 15mm in length were used, Figure 4.8 shows the design details of these samples. Samples were heated resistively by adjusting the current passing through the sample. A C gauge strain measuring device was also attached at the centre to track the dimension change throughout the tests for sample stress and strain rate control alongside with the load cell in line with the samples. C gauge was used here instead of the previously used dilatometer because the programmed compression caused the sample strain to exceed the measuring limit of the dilatometer and such high measuring resolution was also not necessary. Water cooling supply was connected to the C gauge to avoid any heat damage to the device during the thermal mechanical treatment.

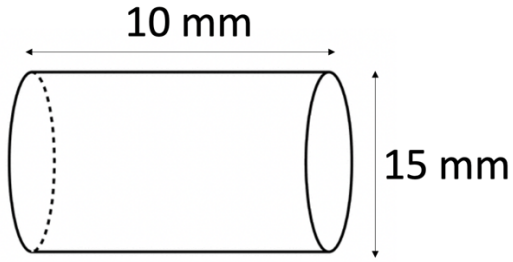


Figure 4.8 Sample geometry used for double hit tests

To prepare the cylindrical samples for tests, a 3/4" tantalum disk and a 5/8" graphite disk were placed on each side of the sample along with thin layers of nickel paste as lubricants. The sample was then placed between two hydraulically operated anvil holders and was held in place with 800N compressive force. Figure 4.9 shows the setup within the Gleeble chamber of the austenite double hit tests.

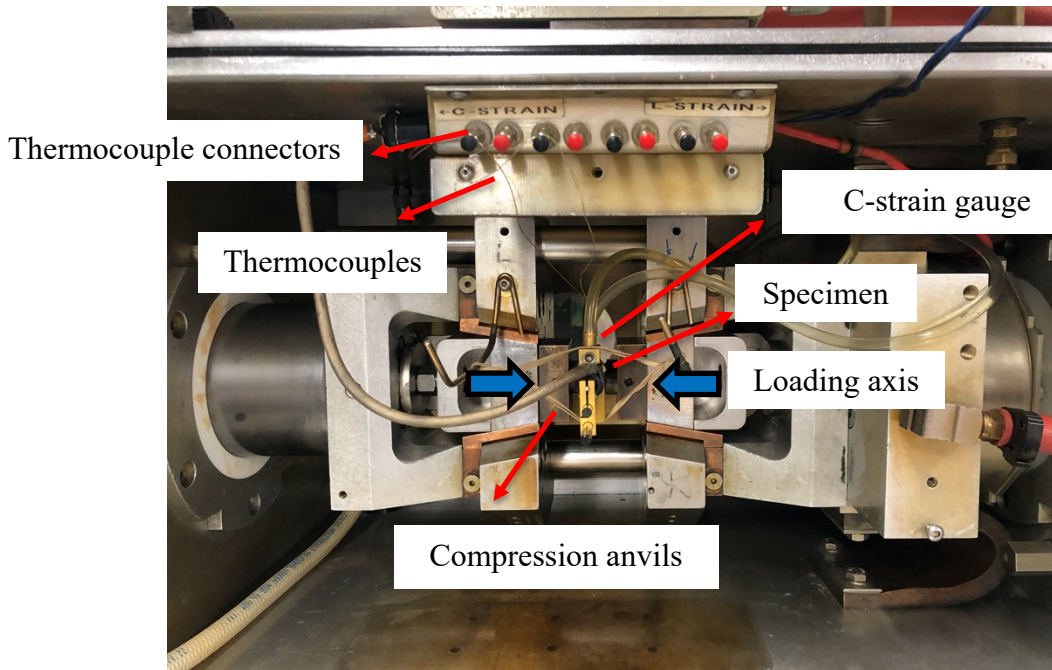


Figure 4.9 Setup within the Gleeble chamber for austenite double hit tests

ISO-T flow stress compression anvils were crucial for the double hit tests in ensuring a uniform temperature distribution along the specimen. It was important that these anvil holders

were well maintained and re-assembled every tenth tests. A two-step thermo-mechanical path was employed: the first step remains the same to serve the purpose of full precipitate dissolution, the heating rate is limited to $5^{\circ}\text{C}/\text{s}$ because the planar anvils used to compress the cylinders are designed to heat up at a uniform lengthwise temperature to ensure the sample is compressed at the desired temperature; the second step was to reheat and hold the sample at the austenitization condition selected previously, then cooled at $5^{\circ}\text{C}/\text{s}$ to 900°C where the compressions are executed once temperature has been stabilized for 5s . The compression strains for the two hits were either 0.2 and 0.1 or 0.4 and 0.1 at a strain rate of 1s^{-1} with varying interpass times of 1s and 5s. Figure 4.10 shows the thermo-mechanical paths employed.

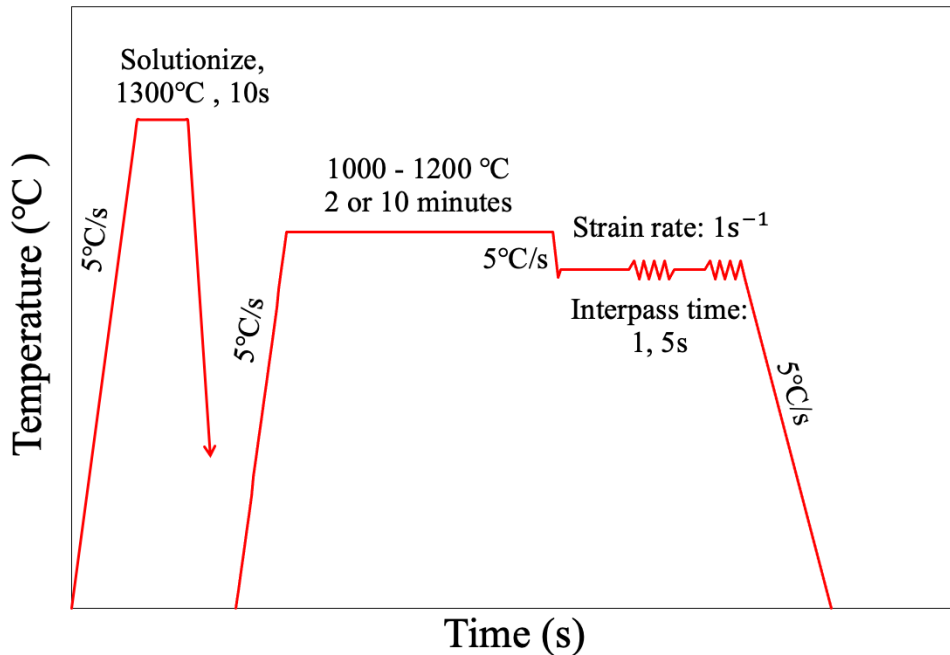


Figure 4.10 Schematic of thermal cycle used in austenite double hit test

With the acquired displacement data from the strain measuring device and load data from the load cells, true axial stress and true axial strain can be calculated using Equation (4.2) and Equation (4.3), respectively:

$$\sigma_{true} = \frac{Force}{Instantaneous\ Area} \quad (4.2)$$

$$\varepsilon_{true,dia} = -2 \times \ln \left(\frac{L_{initial}}{L_{after}} \right) \quad (4.3)$$

where σ_{true} is the true stress, $\varepsilon_{true,dia}$ is the true diametral strain, $L_{initial}$ is the initial diameter, and L_{after} is the diameter after compression.

With the stress and strain information, fraction softened can be calculated as follows:

$$F_s = \frac{\sigma_{max} - \sigma_{y2}}{\sigma_{max} - \sigma_{y1}} \quad (4.4)$$

where F_s is the fraction softened, σ_{max} is the maximum stress in the first hit before unloading occurs, σ_{y1} is the yield stress of the first hit and σ_{y2} is the yield stress of the second hit. Yield stresses were determined using an offset strain of 0.2% as shown in Figure 4.11 by drawing a parallel line with the linear portion of the stress strain profile; the yield stress is taken at the

intersection with the measured stress-strain curve. Figure 4.12 shows a typical stress-strain curve along with the mentioned variables labelled.

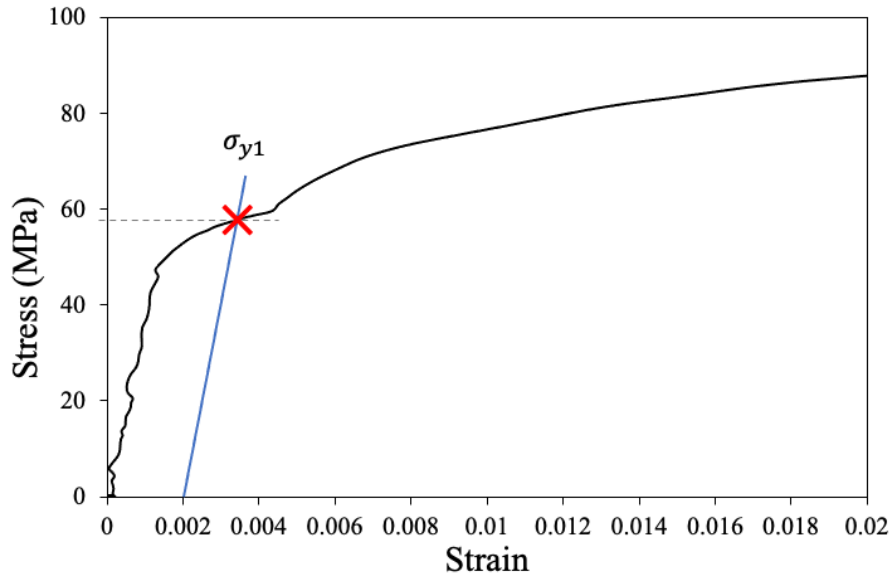


Figure 4.11 Schematic figure of the determination of the yield stress

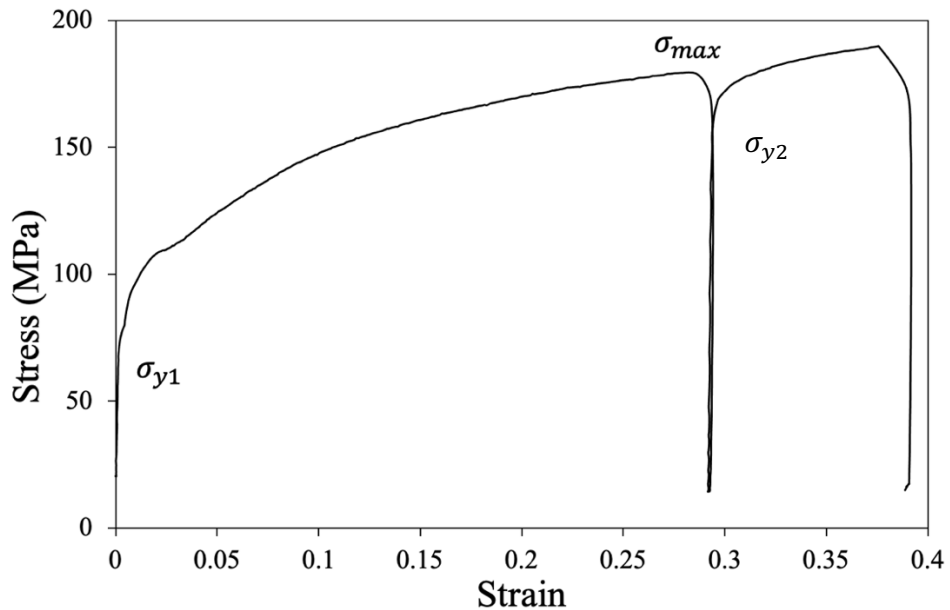


Figure 4.12 Example of a stress-strain curve obtained during a double hit test along with the mentioned variables

4.6 Deformation transformation test

Deformation transformation tests were conducted to examine the effect of retained strain on austenite decomposition behavior. Solid cylindrical rods with threaded ends measuring 120mm in total length and 10mm in diameter; with a reduced section of 10mm in length and 6mm in diameter were used, Figure 4.13 shows the design details of the samples.

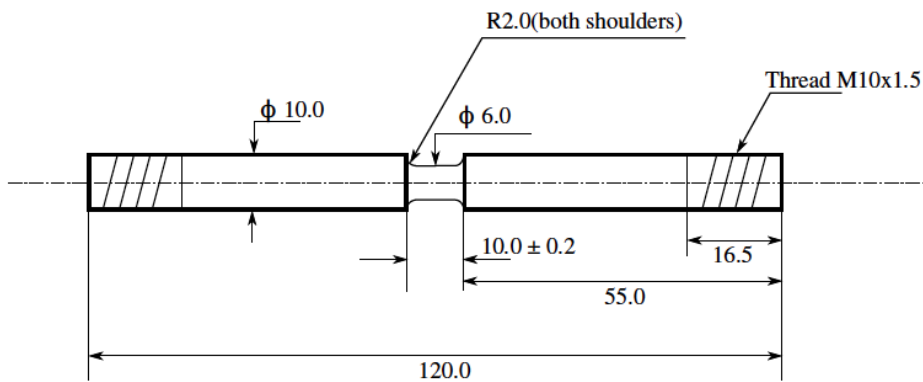


Figure 4.13 Solid cylindrical sample geometry for deformation transformation tests (dimension in mm)

To maintain the sample in place inside the Gleeble chamber, a pair of copper grips were used. Solid copper holders allow better heat transfer, and were used when conducting tests that required cooling rates of $10^{\circ}\text{C}/\text{s}$ and above, however, to minimize thermal gradients along the sample, hollow copper holders were used when high cooling rates were not necessary (i.e. tests at $3^{\circ}\text{C}/\text{s}$). Cooling was achieved through conductive heat transfer using the copper grips while Gleeble provides temperature control to conform to the desired cooling rate. Figure 4.14 shows the two types of copper holders. A pair of clamps with an adjustable nut was also fitted behind the copper holders. They were critical for restraining the sample and ensuring proper force transfer during the compression tests. Helium gas cooling was not used in these tests as it can

introduce significant temperature gradients along the cross section of these solid samples. Figure 4.15 shows the detailed setup for deformation transformation tests.



Figure 4.14 Two types of holders used in deformation transformation tests (left: hollow, right: solid)

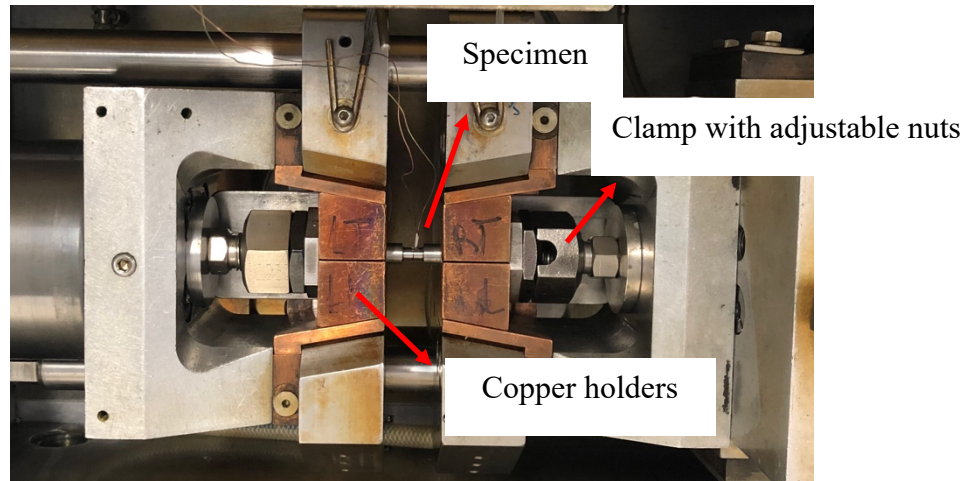


Figure 4.15 Setup within the Gleble chamber for deformation transformation tests

A two-step thermal path was employed with a contact dilatometer attached at the mid plane of the sample to measure its volume changes when undergoing the imposed thermal cycles. Deformation took place at 850°C or 900°C with a strain of 0.2 or 0.4, respectively. These two strain levels fall into the range of the true strains applied in finish rolling below T_{nr} . The strain rate was set as 1s^{-1} to allow for a controlled experiment. After the deformation, the sample was

cooled to room temperature at cooling rates of 3°C/s, 10°C/s, 30°C/s or 80°C/s. Figure 4.16 provides a schematic of the thermal cycles employed.

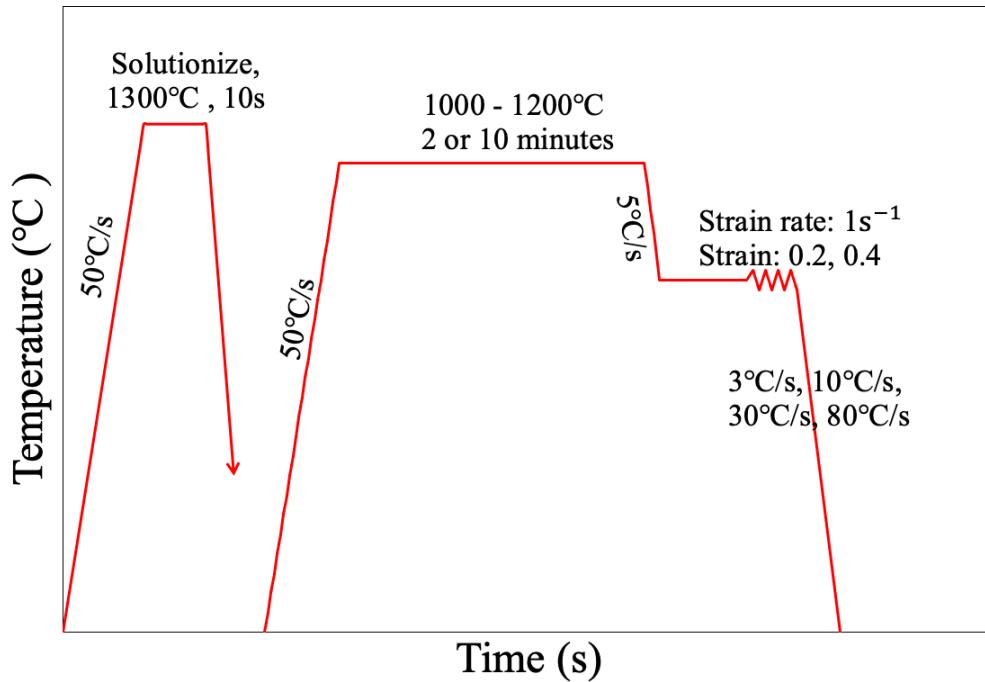


Figure 4.16 Schematic of thermal cycle used in deformation transformation tests

4.7 Microstructure characterization

4.7.1 Sample preparation for metallography

To prepare selected specimens for further metallographic studies, the samples were first cut mid-length at the thermocouple positions using a Struers Accutom-2 water cooled diamond cut off machine. A Buehler compression mounting press along with phenolic epoxy resin were used to hot mount the sectioned sample for optical microscopy. Mechanical polishing procedures were performed with a Buehler polishing machine, using 320, 600, 800 and 1200 grit SiC grinding papers with continuous water stream for lubrication, followed by diamond polishing of 6µm and 1µm accompanied with a lubricating agent. Between each polishing step, the sample

was washed briefly with distilled water then denatured ethyl alcohol and then dried with compressed air. Once the sample surface was scratch free, it was etched for 15s using a 2% Nital solution which consists of 2% by volume nitric acid in ethyl alcohol, followed immediately by a rinse with denatured ethyl alcohol and dried with compressed air.

Sample preparation for electron backscattered diffraction (EBSD) follows a similar polishing procedure, however the specimens were polished without an epoxy mount to allow it to fit inside the SEM sample stage and to remain conductive. Electropolishing was then performed at room temperature with an electrolyte of 95% acetic and 5% perchloric acid, applying a voltage of 15V for 15s, to relieve sample surface strain caused by mechanical polishing, which was followed by a liquid soap rinse and dried with compressed air. To ensure the quality of the EBSD patterns, samples were also cleaned in an ethanol ultrasound bath before scanning.

4.7.2 Optical microscope imaging

Preliminary microstructure characterization was done using a Nikon EPIPHOT 300 series inverted optical microscope attached with a digital camera, capturing optical images at magnification between 100x to 500x following standard metallographic technique. To result in clearer and sharper images, the multi-layer feature was used to automatically combine multiple captured images in case of uneven sample surface. The multi-layer grab feature helps to provide a sharper image by combining multiple images focused at various focal distances, resulting in one sharp image.

4.7.3 Microstructure characterization using electron backscatter diffraction

EBSD metallographic measurements were acquired using a Zeiss Sigma field emission gun scanning electron microscope (FEGSEM) with an EDAX DigiView EBSD Camera and TSL Orientation Imaging Microscopy (OIM) data collection software (6th edition).

Once the sample was loaded, the chamber was then pumped to vacuum with a pressure of 10^{-3} Pa. Sample was then tilted by a 70° angle to optimize the contrast in the diffraction pattern. A working distance of 10-12mm with an aperture size of 60μm and an acceleration voltage of 20kV were used. Images were captured with a step size of 100nm using a hexagonal grid. Ferrite (BCC) and austenite (FCC) were selected for automatic phase indexing of the obtained patterns using the OIM software. Further microstructure quantification analysis was done via the TSL OIM data analysis software using similar methodologies established by Reichert [54] , Roy [71] and Zhang [105]. Information including phase, orientation and data quality, i.e. image quality (IQ) and confidence index (CI) were obtained for each point of the EBSD scan grid.

To conduct a retained austenite analysis, the software was set to determine clusters that consist of two or more pixels as a grain and identifies those objects with FCC crystal structures as retained austenite. Hence, the retained austenite fraction can be determined.

A two-step cleaning process was used to filter out randomly indexed points and clusters. It was done by first applying a grain dilation algorithm using a grain tolerance angle of 2° and grain size threshold of 2 pixels and then a grain CI standardization with the same threshold values. Grain boundaries of 2° – 15° were considered as LAGB while grain boundaries > 15° were considered as HAGB. HAGB densities can be calculated by investigating the ferrite phase of the filtered data and dividing the total length of the HAGB by the total image area. The characteristic length scale of the microstructure can also be defined by taking a reciprocal of the

HAGB density. Ferrite-austenite grain boundaries are included, but these boundaries are negligible in comparison to ferrite-ferrite grain boundaries.

4.7.4 Austenite grain size validation

Prior austenite grain boundaries were also reconstructed using child phase orientation maps obtained from EBSD, using the PAG_GUI software developed by Nyyssönen et al. [116] along with running the open source MTEX toolbox in MATLAB. This algorithm helps with reconstructing the prior austenite grains via iterative OR determination and Markov Cluster Algorithm (MCL). With the exported colorized map showing the PAGB, the average equivalent circle area diameter of the PAGs was determined in accordance with ASTM E1382-97. The PAGBs were traced out using the ImageJ software and the grains were manually counted. The total area of the reconstructed PAG maps was then divided by the total number of grains to determine the average equivalent area diameter (EQAD) of the PAGs which was then compared to the results obtained with LUMet.

4.8 Hardness measurement

Hardness measurements were taken on all CCT test and deformation transformation test samples at the cross-sectional plane of the thermocouple positions using a Micromet 3 microhardness tester with a diamond pyramid indenter. Vickers hardness (VH) tests were conducted with 1kg load and 10s dwell time. A minimum clearance of two indent diagonal widths were maintained between each indentation and away from the sample surface to avoid any misinterpretation of hardness or property alternation due to work hardening or deformation from a previous indent. The diagonal lengths of the impression made by a diamond indenter were

measured with the attached optical microscope and were further converted into hardness measurement according to

$$HV = 0.1891 \times \frac{F}{d_{dia}^2} \quad (4.5)$$

where HV is the Vickers Hardness, F is the load in N and d_{dia} is the measured diagonal length of the indentation in mm. 10 measurements were taken per sample, and an average value along with its standard deviation were determined.

4.9 Phenomenological modelling approach

A phenomenological model describing the austenite decomposition behavior of the investigated steels was developed, including two sub-models: i) ferrite start temperature, ii) ferrite/bainite growth model.

This sub-model was built based on the ferrite start temperatures measured from the transformation tests, i.e. the temperature at which 5% transformation has occurred. The model was initially proposed by Militzer et al. [9] to describe ferrite start temperatures for plain carbon steels, assuming early carbon diffusion growth of corner ferrite nucleating at T_N where carbon enrichment continues until a particular critical carbon enrichment, given by c^* is reached. Once reached, further nucleation at the boundary is disabled which is considered as the starting condition of measurable transformation.

Ferrite and bainite growth were modelled using the Johnson-Mehl-Avrami-Kolmogorov (JMAK) approach with additivity principle. The additivity principle treats a non-isothermal temperature as many individual isothermal steps and was applied since the transformation was non-isothermal. The details of this model will be further described in Chapter 5.

Chapter 5: Results and discussions

5.1 Introduction

This chapter provides a review of the experimental results collected for this study to examine the effect of austenite grain size, cooling rate and retain strain on austenite decomposition as well as the modelling work on austenite decomposition. These tests involve a two-step thermal path: first heating up to 1300°C, followed by a second pass achieving preselected austenite conditions in terms of austenite grain size and retained strain, and ultimately controlled cooling. Microstructure analysis and resulting mechanical properties followed by microstructure modelling work will also be discussed in this chapter.

5.2 Initial grain size conditions

Austenite grain growth study was performed to determine the appropriate reheat conditions in order to obtain representative austenite grain size for finish rolling.

Figure 5.1 shows a summary of the laser ultrasonic grain measurement for both steels at isothermal holding. $t = 0\text{s}$ is defined as when the test is initialized and when the steel is still at room temperature. Firing of the laser starts when the sample has reached 500°C and grain size measurements are recorded after the sample has reached 900°C.

For the 04C07Nb steel with lower carbon concentration, a holding temperature of 1000°C resulted in comparatively little grain growth, reaching a limiting grain size of approximately 10 μm followed by some coarsening after $t = 300\text{s}$. At 1200°C holding temperature, rapid initial grain growth was observed before it slowed down to reach a limiting grain size of approximately 70 μm . Despite the upward slope towards the end of the evolution, it is seen that a change of 10s

in time leads to an average grain size change of $2\mu\text{m}$. Figure 5.2 shows the prior austenite reconstruction map obtained from EBSD after 8 minutes holding at 1200°C . The EQAD measured from the map is $53\mu\text{m}$ which is consistent with the LUMet grain measurements within a difference of 19%. This difference is considered acceptable given the scatter of around $10\mu\text{m}$ in the LUMet data and the lack of statistics presented in the EBSD map.

An attempt to obtain a third grain size for this steel was made through an intermediate holding temperature of 1100°C . Figure 5.3 shows the austenite grain size measurement obtained at this holding temperature from four repeated tests. However, each test resulted in an apparently different grain growth behaviour which is indicative for abnormal grain growth with a bimodal grain size distribution. Some scatters are seen below $10\mu\text{m}$, as this is below the level of accuracy in LUMet measurements. Figure 5.3b confirms the finding as a mixture of fine and coarse grains is seen across the reconstruction map. The abnormal grain growth can be due to precipitate reforming during the cooling and re-heating stages and subsequent dissolution at 1100°C .

The austenite grain growth results for the 2C04Nb steel are shown in Figure 5.1. With a holding temperature of 1000°C , likewise very little grain growth was observed. Limiting grain size of $10\mu\text{m}$ was achieved with further coarsening after $t = 330\text{s}$. At 1050°C , a fast grain growth was first observed, before it slowed down past $t = 100\text{s}$ and eventually reaching a limiting grain size of approximately $20\mu\text{m}$. At 1200°C holding, the initial grain growth was even more rapid. After holding for 600s , it then slowed down to reach a grain size of approximately $50\mu\text{m}$. With such growth, a change of 10s in time would introduce an average change in grain size of $3\mu\text{m}$. The slow grain growth stage could be related to the coarsening of TiN particles [8].

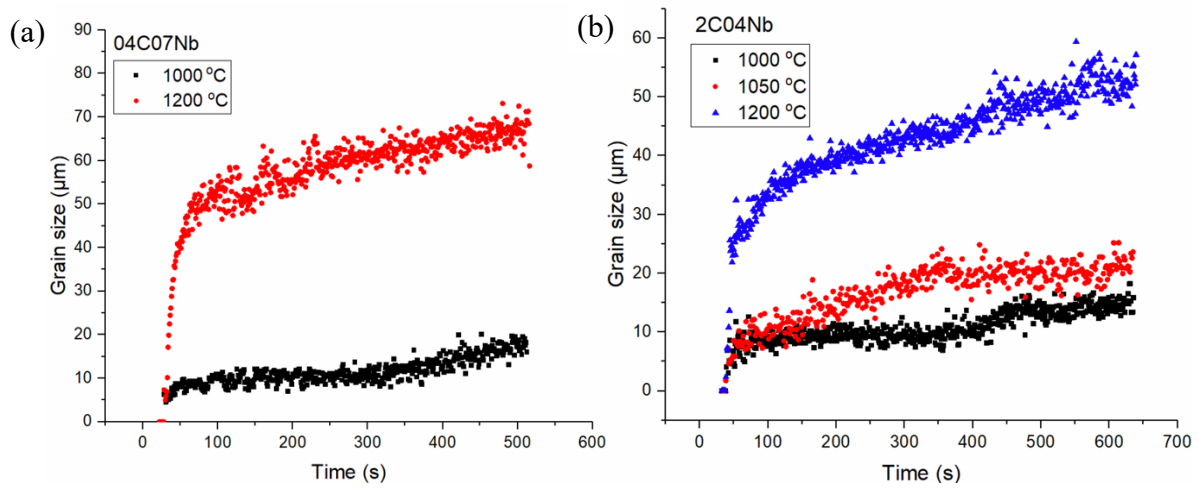


Figure 5.1 Laser ultrasonic measurement of grain growth at different holding temperatures for a) 04C07Nb steel and b) 2C04Nb steel

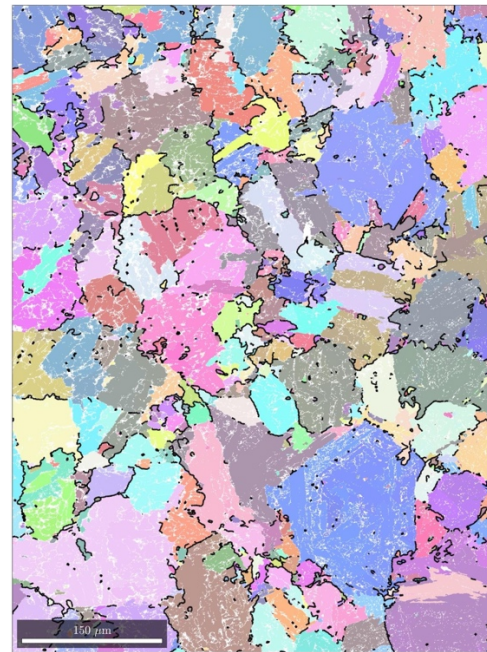


Figure 5.2 Prior austenite reconstruction map from EBSD for the 04C07Nb steel held 8 minutes at 1200°C

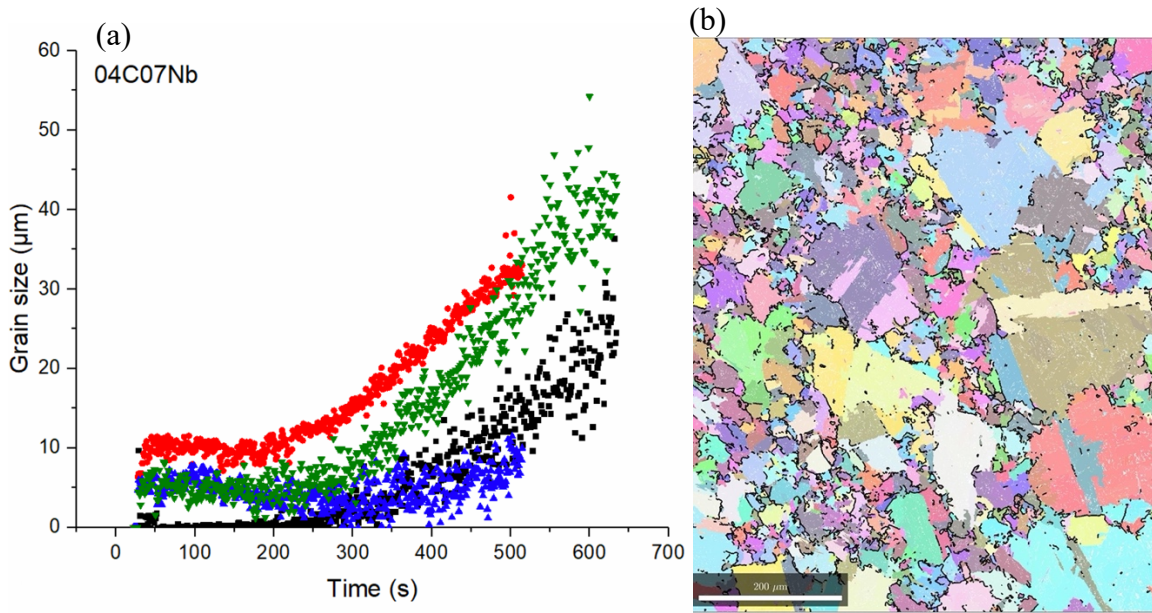


Figure 5.3 Abnormal grain growth in 04C07Nb steel at 1100°C, results from (a) LUMet and (b) EBSD

Table 5.6 shows a summary of the selected grain sizes for further studies, and the details of the second pass holding conditions.

Table 5.6 Details of holding conditions to obtain selected austenite grain sizes

Steel	Second pass holding condition	Grain Size (μm)
04C07Nb	1000°C, 2 min	10
	1200°C, 2 min	60
2C04Nb	1000°C, 2 min	10
	1050°C, 10 min	20
	1200°C, 2 min	40

5.3 Double hit test

Double hit tests were conducted to establish conditions that ensure the presence of retained strain during laboratory simulations, confirming a no-recrystallization condition to

produce pancaked austenite microstructures. Deformation temperatures were deliberately chosen slightly above the A_{e3} temperatures for both steels to maximize retained strain to ensure a no-recrystallization condition in future transformation tests.

Figure 5.4 details the effect of deformation temperature and PAGS on the softening behavior for the 2C04Nb steel. As shown in the figure, softening is much more significant in cases with smaller PAGS, there is a substantial increase of 63% in softening, going from grain size of $40\mu\text{m}$ to $10\mu\text{m}$. When lowering the deformation temperature from 900°C to 850°C , a noticeable reduction of 71% in softening was observed. It is therefore evident that deformation temperature has a significant effect on softening, where higher deformation temperature results in more softening. A significant amount of softening of 82% was recorded in one of the deformation conditions: grain size of $10\mu\text{m}$ with interpass time of 5s deforming at 900°C for 2C04Nb steel. This indicates that recrystallization has taken place between the two hits. It can be concluded that lower deformation transformation temperature, strain and larger initial grain sizes can result in less softening, which demonstrates consistency with previous findings by Petkov [7] and Sarkar et al. [7], [114].

Table 5.7 shows the deformation conditions selected for subsequent transformation tests with strain of 0.2 and 0.4. The experiments had confirmed that the softening behavior for the selected thermomechanical scenarios in both steels to be less than 20%, which can be attributed to recovery in medium and high stacking fault energy materials [70], [98]. The fraction softened for the 04C07Nb steel were 13% and 16% respectively with interpass time of 1s and 5s at deformation temperature of 900°C and PAGS of $10\mu\text{m}$. Softening is much more significant in tests with 5s interpass time compared to 1s interpass time, this is because it provides a longer time for softening, here recovery, to occur. For the 2C04Nb steel, Figure 5.4b shows that no-

recrystallization condition can be achieved, with a deformation temperature of 850°C where the fraction softened was found to be 12% with interpass time of 5s and PAGS of 10 μ m.

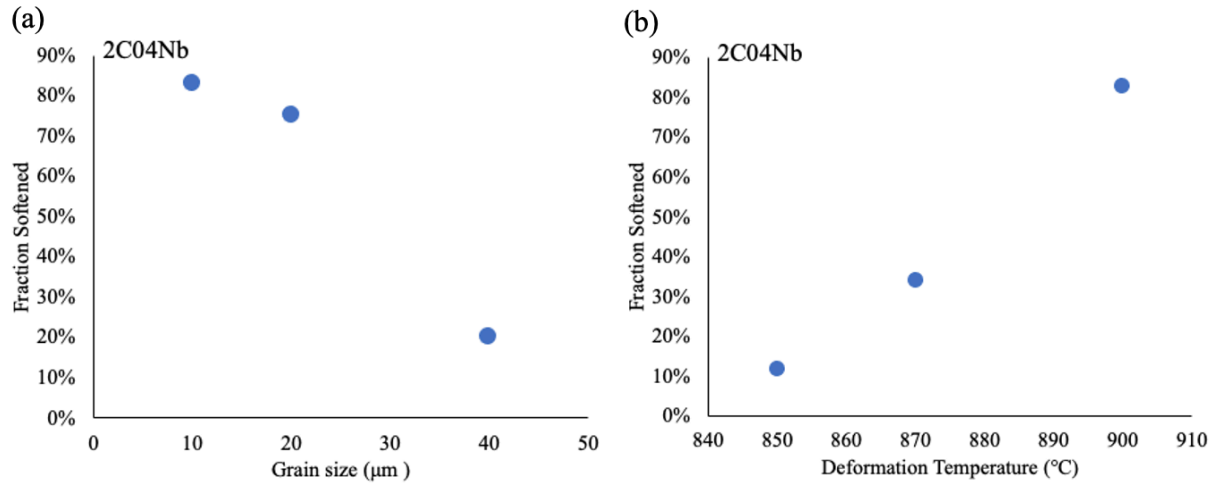


Figure 5.4 Softening behavior at (a) various PAGS and (b) deformation temperature (PAGS: 10 μ m) on 2C04Nb steel with 5s interpass time

Table 5.7 Deformation temperature for each testing condition

Steel	Grain Size (μm)	Deformation Temperature (°C)
04C07Nb	10	900
	60	900
2C04Nb	10	850
	20	850
	40	900

5.4 Test variability

5.4.1 Continuous cooling transformation test

To ensure the repeatability of the CCT tests, an experimental variability analysis was performed. Five tests were repeated under the same condition for 2C04Nb at a cooling rate of 30°C/s with PAGS of 40µm. Figure 5.5 shows a collection of the transformation curves as a function of temperature.

Table 5.8 provides the standard deviation and the maximum difference of the 5%, 50% and 95% transformation temperatures among 5 tests. A maximum standard deviation of 6°C is found during transformation start, T_5 , where this value is later used throughout to report as the accuracy of measurement for continuous cooling tests. Similar experimental variability for continuous cooling tests was found in Roy's study [71].

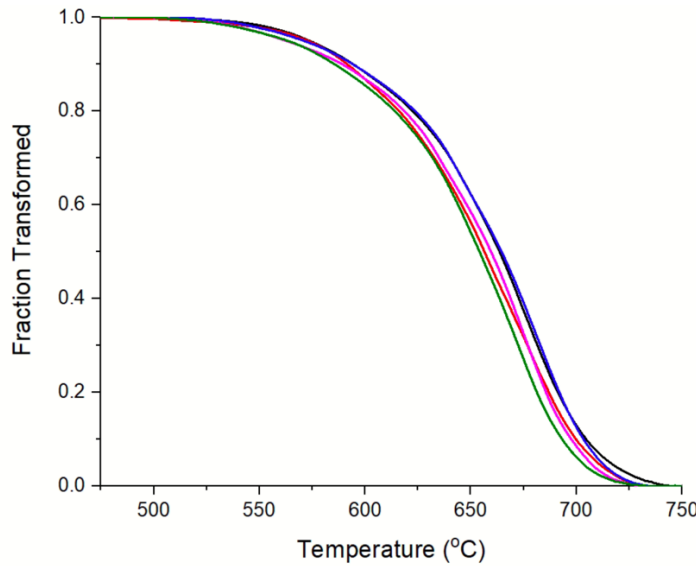


Figure 5.5 Variability of repeated continuous cooling tests at 30°C/s with PAGs of 40µm for 2C04Nb

Table 5.8 Summary of repeatability among 5 CCT (tubular) tests

	Standard Deviation (°C)	Maximum – Minimum (°C)
Transformation start, T_5	6	17
50% transformed, T_{50}	5	11
Transformation finish, T_{95}	5	11

5.4.2 Deformation transformation test

A repeatability analysis was also performed for deformation transformation tests, where 5 tests were repeated with the same condition for 2C04Nb at a cooling rate of 30°C/s with a PAGS of 10µm and a retained strain of 0.2. Figure 5.6 shows the transformation curves of the repeated tests as a function of temperature.

Table 5.9 details the standard deviation and the maximum difference of the 5%, 50% and 95% transformation temperature among 5 deformation transformation tests. As seen in the table, the maximum standard deviation is determined to be 9°C; the value is obtained when measuring 50% transformed temperature and 95% transformed temperature, hence 9°C will be used throughout as accuracy of the deformation transformation tests. A larger standard deviation is obtained in these tests as compared to the continuous cooling tests, and this can be attributed to the increased thermal gradient that the sample experienced along the length.

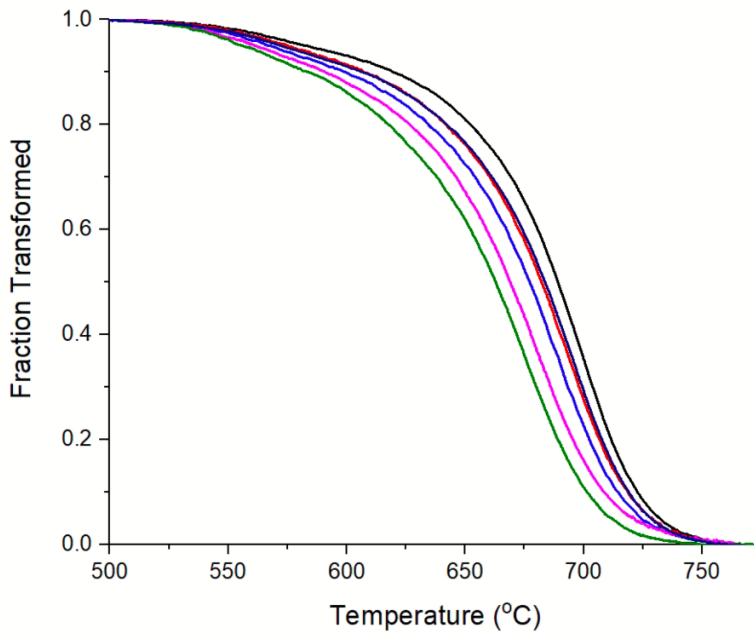


Figure 5.6 Variability of repeated deformation transformation measurements at cooling rate of 30°C/s with PAGS of 10µm and retained strain of 0.2

Table 5.9 Summary of repeatability among 5 deformation transformation tests

	Standard Deviation (°C)	Maximum – Minimum (°C)
Transformation start, T_5	7	17
50% transformed, T_{50}	9	22
Transformation finish, T_{95}	9	22

5.4.3 Effect of sample geometries

Since different sample geometries were used between the CCT tests and the deformation tests (i.e. tubular samples were used for CCT and solid rods were used for deformation tests), the potential effect of sample geometry on transformation measurements was examined to determine the variabilities.

Figure 5.7 shows three sets of repeated tests with different sample geometries for 2C04Nb. It is seen that the differences in transformation between the two different geometries are within a variation of 5°C, except for T_{50} for 10°C/s with a difference of 13°C and T_{95} for 30°C/s with a difference of 17°C. A 13°C difference of T_{50} is within the overlap of the error bars from the two geometries. Even though there is a 17°C difference for one of the T_{95} , the transformation curves are overall in agreement within the accuracy of data measurement of 5°C up to 90% transformation.

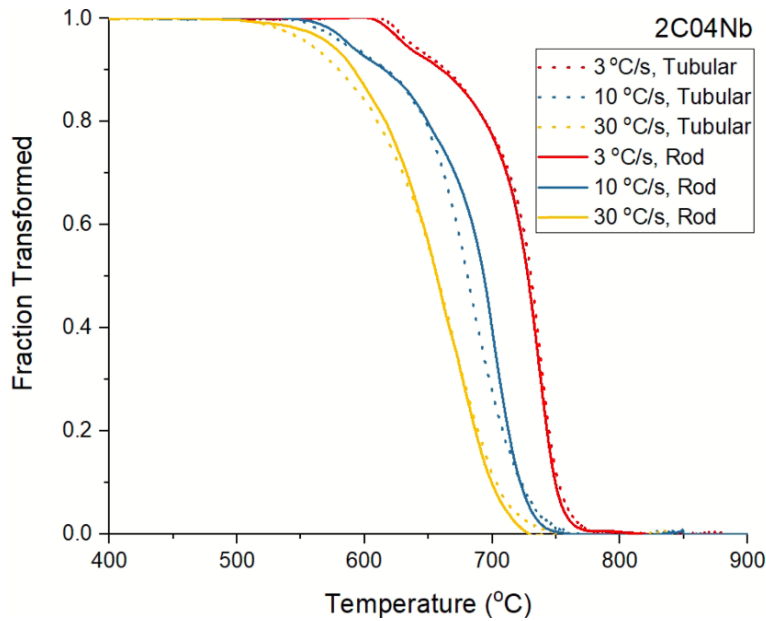


Figure 5.7 Overview of test repeatability between different sample geometries

5.5 Austenite decomposition

5.5.1 Role of cooling rate and initial austenite grain size

To examine the influence of cooling rate on austenite decomposition transformation, 4 different cooling rates of 3°C/s, 10°C/s, 30°C/s, 100°C/s were used. Figure 5.8 shows the continuous cooling transformation kinetics of the 04C07Nb steel with 10µm austenite grain size

at different cooling rates. It shows that as cooling rates increases, transformation curves shift to the left, indicating a decrease in transformation temperature. When cooling rate becomes faster, the amount of time that is available at each temperature step for ferrite formation is less, which delays the transformation to lower temperatures.

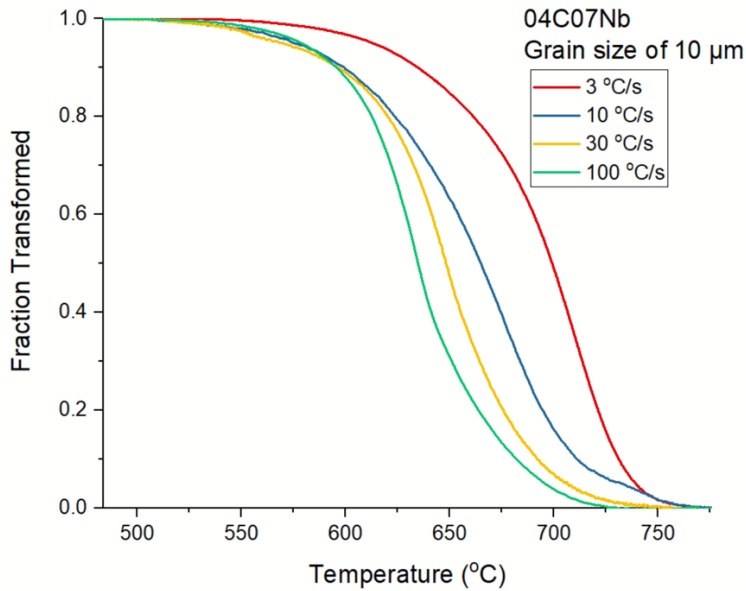


Figure 5.8 Effect of cooling rate on austenite decomposition kinetics in 04C07Nb

Austenite decomposition is also influenced by prior austenite grain sizes (PAGS). In this study, 3 different PAGSs of 10 μm , 20 μm and 40 μm for the 2C04Nb steel and 2 different PAGSs of 10 μm and 60 μm for the 04C07Nb steel were studied. Figure 5.9 shows the effect of PAGS on austenite decomposition kinetics for the 2C04Nb steel at a continuous cooling rate of 30°C/s. As illustrated in Figure 5.9, the transformation shifts to a lower temperature with increasing PAGS. With smaller PAGS, greater grain boundary area densities can be seen, hence resulting in an increase of available ferrite nucleation sites, favoring earlier transformation. This finding is consistent with various previous work [6], [54], [117]–[120].

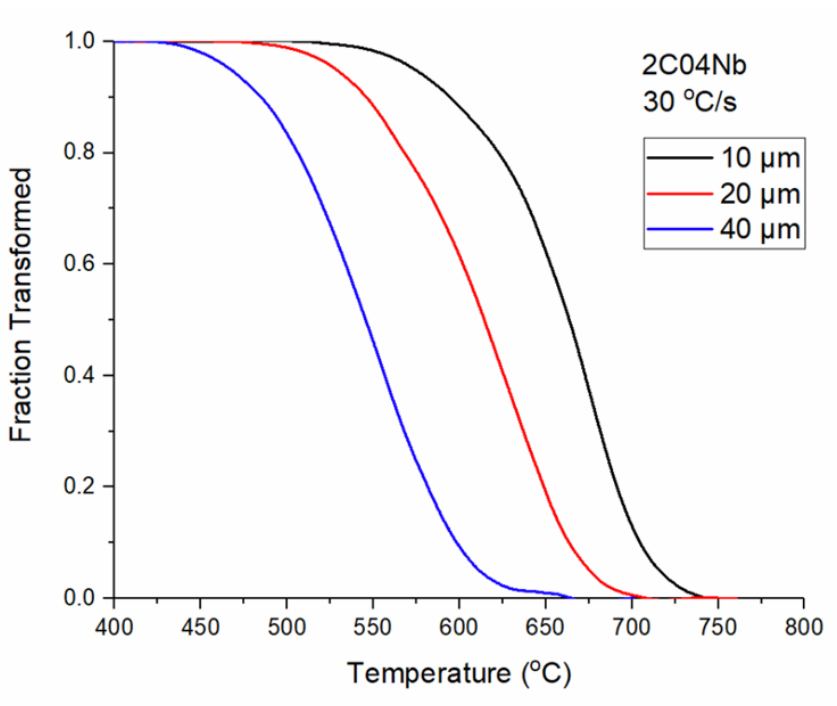


Figure 5.9 Effect of grain size on austenite decomposition kinetics in 2C04Nb

Figure 5.10 shows the 50% transformed temperature, T_{50} for both steels at various cooling rates and PAGSs. A general trend suggests that with larger PAGSs, and faster cooling rates, the 50% transformation temperatures decrease. Among the two steels, the T_{50} with PAGS of 10 μm ranges from 629°C to 729°C (undercooling of 195°C to 95°C) in 2C04Nb and 633°C to 701°C (undercooling of 217°C to 149°C) in 04C07Nb. Hence, T_{50} is found to be slightly lower in 04C07Nb in general, which is a combined effect of the microalloying addition of Nb and Mo. The effect of cooling rate is more pronounced at lower cooling rate; increasing the cooling rate from 3°C/s to 10°C/s results in a decrease of 54°C in T_{50} ; while from 30°C/s to 100°C/s, the difference is only 20°C. This observation is consistent among the two steels except for the case with PAGS of 40 μm in 2C04Nb. A significant drop of T_{50} (i.e. $T_{50} = 383^\circ\text{C}$) is noted for the case with PAGS of 40 μm at cooling rate of 100°C/s in 2C04Nb (as the transformation is in the bainitic regime).

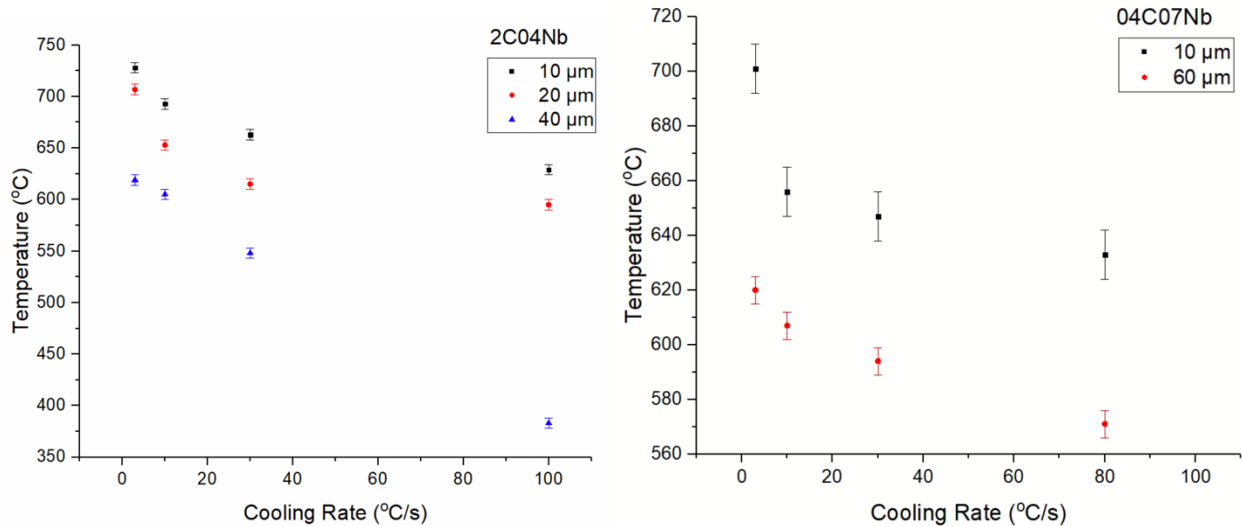


Figure 5.10 Effect of grain size and cooling rate on 50% transformation temperature for both steels (error bar calculation included in Section 5.4.1)

5.5.2 Role of retained strain

Deformation transformation tests were carried out to quantify continuous cooling transformation from pancaked austenite structures, examining the effect of retained strain with varying cooling rates and grain sizes. Figure 5.11 shows the transformation for the 2C04Nb steel with austenite grain size of 10μm for a cooling rate of 30°C/s. The result suggests that with increased retained strain, the transformation shifts to higher temperatures. This can be attributed to the increased grain boundary area and increased irregularity of grain boundaries caused by deformation, boosting potential nucleation sites available for transformation. This is in agreement with previous findings from Sakar [114] and Lottey [120].

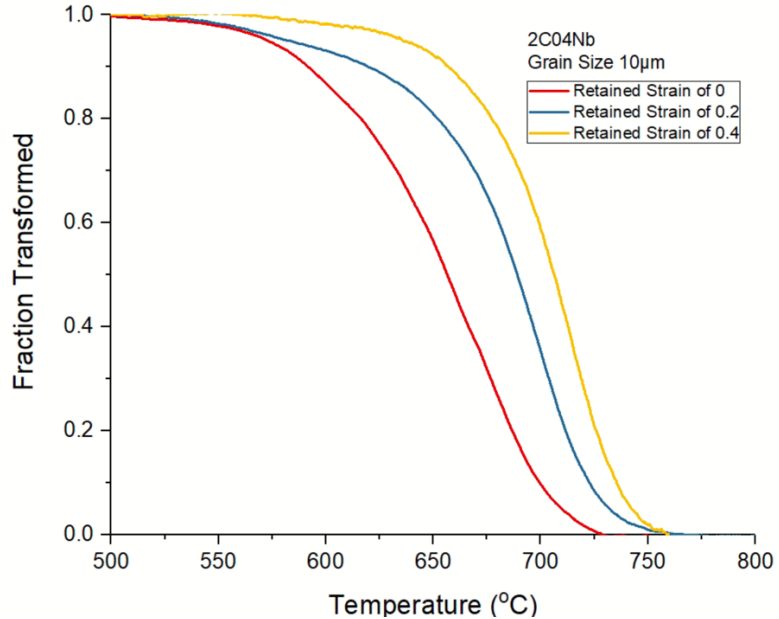


Figure 5.11 Effect of retained strain on austenite decomposition kinetics in 2C04Nb

Figure 5.12 shows the T_{50} for both steels with austenite grain size of 10µm and 20µm at various retained strains and cooling rates. As shown, in general the T_{50} is higher when retained strain is higher at any given cooling rate irrespective of the steel. However, the effect can be small and within the scatter of accuracy in selected cases.

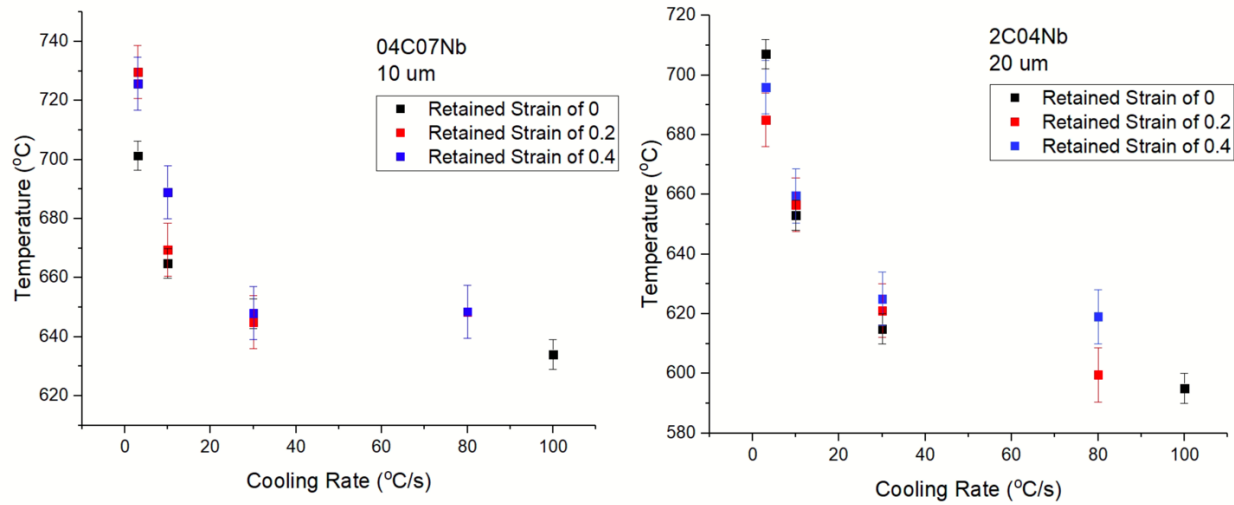


Figure 5.12 Effect of retained strain on 50% transformation temperature for both steels (error bar calculation included in Section 5.4.2)

5.5.3 Optical microstructure characterization

Figure 5.13 and Figure 5.14 show a summary of the optical micrographs obtained in the transformation samples for both steels with different PAGS, cooling rate and retained strain. Table 5.10 and Table 5.11 further provide quantification analysis for the observed microstructure products.

Three major types of microstructures are observed in these micrographs: irregular ferrite, polygonal ferrite and bainite. The transformation products are consistent with the transformation start temperatures. Ferritic structures are observed for cases with higher transformation start temperatures while bainitic structures are observed for scenarios with lower transformation start temperatures. For cases with intermediate transformation start temperatures, a mixture of ferrite and bainite is observed. It is also noted that a higher ferrite fraction was observed for the steel with lower carbon content (i.e. 04C07Nb).

Grain refinement is consistently observed with increasing cooling rate for both steels with different PAGS. Ferrite and pearlite (i.e. 04C07Nb, 10 μ m, 3°C/s and 2C04Nb, 10 μ m, 3°C/s) are observed for slow cooling rate and ferrite and bainite structures are obtained in fast cooling rate cases (i.e. 100°C/s). As seen in Figure 5.13, metallographic observation on the role of PAGS indicates that with smaller PAGS, the microstructures are more towards ferrite-pearlite transformation products; in contrast, with larger PAGS, it tends to bring ferrite structure to finer bainite structures.

A general trend of subtle increase of ferrite fraction and grain refinement is observed as retained strain increases. With deformation, there is a tendency to result in higher transformation temperature, hence forming more ferritic structures. Further quantification work will be presented. A more complicated microstructure is observed in 2C04Nb with PAGS of 40 μ m, ferrite formed on PAG boundaries, wrapping around bainite interior. For these more complex structures, electron backscattered diffraction analysis will be carried out to provide a more in-depth study, which will be detailed in section 5.5.4.

In summary, as the cooling rate increases, the transformation start temperature decreases, the microstructure transition occurs from polygonal ferrite to irregular ferrite and finally to bainite. The ferrite fraction decreases with increasing cooling rates, larger austenite grain sizes and lower retained strain.

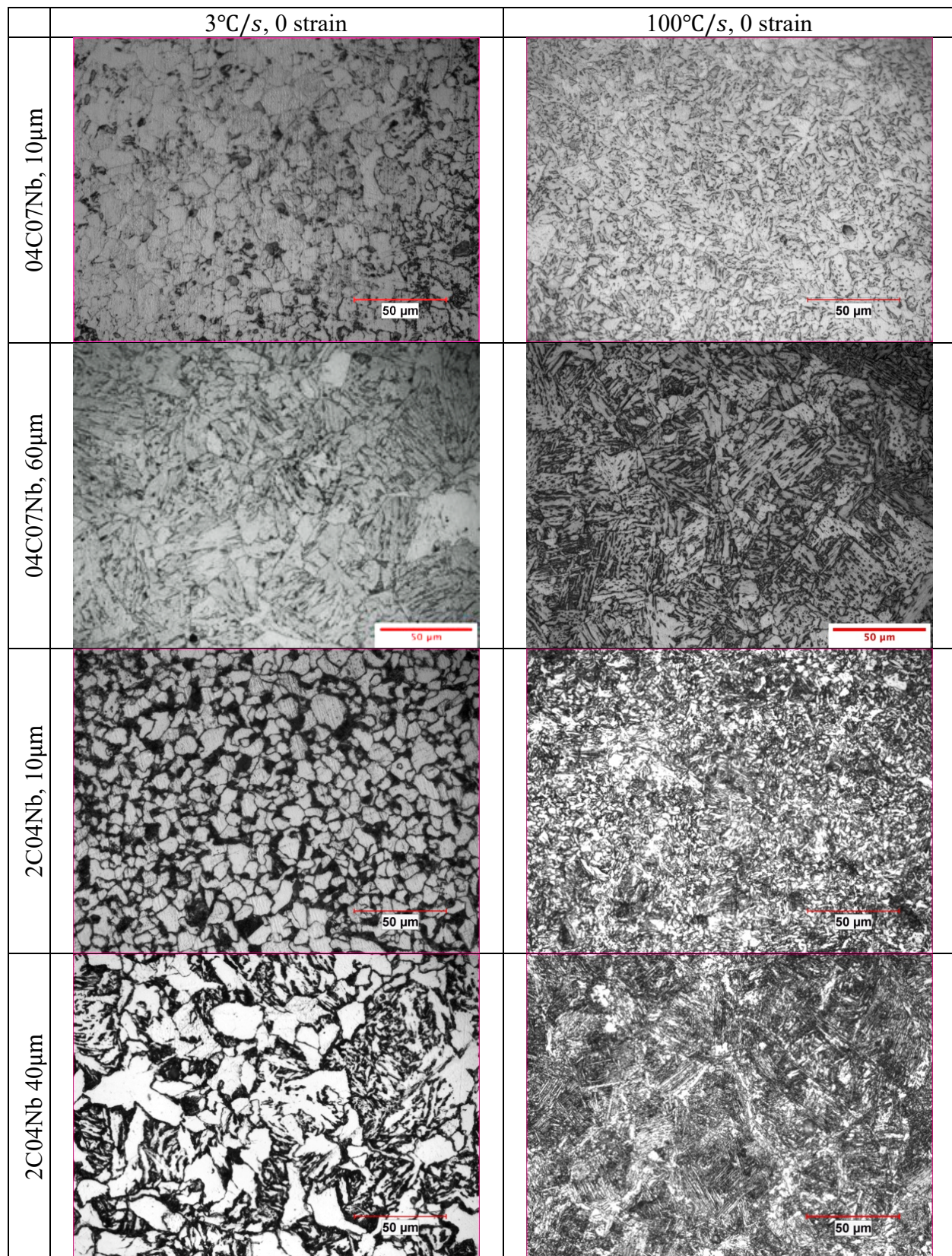


Figure 5.13 Summary of optical micrographs showing effect of grain size and cooling rate

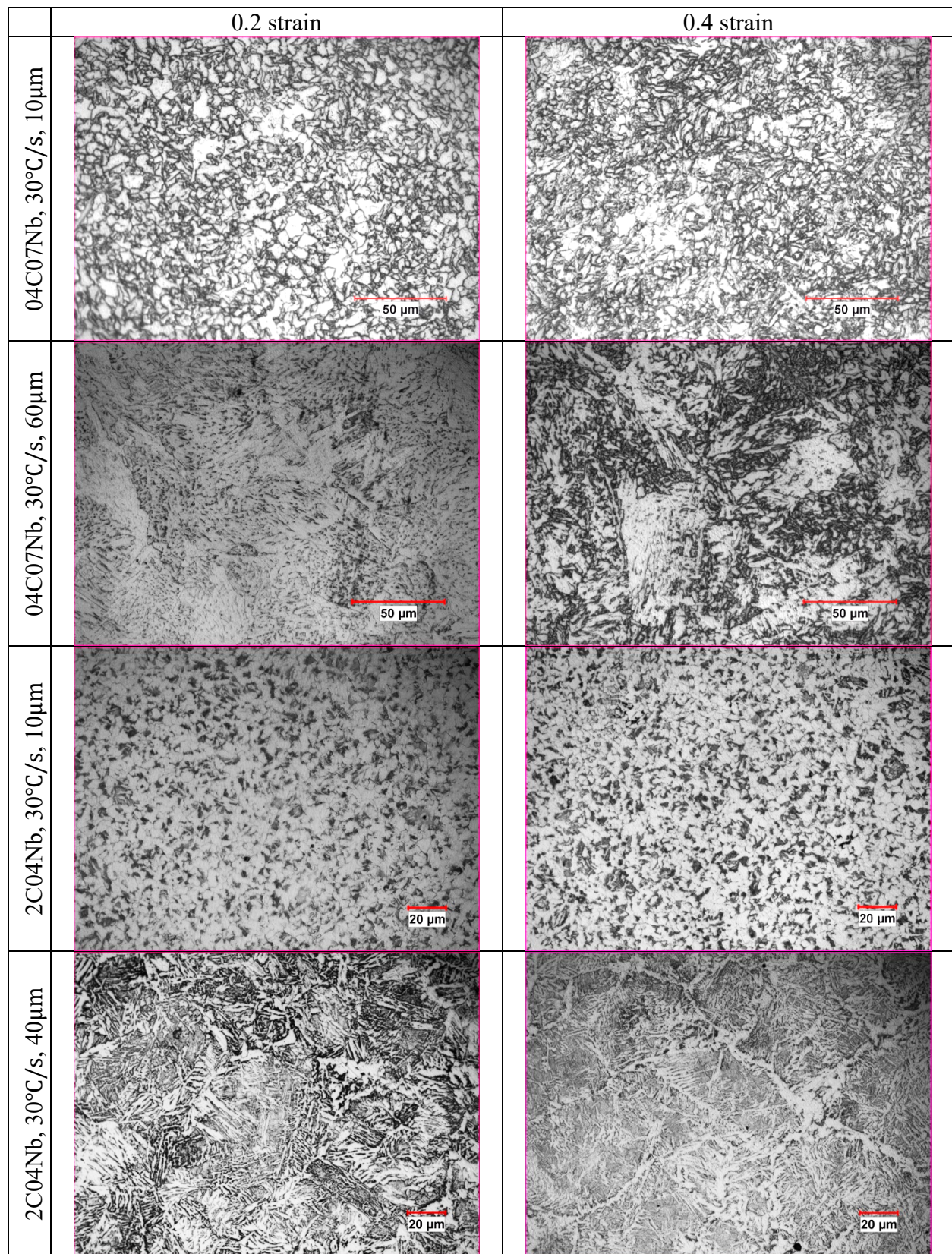


Figure 5.14 Summary of optical micrographs showing effect of retained strain

Table 5.10 shows the phase fraction analysis work done on cases with ferrite and bainite mixture with a focus on the 2C04Nb steel. It is observed that a higher ferrite fraction is obtained with increased retained strains. With higher retained strain, more potential nucleation sites are available as the grains become more pancaked, resulting in a higher ferrite fraction in the final microstructure.

Table 5.11 shows the mean EQAD of polygonal ferrite grains measurement on selected conditions where ferrite is present as the dominant feature. Ferrite grain size provides an indication of strength. As it is observed in the optical microscopy, the ferrite grain size is significantly larger in cases with slower cooling rates.

Table 5.10 Ferrite fraction quantification

Grain size (μm)	Cooling Rate ($^{\circ}\text{C}/\text{s}$)	Strain	T_5 ($^{\circ}\text{C}$)	Ferrite Fraction
40	10	0.4	719	0.57
	10	0.2	679	0.42
	30	0.4	671	0.43
	30	0.2	640	0.37
20	10	0.4	731	0.70
	10	0.2	730	0.51
	30	0.4	707	0.66
	30	0.2	703	0.53

Table 5.11 EQAD measurements of ferrite at selected conditions

Steel	PAGS (μm)	Cooling Rate ($^{\circ}\text{C}/\text{s}$)	Strain	Mean EQAD (μm)
04C07Nb	10	10	0.2	7.5
2C04Nb	20	3	0.4	13.6
2C04Nb	10	10	0.2	6.3

5.5.4 EBSD

To provide further quantification of the microstructures, EBSD characterization was performed on selected conditions (i.e. strained cases in 2C04Nb with PAGS of $20\mu\text{m}$ and $40\mu\text{m}$). Inverse pole figure (IPF) provides colored orientation maps with indication of orientation of each point in the map. The color scale represents crystallographic direction parallel to the assigned sample direction. Figure 5.15 shows the IPF of the investigated conditions for 2C04Nb. The IPFs suggests that with smaller PAGSs, the structures are blocky with more uniform color gradient; while with larger PAGSs, fine lath like structures are observed. Comparing the IPFs, it is observed that larger PAGS results in much finer and lathy microstructures, while an increase in retained strain results in higher portion of blocky-like structure.

Figure 5.16 shows the misorientation maps for the selected conditions for 2C04Nb. The maps show the outline of LAGB and HAGB: LAGB is shown in green, defined as misorientation angle of 2° - 15° ; HAGB is shown in black, defined as misorientation angle $> 15^{\circ}$. Table 5.12 provides a quantitative result of the HAGB density as well as the characteristic length scale for each condition. It is observed that increasing strain level from 0.2 to 0.4 leads to lower HAGB density indicating coarser bainitic structures for PAGS of $40\mu\text{m}$. Similarly to the $40\mu\text{m}$ case, an

increase of LAGB is evident in the case for 20 μm case going from 0.2 to 0.4 strain. In general, a more ferritic structure is observed for 20 μm and bainitic structure for 40 μm .

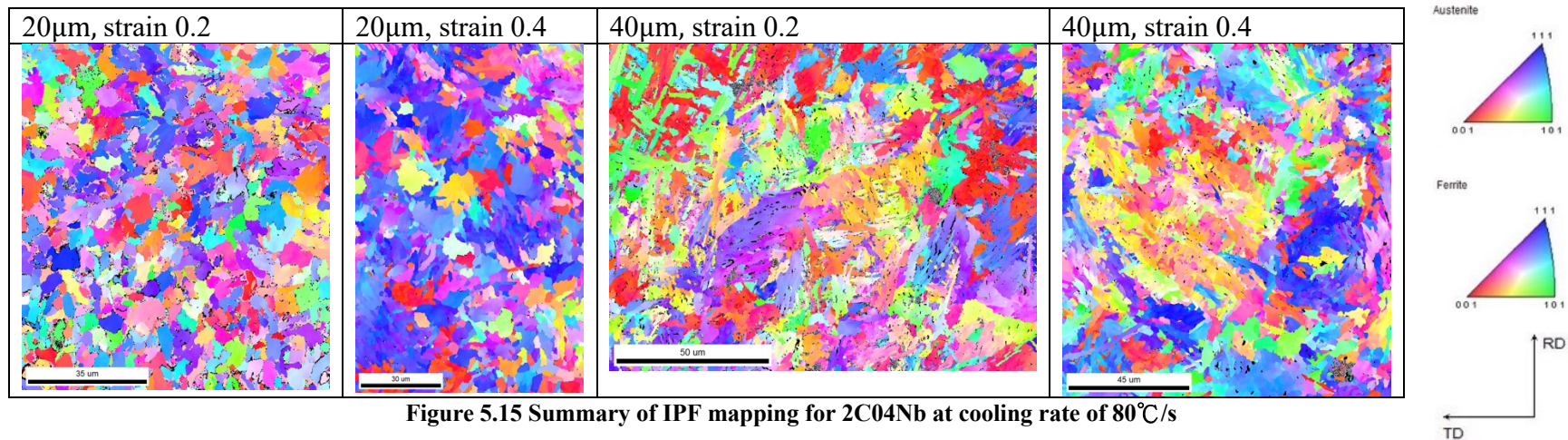


Figure 5.15 Summary of IPF mapping for 2C04Nb at cooling rate of 80°C/s

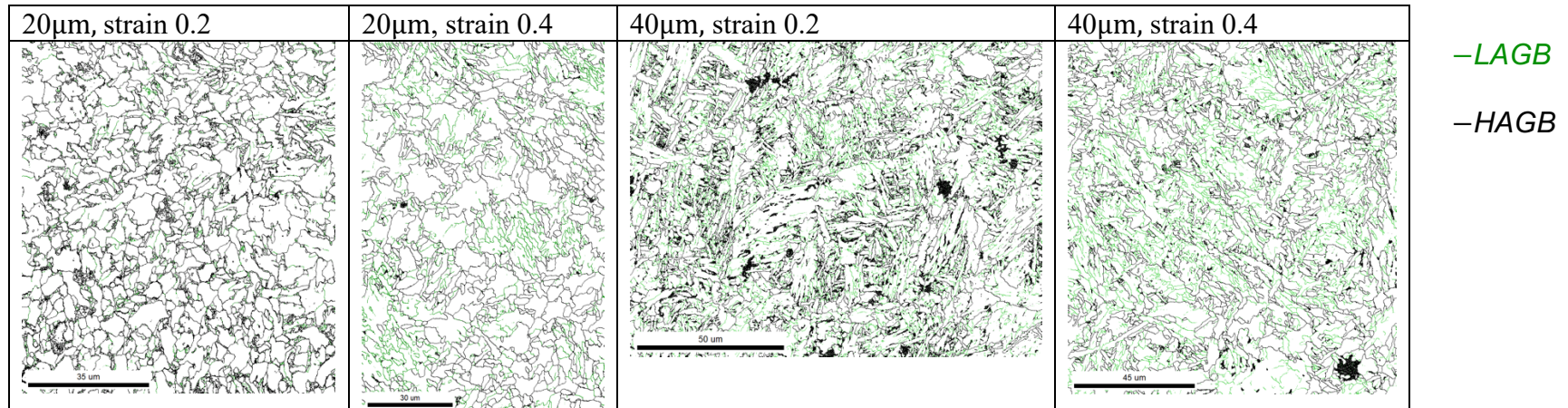


Figure 5.16 Summary of misorientation maps for 2C04Nb at cooling rate of 80°C/s

Table 5.12 Summary of misorientation analysis

	20µm, strain 0.2	20µm, strain 0.4	40µm, strain 0.2	40µm, strain 0.4
HAGB density, H (μm^{-1})	1.15	0.64	1.29	0.75
Characteristic length scale, l (μm)	0.87	1.57	0.77	1.33
LAGB density (μm^{-1})	0.21	0.39	0.63	0.59

5.5.5 Hardness

Vickers hardness was measured for all transformation samples. Figure 5.17 shows the Vickers hardness measured at various degree of deformation and cooling rates for 2C04Nb with a PAGS of $10\mu\text{m}$. The effect of retained strain between 0.2 and 0.4 is observed to be insignificant within the experimental error range. Both the strained cases are observed to have lower hardness compared to the no-strain case.

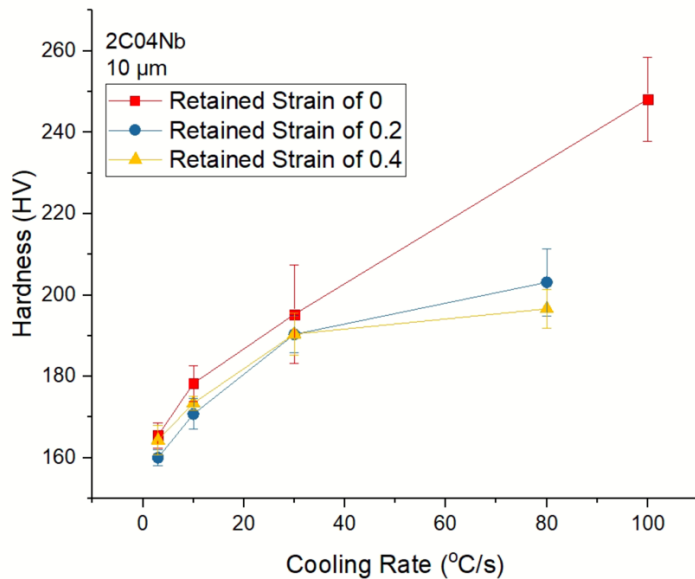


Figure 5.17 Hardness measurement on 2C04Nb with grain size of $10\mu\text{m}$ at various strain

The measured hardness of the two steels as a function of HAGB density is shown in Figure 5.18. A trend with some scatter between hardness and the square root of HAGB density is observed with an R^2 fit of 0.81; however, in detail there is some non-linearity, and it appears that steel chemistry has some effect on this trend. This trend can be described with the following equation:

$$\text{Hardness (Hv)} = 168(\text{HAGB density })^{0.5} + 101 \quad (5.1)$$

where hardness is in Hv and HAGB density is in μm^{-1}

The above equation can be presented in terms of characteristic length scale, l in μm and it is similar to a Hall-Petch like relationship.

$$\text{Hardness } (Hv) = 168(l)^{-0.5} + 101 \quad (5.2)$$

The above shows a preliminary fitting, it is observed that the intercept value can be chemistry dependent and that can be due to different solution strengthening with the different steel chemistry. This relationship shows that increased HAGB density or shorter characteristic length scale leads to higher hardness values.

From Figure 5.18, it shows that the fit starts to deviate towards higher HAGB density $> 1.0\mu\text{m}^{-0.5}$, where the outliers are conditions with fast cooling rate and larger PAGs in the steel with higher carbon content (i.e. 2C04Nb). These outliers correspond to the relatively complex microstructures with mixtures of fine ferritic grains and lathy bainitic structures being present where ferrite forms on PAGB and bainite in the grain interior. The discrepancy of the fit can be due to the complexity of the microstructures observed. It is noted that one point on the plot has a

particularly high hardness measurement of 363 ± 12 HV, this is obtained from the 2C04Nb steel with PAGS of $60\mu\text{m}$ at a cooling rate of $100^\circ\text{C}/\text{s}$ and no deformation.

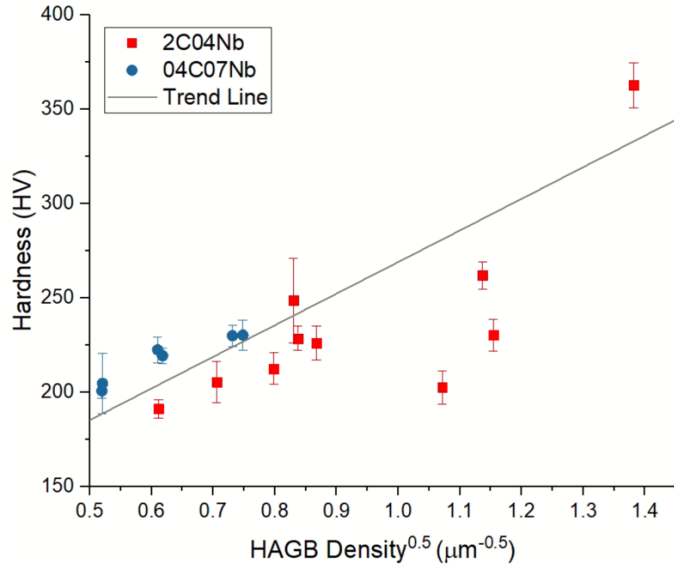


Figure 5.18 Relationship between hardness and HAGB density

Figure 5.19 includes all tested conditions, showing the relationship between hardness and transformation start temperatures. As a first approximation, a linear trend is fitted for transformation start temperature and hardness with some scatters, where higher transformation start temperature results in higher hardness in both steels:

$$\text{Hardness (Hv)} = -0.581T_5 + 607 \quad (5.3)$$

An R^2 value of 0.84 is obtained, indicating a well fitted linear trend. As seen previously, refined features and lathy bainitic structures are often observed with lower transformation start temperature, hence resulting in higher hardness values. It is seen that one data point particularly stand out in the plot with a T_5 of 500°C resulting in the highest hardness point, while this point is in a different microstructure regime (deep in bainitic), it still follows the trend of the rest of the

data points. While most data points follow within a scatter band, it is important to note that a 50HV scatter could introduce a difference of 150MPa in strength, which is non-negligible.

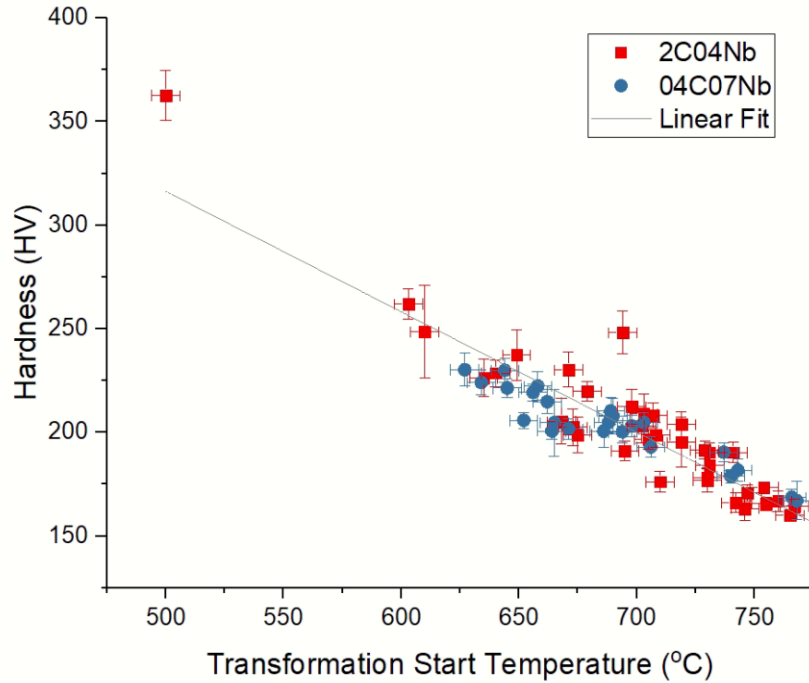


Figure 5.19 Relationship between hardness and transformation start temperature in all tested conditions

5.6 Modelling

5.6.1 Overview

From the previous section, two major types of microstructures were observed: ferrite and bainite. As a result, an austenite decomposition model was created to help describe the phase transformation behavior observed with a focus on cases with pancaked austenite features, consisting of two sub models: ferrite start and ferrite/bainite growth kinetics.

5.6.2 Ferrite start model

To describe transformation start, the ferrite transformation start model proposed by Militzer et al. [69], [70] is applied here. The model assumes early growth of corner nucleated ferrite controlled by carbon diffusion at T_N , with continuous growth until critical carbon enrichment of c^* is reached [121].

The growth rate of corner nucleated ferrite can be described by

$$\frac{dR_f}{dT} \frac{dT}{dt} = D_c \frac{c_\gamma - c^0}{c_\gamma - c_\alpha} \frac{1}{R_f} \quad (5.4)$$

where R_f is the radius of the growing ferrite grain, D_c is the carbon diffusivity in austenite, c_γ and c_α are the equilibrium carbon concentration in austenite and ferrite respectively and c^0 is the average carbon bulk concentration.

The carbon diffusivity, D_c , in austenite can be represented by the Arrhenius equation:

$$D_c = D_0^C \exp\left(\frac{-Q_D^C}{RT}\right) \quad (5.5)$$

where D_0^C represents the pre-exponential diffusivity term of carbon, Q_D^C represents the activation energy of carbon diffusion in austenite, R is the gas constant and T is absolute temperature.

Nucleation site saturation is achieved when the following condition is met:

$$R_f > \frac{d_\gamma}{\sqrt{2}} \frac{c^* - c_0}{c_\gamma - c^0} \quad (5.6)$$

where d_γ is the austenite grain size, and c^* is a fitted parameter representing a critical carbon concentration above which further ferrite nucleation at PAGBs is postulated to not occur.

With a constant cooling rate, φ , transformation start temperatures can be modelled by combining Equation (5.4) and (5.6):

$$c^* - c^0 = \frac{2(c_\gamma - c^0)}{\varphi^{\frac{1}{2}} d_\gamma} \sqrt{\int_{T_s}^{T_N} D_c \frac{c_\gamma - c^0}{c_\gamma - c_\alpha} dT} \quad (5.7)$$

In this study, the fitting parameter c^* was optimized using a least square method based on transformation test results at various cooling rates, austenite grain sizes and two different steel chemistries.

Table 5.13 provides a summary of the parameters used in the model. Figure 5.20 and Figure 5.21 compare the model calculated data with the experimental data for 04C07Nb and 2C04Nb, respectively. The model captures the effect of varying cooling rates and austenite grain sizes for cases with ferrite as the dominant microstructure. The results show that the model accurately describes the majority of the experimental data within the error of measurements.

Table 5.13 Summary of parameters used in the ferrite start model

Steel	Strain	Nucleation Temperature (°C)	c^*/c_0
04C07Nb	0.2	800	3.19
04C07Nb	0.4	800	2.93
2C04Nb	0.2	774	1.35
2C04Nb	0.4	774	1.26

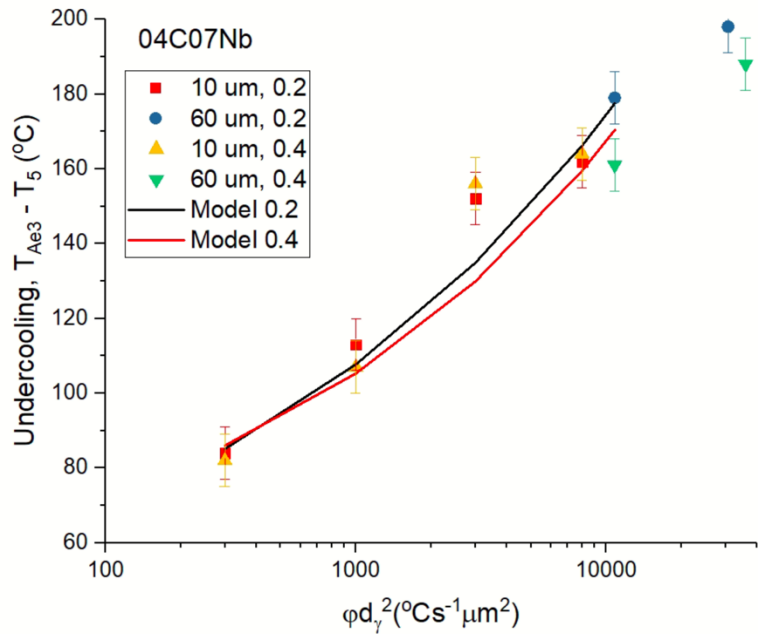


Figure 5.20 Summary of the resulting ferrite start modelled data with corresponding experimental data for 04C07Nb

04C07Nb

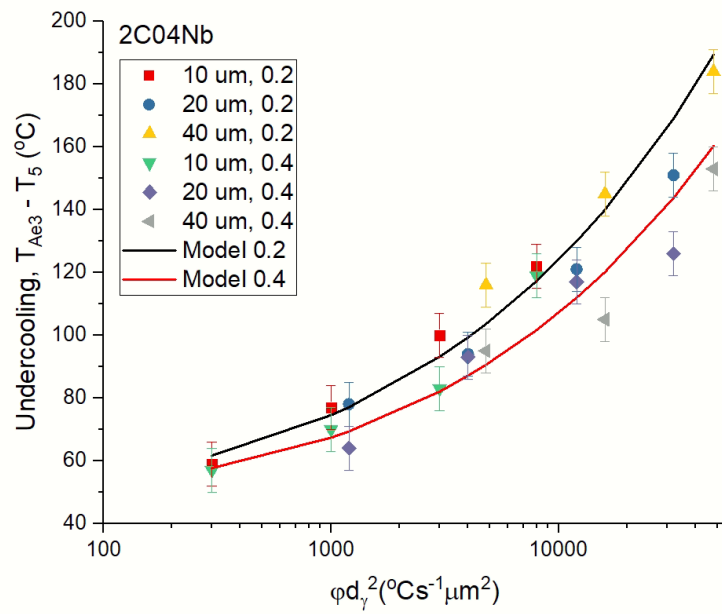


Figure 5.21 Summary of the resulting ferrite start modelled data with corresponding experimental data for 2C04Nb

2C04Nb

5.6.3 Growth kinetics

Ferrite and bainite growth kinetics were modelled using the Johnson-Mehl-Avrami-Kolmogorov (JMAK) model in combination with the additivity rule.

The traditional JMAK equation is:

$$X = 1 - \exp(-bt^n) \quad (5.8)$$

where X is the output of the model, fraction transformed, b is the rate parameter, t is the time at transformation temperature and n is the JMAK exponent. n was varied between 0.5 and 1.0 in order to determine a value where b becomes independent of cooling rate. Modelled b values were determined through a relationship between $\ln(b)$ and temperature using experimental transformation data.

$$b = \left(\frac{dX}{dt} \right)^n \left(n \left(\ln \left(\frac{1}{1-X} \right) \right)^{\frac{n-1}{n}} (1-X) \right)^{-n} \quad (5.9)$$

With the modelled b values, fraction transformed per unit time can hence be obtained as follows:

$$\frac{dX}{dt} = b^{\frac{1}{n}} n \left(\ln \left(\frac{1}{1-X} \right) \right)^{\frac{n-1}{n}} (1-X) \quad (5.10)$$

The present experimental data can be best described using a n value of 0.5, which was also previously reported by Gerami [73]. The temperature dependent rate parameter, b can be described with either a parabolic relationship or a linear relationship depending on transformation temperature. Table 5.14 summarizes the fitting parameters used to calculate $\ln(b)$ with Equation (5.11) where a parabolic relationship is used to describe cases with ferrite bainite mixtures while a linear relationship is used for cases with primarily ferrite structures. It is noted

that some cases share the same fitting parameters as the effect of retained strain is deemed minor in $\ln(b)$.

$$\ln(b) = \beta_3 T^2 + \beta_2 T + \beta_1 \quad (5.11)$$

Table 5.14 Summary of JMAK fit parameters

	β_3	β_2	β_1
04C07Nb, 10 μm , $\varepsilon = 0.2, 0.4$	-2.67×10^{-4}	3.18×10^{-1}	-9.40×10^1
2C04Nb, 10 μm , $\varepsilon = 0.2$	1.54×10^{-4}	1.82×10^{-1}	-5.28×10^1
2C04Nb, 10 μm , $\varepsilon = 0.4$	1.33×10^{-4}	1.61×10^{-1}	4.80×10^1
2C04Nb, 20 μm , $\varepsilon = 0.2, 0.4$	0	-1.83×10^{-2}	1.09×10^1
2C04Nb, 40 μm , $\varepsilon = 0.2$	0	-3.26×10^{-2}	1.84×10^1
2C04Nb, 40 μm , $\varepsilon = 0.4$	0	-1.82×10^{-2}	1.03×10^1

Figure 5.22 shows a comparison of the JMAK fit model with the experimental data of the case with PAGS of 20 μm and retained strain of 0.2 in 2C04Nb. The growth model shown is based on the experimental T_5 values. As seen in the figure, the modelled results are in close agreement with the experimental results for most part of the transformation. Slight disagreement of less than 10°C was observed past the 70% transformation point for the case with PAGS of 20 μm in 2C04Nb with retained strain of 0.2 at cooling of 3°C/s.

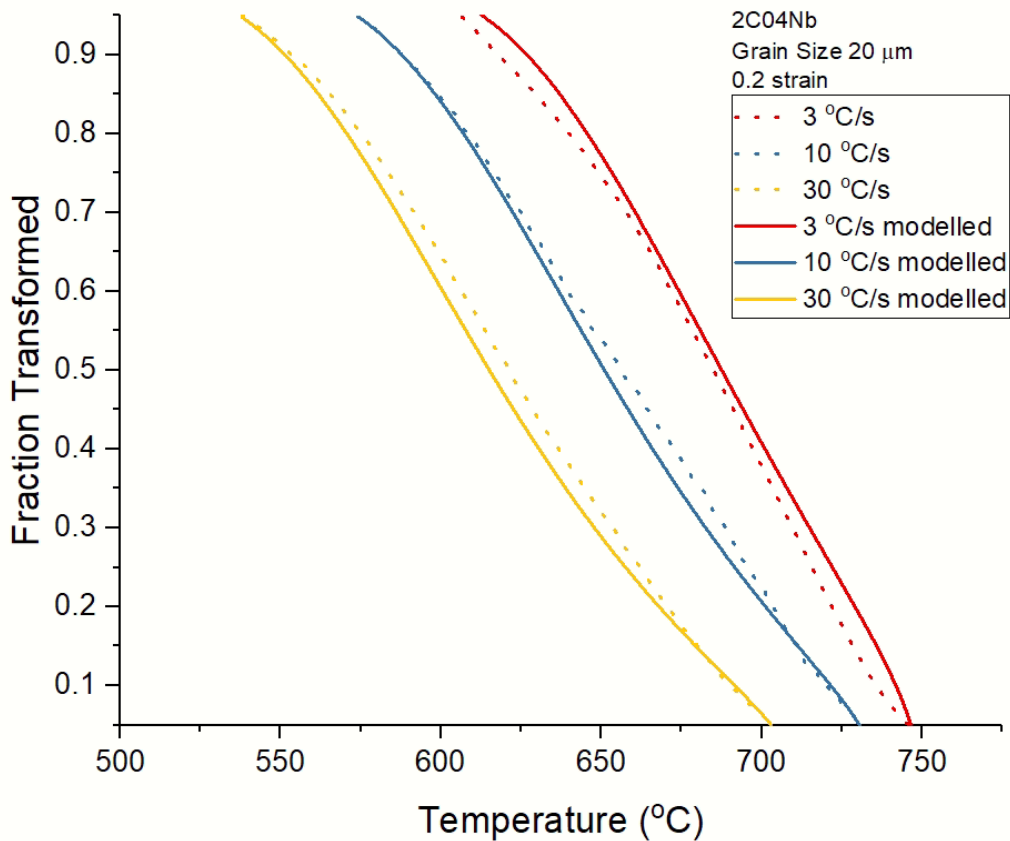


Figure 5.22 Comparison between JMAK modelled data and experimentally measured transformation kinetics for cases with PAGS of 20 μm in 2C04Nb with 0.2 retained strain

Figure 5.23 shows a summary of the proposed model compared to the experimental T_{50} results, the offset covers the experimental error of $\pm 9^\circ\text{C}$. The model shown here is a combination of the transformation start and JMAK growth model, i.e. the T_5 obtained from the transformation start model was further applied in the growth model. It focuses on cases with cooling rates ranging from $10^\circ\text{C}/\text{s}$ to $80^\circ\text{C}/\text{s}$ which are of significance for runout table application. Good reproduction was observed with the majority of data points lying within the error deviation. An outlier is observed for the case with a PAGS of $10\mu\text{m}$, cooling rate of $10^\circ\text{C}/\text{s}$ and 0.2 retained

strain in the 2C04Nb steel. A discrepancy of 35°C was seen with the modelled T_{50} of 683°C and the experimental T_{50} of 718°C.

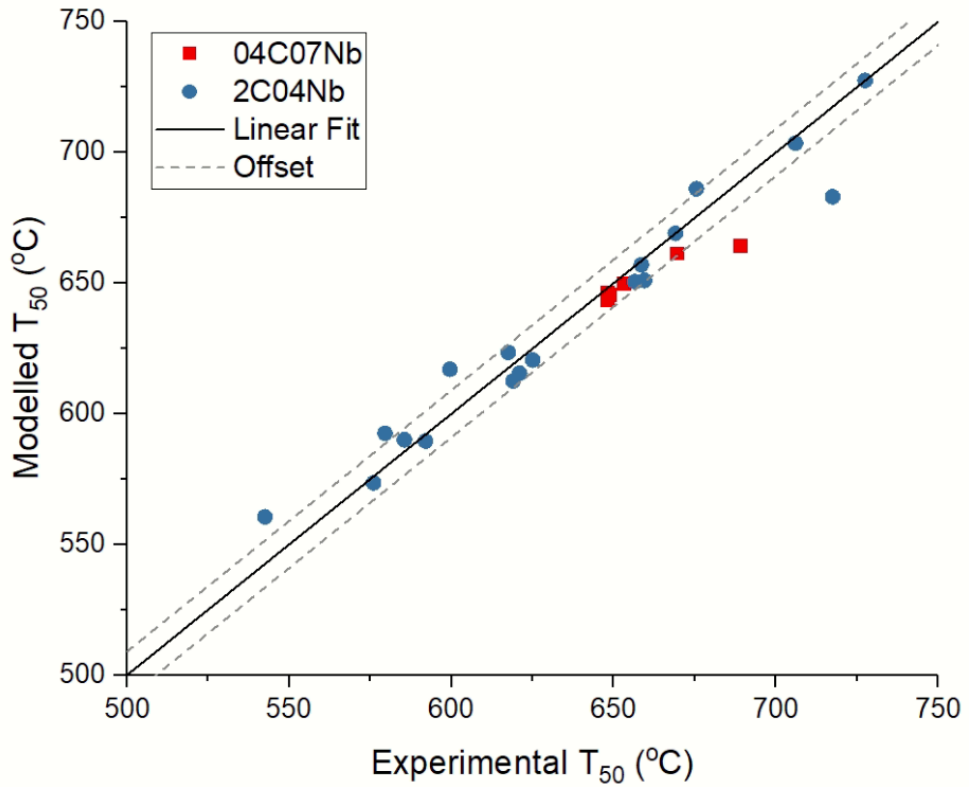


Figure 5.23 Comparison of T_{50} obtained from the JMAK modelling approach with the measurement results (offset calculation included in Section 5.4.2)

Chapter 6: Conclusions and future work

6.1 Conclusions and summary

A series of continuous cooling tests have been conducted on two low-carbon steels to quantify the continuous cooling phase transformation kinetics using Gleeble 3500 thermomechanical simulator. The objective of the study was to examine the role of various processing parameters including 1) PAGS 2) cooling rate and 3) retained strain on transformation kinetics and the final decomposition products. To select the appropriate reheat conditions for subsequent tests, *in-situ* austenite grain size measurement were completed using the LUMet system. Dilation measurements were captured to study the austenite decomposition kinetics along with microstructure characterization completed with optical microscopy and electron backscattered diffraction. The mechanical property of the final structure was evaluated through hardness testing using a micro-Vickers indenter. With the experimental results, a phenomenological model of the austenite decomposition kinetics was also developed. This model consists of two sub-models: ferrite start and ferrite/bainite growth kinetics, both of which have shown to be capable of replicating experimentally observed kinetics with adequate accuracy.

Based on the conducted austenite decomposition experiments, the key findings of this thesis can be summarized as follows:

1. Austenite decomposition kinetics and products are strongly influenced by cooling rate. It was found that as cooling rate increases, transformation temperature decreases. Grain refinement was also observed with faster cooling rate, where ferrite structures were more predominate with slower cooling rate and beyond a certain cooling rate, bainitic structures were more commonly seen.

2. PAGS showed an inverse relationship with transformation temperature, i.e. large PAGS led to lower transformation temperatures. Microstructure characterization has shown that smaller PAGS promoted the production of equilibrium transformation products such as polygonal ferrite.
3. The effect of deformation was examined, where with more retained strain, transformation temperature was higher, due to increased nucleation site density. As a result of the increased transformation temperature, ferrite fraction was also higher with more deformation.
4. Hardness measurements were found to be strongly impacted by cooling rate. With higher cooling rate, grain refinement was observed, resulting in higher hardness readings. The effect of retain strain on the other hand was less significant on hardness results.
5. A linear trend between hardness measurements and the square root of HAGB density was observed with steel chemistry dependency. By taking an inverse of the HAGB density, a characteristic length scale, l can be obtained, and it indicated a Hall-Petch like relationship between hardness and grain size.
6. A linear increase of hardness values was observed with decreasing transformation start temperature.
7. A transformation start model was developed, assuming early growth of corner nucleated ferrite grains, providing prediction on austenite to ferrite transformation start temperature. The model calculated transformation start temperatures agree within the experimental error of $\pm 9^\circ\text{C}$ with the experimental results.
8. A JMAK model adapting the additivity rule was employed to model the kinetics of subsequent ferrite and bainite growth, capturing the effects of PAGS, cooling rate and

retained strain. The model has shown to be within the measurement accuracy of the experimental CCT test data.

6.2 Future work

The present research generated a systematic study on the microstructure phase transformation during continuous cooling on two low-carbon steels, and further work is needed to improve and extend knowledge on the current topic. A few suggestions for future work are as follows:

1. The current study provided investigation on two steel types, a more in-depth study involving more steels should be conducted to examine quantitatively the role of different alloying elements on austenite decomposition for typical or potential steel chemistries relevant for high-performance low-carbon steels.
2. Since the final product microstructures critically determine the resulting properties, it is recommended that a more detailed microstructure characterization analysis is to be done for complex ferrite-bainite steels. This can include more in-depth characterization by EBSD such as Bain group analysis to distinguish upper and lower bainite.
3. Mechanical testing beyond hardness measurements will be essential to establish improved structure-property relationships. The mechanical properties of interest include yield and tensile strength, uniform and total elongation, ductile-brittle transition temperatures as well as Charpy impact toughness. The relationship between these mechanical properties and the transformation kinetics and products are to be analyzed. To achieve the overall goal of the wider project that this study is a part of, future work focusing on heat transfer behavior during accelerated cooling is needed to improve knowledge on the overall understanding of industrial runout table and to develop

fundamental runout table process models providing insights on process control. Additional work is to be done to incorporate the current phase transformation models into the runout table cooling model. The combined model should then be validated and verified with dedicated pilot-scale tests as well as industrial data.

Bibliography

- [1] World Steel Association, “Steel statistical yearbook 2020 Extended Version,” 2020.
- [2] World Steel Association, “Worldsteel short range outlook June 2020,” Brussels, Belgium, 2020. [Online]. Available: <https://www.worldsteel.org/media-centre/press-releases/2020/worldsteel-short-range-outlook-june-2020.html>.
- [3] International Energy Agency, “Global energy demand grew by 2.1% in 2017, and carbon emissions rose for the first time since 2014,” 2018.
- [4] I. Tamura, H. Sekine, T. Tanaka, and C. Ouchi, *Thermomechanical processing of high-strength low-alloy steels*. 1988.
- [5] K. E. Porter, David A.; Easterling, *Phase transformations in metals and alloys*, Third Edit. CRC Press, 1992.
- [6] R. Tafteh, “Austenite decomposition in an X80 linepipe steel,” M.A.Sc Thesis, The University of British Columbia, Vancouver, 2008.
- [7] P. Petkov, “Austenite decomposition of low carbon high strength steels during continuous cooling,” M.A.Sc Thesis, The University of British Columbia, Vancouver, 2004.
- [8] I. D. G. Robinson, “Grain growth and austenite decomposition in two niobium containing high strength line pipe steels,” M.A.Sc Thesis, The University of British Columbia, Vancouver, 2016.
- [9] R. Pandi, “Modelling of austenite to ferrite transformation behaviour in Low Carbon Steels during run out table cooling,” PhD Thesis, The University of British Columbia, Vancouver, 1998.
- [10] A. K. Giumelli, “Austenite grain growth kinetics,” M.A.Sc Thesis, The University of British Columbia, Vancouver, 1995.

- [11] Standard Council of Canada, *CSA Z245.1-14 steel pipe*. 2014.
- [12] American Petroleum Institute, *API 5L Specification for line pipe*, 48th ed. .
- [13] J. W. Cahn, “The impurity-drag effect in grain boundary motion,” *Acta Metall.*, vol. 10, no. 9, pp. 789–798, 1962, doi: 10.1016/0001-6160(62)90092-5.
- [14] M. Enomoto, N. Nojiri, and Y. Sato, “Effects of vanadium and niobium on the nucleation kinetics of proeutectoid ferrite at austenite grain boundaries in Fe-C and Fe-C-Mn alloys,” *Mater. Trans. JIM*, vol. 35, no. 12, pp. 859–867, 1994, doi: 10.2320/matertrans1989.35.859.
- [15] M. Buhler, G. R. Gomez, and T. Pérez, “Effect of Nb in solid solution on the austenite decomposition kinetic of a V-Nb-Ti microalloyed steel,” *Super-High Strength Steels*, pp. 1–10, 2005.
- [16] A. J. DeArdo, C. I. Garcia, and E. J. Palmiere, “Thermomechanical processing of steels,” *ASM Handb.*, vol. 4, no. 5, pp. 237–255, 1991, doi: 10.3390/met10050641.
- [17] C. Fossaert, G. Rees, T. Maurickx, and H. Bhadeshia, “The effect of niobium on the hardenability of microalloyed austenite,” *Metall. Mater. Trans. A*, vol. 26, no. 1, pp. 21–30, 1995.
- [18] F. Boratto, R. Barbosa, S. Yue, and J. J. Jonas, “Effect of chemical composition on the critical temperatures of microalloyed steels,” in *International Conference on Physical Metallurgy of Thermomechanical Processing of Steels and Other Metals*, 1988, vol. 1, pp. 383–390.
- [19] D. Q. Bai, S. Yue, W. P. Sun, and J. J. Jonas, “Effect of deformation parameters on the no-recrystallization temperature in Nb-bearing steels,” *Metall. Trans. A*, vol. 24, no. 10, pp. 2151–2159, 1993, doi: 10.1007/BF02648589.

- [20] S. Vervynckt, K. Verbeken, B. Lopez, and J. J. Jonas, “Modern HSLA steels and role of non-recrystallisation temperature,” *Int. Mater. Rev.*, vol. 57, no. 4, pp. 187–207, 2012, doi: 10.1179/1743280411Y.0000000013.
- [21] A. I. Fernández, P. Uranga, B. López, and J. M. Rodriguez-Ibabe, “Dynamic recrystallization behavior covering a wide austenite grain size range in Nb and Nb-Ti microalloyed steels,” *Mater. Sci. Eng. A*, vol. 361, no. 1–2, pp. 367–376, 2003, doi: 10.1016/S0921-5093(03)00562-8.
- [22] Y. Adachi, K. Hakata, and K. Tsuzaki, “Crystallographic analysis of grain boundary BCC-precipitates in a Ni-Cr alloy by FESEM/EBSD and TEM/Kikuchi line methods,” *Mater. Sci. Eng. A*, vol. 412, no. 1–2, pp. 252–263, 2005, doi: 10.1016/j.msea.2005.09.033.
- [23] M. Toloui, “Microstructural evolution in the HAZ of X80 linepipe steel: phase field modelling,” PhD Thesis, The University of British Columbia, Vancouver, 2015.
- [24] D. G. Kurdjumow and G. Sachs, “Über den Mechanismus der Stahlhärtung (On the mechanism of hardening of steel),” *Z. Phys.*, vol. 64, no. 325–343, 1930.
- [25] G. Wassermann, “Über den Mechanismus der $\alpha \rightarrow \gamma$ Umwandlung des Eisens (On the mechanism of the $\alpha \rightarrow \gamma$ transformation of iron),” *Mitteilungen aus dem Kaiser Wilhelm Inst. für Eisenforsch.*, vol. 185, no. 590–598, 1935.
- [26] A. B. Greninger and A. R. Troiano, “The mechanism of martensite formation,” *Met. Trans.*, vol. 185, no. 590–598, 1949.
- [27] W. F. Lange, M. Enomoto, and H. I. Aaronson, “The kinetics of ferrite nucleation at austenite grain boundaries in Fe-C alloys,” *Metall. Trans. A*, vol. 19, no. 3, pp. 427–440, 1988, doi: 10.1007/BF02649256.
- [28] W. Huang and M. Hillert, “The role of grain corners in nucleation,” *Metall. Mater. Trans.*

A Phys. Metall. Mater. Sci., vol. 27, no. 2, pp. 480–483, 1996, doi: 10.1007/BF02648428.

- [29] M. Hillert, “The formation of pearlite,” in *Decomposition of Austenite by Diffusional Process*, 1962.
- [30] H. I. Aaronson and H. A. Domian, “Partition of alloying elements between austenite and proeutectoid ferrite or bainite,” *AIME*, vol. 236, pp. 781–796, 1966.
- [31] D. E. Coates, “Diffusional growth limitation and hardenability,” *Metall. Trans.*, vol. 4, no. 10, pp. 2313–2325, 1973, doi: 10.1007/BF02669370.
- [32] G. Krauss and S. W. Thompson, “Ferritic microstructures in continuously cooled low- and ultralow-carbon steels,” *ISIJ Int.*, vol. 35, no. 8, pp. 937–945, 1995, doi: 10.2355/isijinternational.35.937.
- [33] P. Cizek, B. P. Wynne, C. H. J. Davies, B. C. Muddle, and P. D. Hodgson, “Effect of composition and austenite deformation on the transformation characteristics of low-carbon and ultralow-carbon microalloyed steels,” *Metall. Mater. Trans. A Phys. Metall. Mater. Sci.*, vol. 33, no. 5, pp. 1331–1349, 2002, doi: 10.1007/s11661-002-0059-8.
- [34] F. Zhang, Y. Zhao, Y. Tan, X. Ji, and S. Xiang, “Study on the nucleation and growth of pearlite colony and impact toughness of eutectoid steel,” *Metals (Basel)*, vol. 9, no. 11, 2019, doi: 10.3390/met9111133.
- [35] M. Wang *et al.*, “Microstructure, mechanical properties, and strain-hardening behavior of V–N microalloyed pipeline steels consisted of polygonal ferrite and acicular ferrite,” *Steel Res. Int.*, vol. 92, no. 3, pp. 1–10, 2021, doi: 10.1002/srin.202000404.
- [36] L. Wang, S. V. Parker, A. J. Rose, G. D. West, and R. C. Thomson, “Modelling of Nb influence on phase transformation behaviours from austenite to ferrite in low carbon steels,” *Model. Simul. Mater. Sci. Eng.*, vol. 24, no. 3, 2016, doi: 10.1088/0955-

- [37] C. Ekinci, N. Ucar, A. Calik, S. Karakas, and I. Akkurt, “Effects of heat treatment on the microstructure and mechanical properties of low-carbon microalloyed steels,” *High Temp. Mater. Process.*, vol. 30, no. 1–2, pp. 39–42, 2011, doi: 10.1515/HTMP.2011.005.
- [38] S. J. Jia, B. Li, Q. Y. Liu, Y. Ren, S. Zhang, and H. Gao, “Effects of continuous cooling rate on morphology of granular bainite in pipeline steels,” *J. Iron Steel Res. Int.*, vol. 27, no. 6, pp. 681–690, 2020, doi: 10.1007/s42243-019-00346-3.
- [39] K. R. Carpenter and C. R. Killmore, “The effect of Nb on the continuous cooling transformation curves of ultra-thin strip CASTRIPI[©] steels,” *Metals (Basel)*, vol. 5, no. 4, pp. 1857–1877, 2015, doi: 10.3390/met5041857.
- [40] N. Isasti, D. Jorge-Badiola, M. L. Taheri, B. López, and P. Uranga, “Effect of composition and deformation on coarse-grained austenite transformation in Nb-Mo microalloyed steels,” *Metall. Mater. Trans. A Phys. Metall. Mater. Sci.*, vol. 42, no. 12, pp. 3729–3742, 2011, doi: 10.1007/s11661-011-0624-0.
- [41] F. R. Xiao *et al.*, “Challenge of mechanical properties of an acicular ferrite pipeline steel,” *Mater. Sci. Eng. A*, vol. 431, no. 1–2, pp. 41–52, 2006, doi: 10.1016/j.msea.2006.05.029.
- [42] Y. Smith, A. Coldren, and R. Cryderman, “Toward improved ductility and toughness,” *Tokyo Climax Molybdenum Co. Ltd*, pp. 119–142, 1972.
- [43] H. S. Fang, Y. K. Zheng, Z. G. Yang, and B. Z. Bai, “Creation of air-cooled Mn series bainitic steels,” *J. Iron Steel Res. Int.*, vol. 15, no. 6, pp. 1–9, 2008, doi: 10.1016/S1006-706X(08)60257-5.
- [44] G. Krauss, “Steels: processing, structure, and performance,” *ASM Int.*, 2015.
- [45] H. Xiao *et al.*, “Characterization of microstructure in high-hardness surface layer of low-

carbon steel," *Metals (Basel)*., vol. 10, no. 8, pp. 1–10, 2020, doi: 10.3390/met10080995.

- [46] H. K. D. H. Bhadeshia and J. W. Christian, "Bainite in steels," *Metall. Trans. A*, vol. 21, no. 3, pp. 767–797, 1990, doi: 10.1007/BF02656561.
- [47] Y. K. Lee, "Empirical formula of isothermal bainite start temperature of steels," *J. Mater. Sci. Lett.*, vol. 21, no. 16, pp. 1253–1255, 2002.
- [48] T. Kunitake and Y. Okada, "The estimation of bainite transformation temperatures in steels by the empirical formulas," *Tetsu-to-Hagane*, vol. 84, no. 2, pp. 137–141, 1998.
- [49] J. S. Kirkaldy and D. Venugopalan, "Phase transformations in ferrous alloys," in *TMS-AIME*, 1984, pp. 125–148.
- [50] Z. Lawrynowicz, "Transition from upper to lower bainite in Fe-C-Cr steel," in *Materials Science and Technology*, 2004, vol. 20, no.11, pp. 1447–1454.
- [51] L. Habraken and M. Economopoulos, *Bainitic microstructures in low carbon alloy steels and their mechanical properties*. 1967.
- [52] Z.-G. Yang and H.-S. Fang, "An overview on bainite formation in steels," *Curr. Opin. Solid State Mater. Sci.*, vol. 9, no. 6, pp. 277–286, 2005.
- [53] W. Johnson and R. Mehl, "Reaction kinetics in processes of nucleation and growth," *Trans. Am. Inst. Min. Metall. Eng.*, vol. 135, no. 416–442, 1939.
- [54] J. M. Reichert, "Structure and properties of complex transformation products in Nb/Mo-microalloyed steels," PhD Thesis, The University of British Columbia, Vancouver, 2016.
- [55] X. Y. Long, J. Kang, B. Lv, and F. C. Zhang, "Carbide-free bainite in medium carbon steel," *Mater. Des.*, vol. 64, pp. 237–245, 2014, doi: 10.1016/j.matdes.2014.07.055.
- [56] N. Takayama, G. Miyamoto, and T. Furuhara, "Effects of transformation temperature on variant pairing of bainitic ferrite in low carbon steel," *Acta Mater.*, vol. 60, no. 5, pp.

2387–2396, 2012, doi: 10.1016/j.actamat.2011.12.018.

- [57] T. B. Massalski, “Phase Transformations,” in *ASM Seminar 1968*, 1970, p. 433.
- [58] Z. Nishiyama, *Martensitic transformation*. Elsevier, 2012.
- [59] A. G. Khachaturyan, *Theory of structural transformations in solids*. Courier Corporation, 2013.
- [60] J. Trzaska, “Calculation of critical temperatures by empirical formulae,” *Arch. Metall. Mater.*, vol. 61, 2016.
- [61] Y. Li and T. N. Baker, “Effect of morphology of martensite-austenite phase on fracture of weld heat affected zone in vanadium and niobium microalloyed steels,” *Mater. Sci. Technol.*, vol. 26, no. 9, pp. 1029–1040, 2010, doi: 10.1179/026708309X12512744154360.
- [62] T. Haze, S. Aihara, and H. Mabuchi, “Characteristics of high-strength steel plates for low-temperature service with high weldability and HAZ toughness imparted by controlled rolling and accelerated cooling,” *Proc. Metall. Soc. Can. Inst. Min. Metall.*, vol. 3, pp. 235–247, 1988, doi: 10.1016/b978-0-08-035770-6.50021-0.
- [63] H. K. D. H. Bhadeshia and R. W. K. Honeycombe, *Steels: microstructure and properties*. Butterworth-Heinemann, 2017.
- [64] C. Hofer *et al.*, “High-resolution characterization of the martensite-austenite constituent in a carbide-free bainitic steel,” *Mater. Charact.*, vol. 144, no. July, pp. 182–190, 2018, doi: 10.1016/j.matchar.2018.07.011.
- [65] J. C. F. Jorge *et al.*, “Microstructure characterization and its relationship with impact toughness of C-Mn and high strength low alloy steel weld metals - A review,” *J. Mater. Res. Technol.*, vol. 10, pp. 471–501, 2021, doi: 10.1016/j.jmrt.2020.12.006.

- [66] C. L. Davis and J. E. King, “Cleavage initiation in the intercritically reheated coarse-grained heat-affected zone: Part I. Fractographic evidence,” *Metall. Mater. Trans. A*, vol. 25, no. 3, pp. 563–573, 1994, doi: 10.1007/BF02651598.
- [67] K. Wu *et al.*, “Microstructure and charpy impact toughness of a 2.25Cr-1Mo-0.25V steelweld metal,” *Materials (Basel)*., vol. 13, no. 13, 2020, doi: 10.3390/ma13133013.
- [68] B. C. Kim, S. Lee, N. J. Kim, and D. Y. Lee, “Microstructure and local brittle zone phenomena in high-strength low-alloy steel welds,” *Metall. Trans. A*, vol. 22, no. 1, pp. 139–149, 1991, doi: 10.1007/BF03350956.
- [69] M. Militzer, R. Pandi, and E. B. Hawbolt, “Ferrite nucleation and growth during continuous cooling,” *Metall. Mater. Trans. A Phys. Metall. Mater. Sci.*, vol. 27, no. 6, pp. 1547–1556, 1996, doi: 10.1007/BF02649814.
- [70] M. Militzer, E. B. Hawbolt, and T. R. Meadowcroft, “Microstructural model for hot strip rolling of high-strength low-alloy steels,” *Metall. Mater. Trans. A Phys. Metall. Mater. Sci.*, vol. 31, no. 4, pp. 1247–1259, 2000, doi: 10.1007/s11661-000-0120-4.
- [71] S. Roy, “Austenite decomposition in the coarse grain heat affected zone of X80 line pipe steel,” M.A.Sc Thesis, The University of British Columbia, Vancouver, 2020.
- [72] T. T. Pham, “Mathematical modelling of the onset of transformation from austenite to pearlite under non-continuous cooling conditions,” M.A.Sc. Thesis, The University of British Columbia, Vancouver, 1993.
- [73] S. Gerami, “Characterization and microstructural evolution model of a Nb ferrite-bainite steel,” M.A.Sc Thesis, The University of British Columbia, Vancouver, 2010.
- [74] A. J. DeArdo, “High strength low alloy steels,” in *AIME Conference Proceedings*, 1984, p. 70.

- [75] G. Thewlis, “Transformation kinetics of ferrous weld metals,” *Mater. Sci. Technol. (United Kingdom)*, vol. 10, no. 2, pp. 110–125, 1994, doi: 10.1179/mst.1994.10.2.110.
- [76] R. A. Farrar and Z. Zhang, “Experimental verification of the continuous-cooling transformation diagram produced by the dilatometry-metallography method,” *J. Mater. Sci. Lett.*, vol. 12, no. 20, pp. 1606–1611, 1993, doi: 10.1007/BF00627027.
- [77] A. K. Lis and J. Lis, “Effect of hot deformation and cooling rate on phase transformations in low carbon HN5MVNb bainitic steel,” *Mater. Sci. Forum*, vol. 539–543, pp. 4620–4625, 2007, doi: 10.4028/www.scientific.net/msf.539-543.4620.
- [78] F. B. Amin, R. K. & Pickering, “Austenite grain coarsening and the effect of thermomechanical processing on austenite recrystallization in thermomechanical processing of microalloyed austenite,” in *Austenite Grain Coarsening and the Effect of Thermomechanical Processing on Austenite Recrystallization in Thermomechanical Processing of Microalloyed Austenite*, 1982.
- [79] M. Umemoto, H. Ohtsuka, and I. Tamura, “Transformation to pearlite from work-hardened austenite,” *Trans. Iron Steel Inst. Japan*, vol. 23, no. 9, pp. 775–784, 1983, doi: 10.2355/isijinternational1966.23.775.
- [80] G. R. Speich, L. J. Cuddy, C. R. Gordon, and A. J. DeArdo, “Formation of ferrite from control-rolled austenite,” in *Phase transformations in ferrous alloys*, 1981, pp. 341–389.
- [81] C. Ouchi, T. Sampei, and I. Kozasu, “The effect of hot rolling condition and chemical composition on the onset temperature of $\gamma \rightarrow \alpha$ transformation after hot rolling,” *Trans. Iron Steel Inst. Japan*, vol. 22, no. 3, pp. 214–222, 1982, doi: 10.2355/isijinternational1966.22.214.
- [82] D. N. Hanlon, J. Sietsma, and S. Van Der Zwaag, “The effect of plastic deformation of

austenite on the kinetics of subsequent ferrite formation," *ISIJ Int.*, vol. 41, no. 9, pp. 1028–1036, 2001, doi: 10.2355/isijinternational.41.1028.

- [83] Y. Van Leeuwen and J. Sietsma, "The effect of plastic deformation on the formation of different morphologies of ferrite upon cooling," *Mater. Sci. Forum*, vol. 539–543, pp. 4572–4577, 2007, doi: 10.4028/www.scientific.net/msf.539-543.4572.
- [84] M. Suehiro, K. Sato, Y. Tsukano, Y. Takehide, and M. Yoshikazu, "Computer modeling of microstructural change and strength of low carbon steel in hotsStrip rolling," *ISIJ Int.*, no. 439, pp. 261–287, 1987.
- [85] F. Fazeli and M. Militzer, "Effect of Nb on austenite formation and decomposition in an X80 linepipe steel," *J. Iron Steel Res. Int.*, vol. 18, no. 1–2, pp. 658–663, 2011.
- [86] M. Militzer, F. Fazeli, and H. Azizi-Alizamini, "Modelling of microstructure evolution in advanced high strength steels," *La Metall. Ital.*, vol. 4, pp. 35–41, 2011.
- [87] R. G. Kamat, E. B. Hawbolt, L. C. Brown, and J. K. Brimacombe, "Principle of additivity and the proeutectoid ferrite transformation," *Metall. Trans. A, Phys. Metall. Mater. Sci.*, vol. 23, no. 9, pp. 2469–2480, 1992.
- [88] R. A. Vandermeer, "Modeling diffusional growth during austenite decomposition to ferrite in polycrystalline FeC alloys," *Acta Metall. Mater.*, vol. 38, no. 12, pp. 2461–2470, 1990, doi: 10.1016/0956-7151(90)90257-H.
- [89] T. A. Kop, Y. Van Leeuwen, J. Sietsma, and S. Van Der Zwaag, "Modelling the austenite to ferrite phase transformation in low carbon steels in terms of the interface mobility," *ISIJ Int.*, vol. 40, no. 7, pp. 713–718, 2000, doi: 10.2355/isijinternational.40.713.
- [90] G. P. Krielaart, J. Sietsma, and S. van der Zwaag, "Ferrite formation in Fe-C alloys during austenite decomposition under non-equilibrium interface conditions," *Mater. Sci. Eng.*,

vol. 237, no. 2, pp. 216–223, 1997.

- [91] H. Chen *et al.*, “Austenite/ferrite interface migration and alloying elements partitioning: an overview,” *Jinshu Xuebao/Acta Metall. Sin.*, vol. 54, no. 2, pp. 217–227, 2018, doi: 10.11900/0412.1961.2017.00465.
- [92] J. W. Christian, “The thermodynamics of irreversible processes,” *Theory Transform. Met. Alloy.*, pp. 95–105, 2002, doi: 10.1016/b978-008044019-4/50008-8.
- [93] K. Barmak, “A commentary on: ‘Reaction kinetics in processes of nucleation and growth,’” *Metall. Mater. Trans. A Vol.*, vol. 41, pp. 2711–2775, 2010.
- [94] Y. Cho, Y.-R. Im, J. K. Lee, D. Suh, S.-J. Kim, and H. N. Han, “A finite element modeling for dilatometric nonisotropy in steel,” *Metall. Mater. Trans. A*, vol. 42, no. 7, pp. 2094–2106, 2011.
- [95] B. Zhu and M. Militzer, “3D phase field modelling of recrystallization in a low-carbon steel,” *Model. Simul. Mater. Sci. Eng.*, vol. 20, no. 8, p. 085011, 2012.
- [96] H. Luo, J. Sietsma, and S. Van Der Zwaag, “Effect of inhomogeneous deformation on the recrystallization kinetics of deformed metals,” *ISIJ Int.*, vol. 44, no. 11, pp. 1931–1936, 2004.
- [97] S. H. Mohamadi Azghandi *et al.*, “Investigation on decomposition behavior of austenite under continuous cooling in vanadium microalloyed steel (30MSV6),” *Mater. Des.*, vol. 88, pp. 751–758, 2015, doi: 10.1016/j.matdes.2015.09.046.
- [98] D. Liu, F. Fazeli, M. Militzer, and W. J. Poole, “A microstructure evolution model for hot rolling of a Mo-TRIP steel,” *Metall. Mater. Trans. A Phys. Metall. Mater. Sci.*, vol. 38, no. 4, pp. 894–909, 2007, doi: 10.1007/s11661-007-9116-7.
- [99] T. Garcin, M. Militzer, W. Poole, and L. Collins, “Microstructure model for the heat-

affected zone of X80 linepipe steel,” *Mater. Sci. Technol.*, vol. 32, no. 7, pp. 708–721, 2016.

- [100] S. Jones and H. Bhadeshia, “Competitive formation of inter-and intragranularly nucleated ferrite,” *Metall. Mater. Trans.*, vol. 28, no. 10, pp. 2005–2013, 1997.
- [101] M. Umemoto, N. Komatsubara, and I. Tamura, “Prediction of hardenability effects from isothermal transformation kinetics,” *J. Heat Treat.*, vol. 1, no. 3, pp. 57–64, 1980.
- [102] G. K. Manning and C. H. Lorig, “The relationship between transformation at constant temperature and transformation during cooling,” *Met. Technol.*, 1946.
- [103] S. Sarkar and M. Militzer, “Microstructure evolution model for hot strip rolling of Nb-Mo microalloyed complex phase steel,” *Mater. Sci. Technol.*, vol. 25, no. 9, pp. 1134–1146, 2009, doi: 10.1179/174328409X453271.
- [104] H. N. Han, J. K. Lee, H. J. Kim, and Y. S. Jin, “A model for deformation temperature and phase transformation behavior of steels on run-out table in hot strip mill,” *J. Mater. Process. Technol.*, vol. 128, no. 1–3, pp. 216–225, 2002, doi: 10.1016/S0924-0136(02)00454-5.
- [105] T. Zhang, “Intercritical austenite formation in the coarse grain heat affected zone in X80 line pipe steels,” M.A.Sc Thesis, The University of British Columbia, Vancouver, 2020.
- [106] A. Finel, Y. Le Bouar, B. Dabas, B. Appolaire, Y. Yamada, and T. Mohri, “Sharp phase field method,” *Phys. Rev. Lett.*, vol. 121, no. 2, p. 025501, 2018.
- [107] D. H. Yeon, P. R. Cha, and J. K. Yoon, “A phase field study for ferrite-austenite transitions under para-equilibrium,” *Scr. Mater.*, vol. 45, no. 6, pp. 661–668, 2001, doi: 10.1016/S1359-6462(01)01077-6.
- [108] G. Pariser, P. Schaffnit, I. Steinbach, and W. Bleck, “Simulation of the γ - α -transformation

using the phase-field method," *Steel Res.*, vol. 72, no. 9, pp. 354–360, 2001, doi: 10.1002/srin.200100130.

- [109] Y. Takahama and J. Sietsma, "Mobility analysis of the austenite to ferrite transformation in Nb microalloyed steel by phase field modelling," *ISIJ Int.*, vol. 48, no. 4, pp. 512–517, 2008, doi: 10.2355/isijinternational.48.512.
- [110] M. Dubois, M. Militzer, A. Moreau, and J. F. Bussière, "New technique for the quantitative real-time monitoring of austenite grain growth in steel," *Scr. Mater.*, vol. 42, no. 9, pp. 867–874, Apr. 2000, doi: 10.1016/S1359-6462(00)00305-5.
- [111] M. Militzer, M. Maalekian, and A. Moreau, "Laser-ultrasonic austenite grain size measurements in low-carbon steels," in *Materials Science Forum*, 2012, vol. 715–716, pp. 407–414, doi: 10.4028/www.scientific.net/MSF.715-716.407.
- [112] M. Maalekian, R. Radis, M. Militzer, A. Moreau, and W. J. Poole, "In situ measurement and modelling of austenite grain growth in a Ti/Nb microalloyed steel," *Acta Mater.*, vol. 60, no. 3, pp. 1015–1026, 2012, doi: 10.1016/j.actamat.2011.11.016.
- [113] M. Maalekian, R. Radis, M. Militzer, A. Moreau, and W. J. Poole, "In situ measurement and modelling of austenite grain growth in a Ti/Nb microalloyed steel," *Acta Mater.*, vol. 60, no. 3, pp. 1015–1026, 2012, doi: 10.1016/j.actamat.2011.11.016.
- [114] S. Sarkar, "Microstructural evolution model for hot strip rolling of a Nb-Mo complex-phase steel," PhD Thesis, The University of British Columbia, Vancouver, 2008.
- [115] L. Zhao *et al.*, "Quantitative dilatometric analysis of intercritical annealing in a low-silicon TRIP steel," *J. Mater. Sci.*, vol. 37, no. 8, pp. 1585–1591, 2002, doi: 10.1023/A:1014941424093.
- [116] T. Nyssönen, N. Nyssönen, P. Peura, and V.-T. Kuokkala, "Crystallography,

morphology, and martensite transformation of prior austenite in intercritically annealed high-aluminum steel,” *Metall. Mater. Trans. A*, vol. 49, doi: 10.1007/s11661-018-4904-9.

- [117] N. Nakata and M. Militzer, “Modelling of microstructure evolution during hot rolling of a 780 MPa high strength steel,” *ISIJ Int.*, vol. 45, no. 1, pp. 82–90, 2005, doi: 10.2355/isijinternational.45.82.
- [118] R. L. Bodnar and S. S. Hansen, “Effects of austenite grain size and cooling rate on Widmanstätten ferrite formation in low-alloy steels,” *Metall. Mater. Trans. A*, vol. 25, no. 4, pp. 665–675, 1994, doi: 10.1007/BF02665443.
- [119] R. A. Farrar, Z. Zhang, S. R. Bannister, and G. S. Barritte, “The effect of prior austenite grain size on the transformation behaviour of C-Mn-Ni weld metal,” *J. Mater. Sci.*, vol. 28, no. 5, pp. 1385–1390, 1993, doi: 10.1007/BF01191982.
- [120] K. K. Lottey, “Austenite decomposition of a HSLA-Nb/Ti steel and an Al-Trip steel during continuous cooling,” M.A. Sc Thesis, The University of British Columbia, Vancouver, 2004.
- [121] M. Militzer, “Austenite decomposition: overall kinetics during isothermal, and continuous cooling transformation,” *Encycl. Mater. Sci. Technol.*, pp. 1–5, 2001.